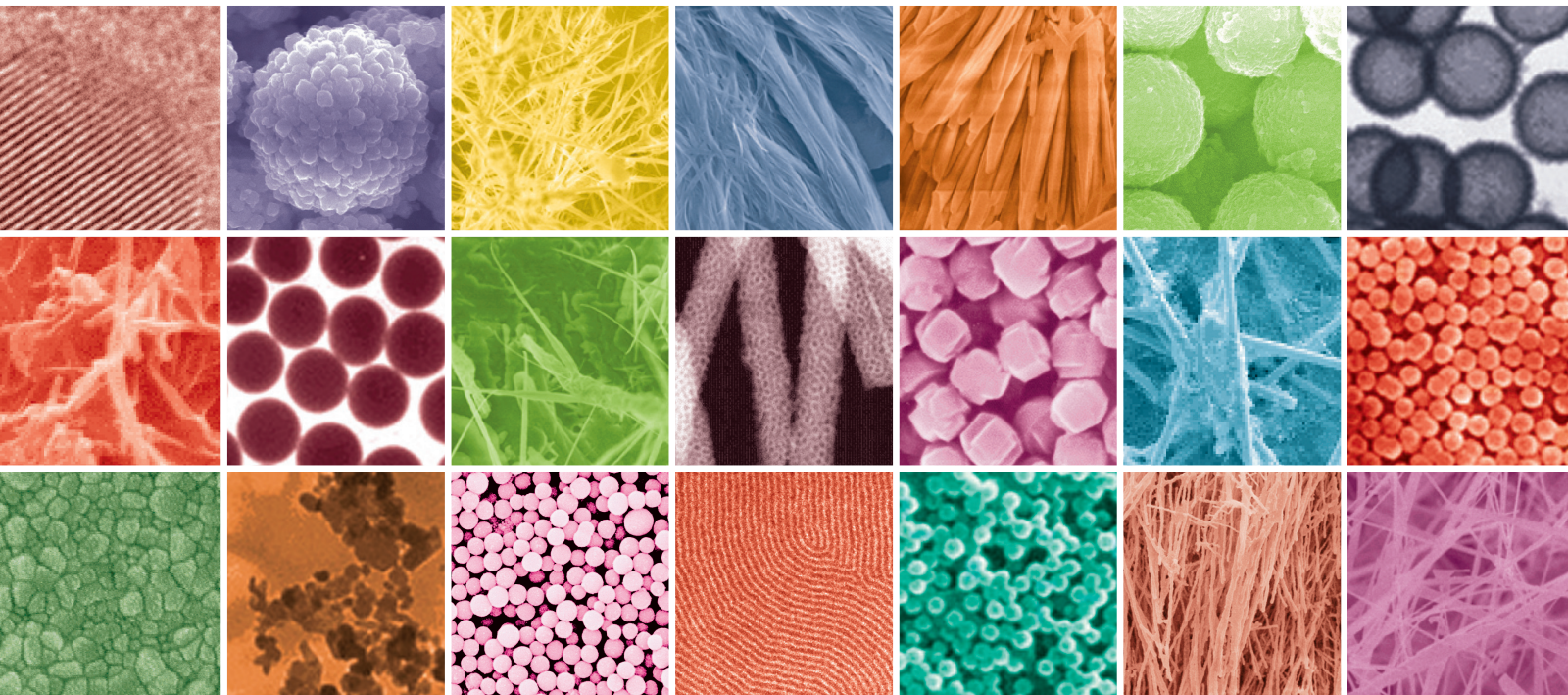


# Nanomaterials for Nanooptoelectronics Device Applications

Guest Editors: Chien-Jung Huang, Chi-Chih Liao, Mau-Phon Houng,  
Fu-Ken Liu, and Ying-Chung Chen





---

# **Nanomaterials for Nanooptoelectronics Device Applications**

# **Nanomaterials for Nanooptoelectronics Device Applications**

Guest Editors: Chien-Jung Huang, Chi-Chih Liao,  
Mau-Phon Houg, Fu-Ken Liu, and Ying-Chung Chen



---

Copyright © 2014 Hindawi Publishing Corporation. All rights reserved.

This is a special issue published in "Journal of Nanomaterials." All articles are open access articles distributed under the Creative Commons Attribution License, which permits unrestricted use, distribution, and reproduction in any medium, provided the original work is properly cited.

## Editorial Board

Domenico Acierno, Italy  
Katerina E. Aifantis, USA  
Sheikh Akbar, USA  
Nageh K. Allam, USA  
Margarida Amaral, Portugal  
Jordi Arbiol, Spain  
Raul Arenal, Spain  
Ilaria Armentano, Italy  
Xuedong Bai, China  
Lavinia Balan, France  
Thierry Baron, France  
Andrew R. Barron, USA  
Hongbin Bei, USA  
Stefano Bellucci, Italy  
Enrico Bergamaschi, Italy  
D. Bhattacharyya, New Zealand  
Giovanni Bongiovanni, Italy  
T. Borca-Tasciuc, USA  
M. Bououdina, Bahrain  
C. Jeffrey Brinker, USA  
Christian Brosseau, France  
Yibing Cai, China  
Chuanbao Cao, China  
Xuebo Cao, China  
Victor M. Castaño, Mexico  
Albano Cavaleiro, Portugal  
Bhanu P. S. Chauhan, USA  
Wei Chen, China  
Yuan Chen, Singapore  
Tupei Chen, Singapore  
Shafiul Chowdhury, USA  
Kwang-Leong Choy, UK  
Jin-Ho Choy, Korea  
Yu-Lun Chueh, Taiwan  
Elisabetta Comini, Italy  
Giuseppe Compagnini, Italy  
M. A. Correa-Duarte, Spain  
P. Davide Cozzoli, Italy  
Majid Darroudi, Iran  
Shadi A. Dayeh, USA  
Yong Ding, USA  
Bin Dong, China  
Zehra Durmus, Turkey  
Joydeep Dutta, Oman  
Ali Eftekhari, USA  
Samy El-Shall, USA  
Farid El-Tantawy, Egypt  
Ovidiu Ersen, France  
Claude Estournès, France  
Andrea Falqui, Saudi Arabia  
Xiaosheng Fang, China  
Bo Feng, China  
Matteo Ferroni, Italy  
W. Fritzsche, Germany  
Alan Fuchs, USA  
Lian Gao, China  
Peng Gao, China  
Miguel A. Garcia, Spain  
Siddhartha Ghosh, Singapore  
P. K. Giri, India  
Russell E. Gorga, USA  
Jihua Gou, USA  
Alexander Govorov, USA  
Jean M. Greneche, France  
Changzhi Gu, China  
Hongchen Chen Gu, China  
Mustafa O. Guler, Turkey  
John Z. Guo, USA  
Lin Guo, China  
Smrati Gupta, Germany  
K. Hamad-Schifferli, USA  
Michael Harris, USA  
Jr-Hau He, Taiwan  
Nguyen D. Hoa, Vietnam  
Zhongkui Hong, China  
Michael Z. Hu, USA  
Nay Ming Huang, Malaysia  
Qing Huang, China  
Shaoming Huang, China  
David Hui, USA  
Zafar Iqbal, USA  
B. Jeyadevan, Japan  
Sheng-Rui Jian, Taiwan  
Xin Jiang, Germany  
Wanqin Jin, China  
Rakesh K. Joshi, UK  
Myung-Hwa Jung, Korea  
Jeong-won Kang, Korea  
Zhenhui Kang, China  
Hassan Karimi-Maleh, Iran  
Fathallah Karimzadeh, Iran  
Antonios Kelarakis, UK  
Alireza Khataee, Iran  
Ali Khorsand Zak, Iran  
Wonbaek Kim, Korea  
Jang-Kyo Kim, Hong Kong  
Dojin Kim, Korea  
Philippe Knauth, France  
Christian Kübel, Germany  
Prashant Kumar, UK  
Sanjeev Kumar, India  
Sushil Kumar, India  
Subrata Kundu, India  
Alan K. T. Lau, Hong Kong  
Michele Laus, Italy  
Eric Le Bourhis, France  
Burtrand Lee, USA  
Jun Li, Singapore  
Benxia Li, China  
Xing-Jie Liang, China  
Meiyong Liao, Japan  
Shijun Liao, China  
Silvia Licoccia, Italy  
Wei Lin, USA  
Gong-Ru Lin, Taiwan  
Jun Liu, USA  
Tianxi Liu, China  
Zainovia Lockman, Malaysia  
Jue Lu, USA  
Songwei Lu, USA  
Ed Ma, USA  
Malik Maaza, South Africa  
Lutz Mädler, Germany  
Gaurav Mago, USA  
Morteza Mahmoudi, Iran  
Santanu K. Maiti, India  
Mohammad A. Malik, UK  
Devanesan Mangalaraj, India  
Sanjay R. Mathur, Germany  
V. Mittal, United Arab Emirates  
Paulo Cesar Morais, Brazil  
Mahendra A. More, India  
Paul Munroe, Australia  
Jae-Min Myoung, Korea  
Rajesh Naik, USA

Albert Nasibulin, Russia  
Toshiaki Natsuki, Japan  
Weihai Ni, China  
Koichi Niihara, Japan  
Sherine Obare, USA  
W.-C. Oh, Republic of Korea  
Atsuto Okamoto, Japan  
Abdelwahab Omri, Canada  
Ungyu Paik, Republic of Korea  
Edward A. Payzant, USA  
Ton Peijs, UK  
Kui-Qing Peng, China  
O. Perales-Perez, Puerto Rico  
A. Phuruangrat, Thailand  
Wenxiu Que, China  
S. Sinha Ray, South Africa  
Peter Reiss, France  
Orlando Rojas, USA  
Marco Rossi, Italy  
Cengiz S. Ozkan, USA  
Vladimir Šepelák, Germany  
Ugur Serincan, Turkey  
Huaiyu Shao, Japan  
Prashant K. Sharma, India  
Donglu Shi, USA

Bhanu P. Singh, India  
Surinder Singh, USA  
Vladimir Sivakov, Germany  
Yanlin Song, China  
Ashok Sood, USA  
Marinella Striccoli, Italy  
Bohua Sun, South Africa  
Jing Sun, China  
Xuping Sun, Saudi Arabia  
Ashok K. Sundramoorthy, USA  
Sabine Szunerits, France  
Nyan-Hwa Tai, Taiwan  
Bo Tan, Canada  
Somchai Thongtem, Thailand  
Ion Tiginyanu, Moldova  
Alexander Tolmachev, Ukraine  
Valeri P. Tolstoy, Russia  
Muhammet S. Toprak, Sweden  
Ramon Torrecillas, Spain  
Takuya Tsuzuki, Australia  
Tamer Uyar, Turkey  
Bala Vaidhyanathan, UK  
Luca Valentini, Italy  
Rajender S. Varma, USA  
Raquel Verdejo, Spain

Antonio Villaverde, Spain  
Ajayan Vinu, Australia  
Zhenbo Wang, China  
Shiren Wang, USA  
Yong Wang, USA  
Ruibing Wang, Macau  
Magnus Willander, Sweden  
Xingcai Wu, China  
Zhi Li Xiao, USA  
Ping Xiao, UK  
Shuangxi Xing, China  
Yangchuan Xing, USA  
Doron Yadlovker, Israel  
Yingkui Yang, China  
Piaoping Yang, China  
Yoke K. Yap, USA  
Ramin Yousefi, Iran  
William W. Yu, USA  
Kui Yu, Canada  
Haibo Zeng, China  
Bin Zhang, China  
Renyun Zhang, Sweden  
Yanbao Zhao, China  
L. Zheng, United Arab Emirates  
Chunyi Zhi, Hong Kong

**Nanomaterials for Nanooptoelectronics Device Applications**, Chien-Jung Huang, Chi-Chih Liao, Mau-Phon Houng, Fu-Ken Liu, and Ying-Chung Chen  
Volume 2014, Article ID 178686, 1 pages

**Analysis of the High Conversion Efficiencies  $\beta$ -FeSi<sub>2</sub> and BaSi<sub>2</sub> n-i-p Thin Film Solar Cells**, Jung-Sheng Huang, Kuan-Wei Lee, and Yu-Hsiang Tseng  
Volume 2014, Article ID 238291, 5 pages

**Improvement of Short-Circuit Current Density in p-Ni<sub>1-x</sub>O:Li/n-Si Heterojunction Solar Cells by Wet Chemical Etching**, Feng-Hao Hsu, Na-Fu Wang, Yu-Zen Tsai, Ming-Hao Chien, and Mau-Phon Houng  
Volume 2014, Article ID 104136, 7 pages

**Effect of Chromium Interlayer Thickness on Optical Properties of Au-Ag Nanoparticle Array**, Jing Liu, Haoyuan Cai, Lingqi Kong, and Xianfang Zhu  
Volume 2014, Article ID 650359, 9 pages

**Development of Tandem Amorphous/Microcrystalline Silicon Thin-Film Large-Area See-Through Color Solar Panels with Reflective Layer and 4-Step Laser Scribing for Building-Integrated Photovoltaic Applications**, Chin-Yi Tsai and Chin-Yao Tsai  
Volume 2014, Article ID 809261, 9 pages

**Characterization of the Nanoporous Template Using Anodic Alumina Method**, Mau-Phon Houng, Wei-Lun Lu, Tsung-Hsin Yang, and Kuan-Wei Lee  
Volume 2014, Article ID 130716, 7 pages

**Nanographene-Based Saturable Absorbers for Ultrafast Fiber Lasers**, Hsin-Hui Kuo and Shuo-Fu Hong  
Volume 2014, Article ID 631928, 6 pages

**Development of Amorphous/Microcrystalline Silicon Tandem Thin-Film Solar Modules with Low Output Voltage, High Energy Yield, Low Light-Induced Degradation, and High Damp-Heat Reliability**, Chin-Yi Tsai and Chin-Yao Tsai  
Volume 2014, Article ID 861741, 10 pages

**High Stability White Organic Light-Emitting Diode (WOLED) Using Nano-Double-Ultra Thin Carrier Trapping Materials**, Kan-Lin Chen  
Volume 2014, Article ID 173276, 7 pages

**Theoretical Study of the Effects of Carrier Transport, Capture, and Escape Processes on Solar Cells with Embedded Nanostructures**, Chin-Yi Tsai  
Volume 2014, Article ID 972597, 8 pages

## Editorial

# Nanomaterials for Nanooptoelectronics Device Applications

**Chien-Jung Huang,<sup>1</sup> Chi-Chih Liao,<sup>2</sup> Mau-Phon Houng,<sup>3</sup>  
Fu-Ken Liu,<sup>4</sup> and Ying-Chung Chen<sup>5</sup>**

<sup>1</sup> Department of Applied Physics, National University of Kaohsiung, Kaohsiung 81148, Taiwan

<sup>2</sup> Applied Optoelectronics, Inc., Sugar Land, TX 77478, USA

<sup>3</sup> Institute of Microelectronics and Department of Electrical Engineering, National Cheng Kung University, Tainan 70101, Taiwan

<sup>4</sup> Department of Applied Chemistry, National University of Kaohsiung, Kaohsiung 81148, Taiwan

<sup>5</sup> Department of Electrical Engineering, National Sun Yat-Sen University, Kaohsiung 80424, Taiwan

Correspondence should be addressed to Chien-Jung Huang; [chien@nuk.edu.tw](mailto:chien@nuk.edu.tw)

Received 6 November 2014; Accepted 6 November 2014; Published 30 December 2014

Copyright © 2014 Chien-Jung Huang et al. This is an open access article distributed under the Creative Commons Attribution License, which permits unrestricted use, distribution, and reproduction in any medium, provided the original work is properly cited.

Nanomaterials are a new class of materials, with dimensions in the  $0.1\ \mu\text{m}\sim 0.1\ \text{nm}$  range, that provide great potentials of improving and enhancing the performance and functionality of many industrial products. Nanostructures, based on their shapes, can be categorized into uniform zero-dimensional (0D), elongated one-dimensional (1D), and planar two-dimensional (2D) structures. The recent emphasis on the nanomaterial research is put on 1D nanostructures at the expense of 0D and 2D ones, perhaps due to the intriguing possibility of using them in a majority of short-term future applications. The most successful examples are seen in the microelectronic, green energy or display where these have always meant a greater performance ever since the invention of transistors, invertors, and lightings, for example, higher density of integration, faster response, lower cost, and less power consumption.

In recent years, the nanomaterials for nanooptoelectronics device applications have been highly developed in various fields, due to their flexibility and light weight for daily use. As a result, the field of nanooptoelectronics device has been the subject of intensive researches and investigations. In addition, nanooptoelectronics devices are environmentally sustainable due to the abundant availability of the nanostructured raw materials. The chance to share and discuss these crucial nanooptoelectronics developments in a timely and influential forum is important. This special issue selects 20 papers about display, solar cell materials, devices,

and processing, nanoscale luminescent materials, and other related fields. This special issue enables interdisciplinary collaboration between engineering technologists and science in the industrials and academic field.

*Chien-Jung Huang  
Chi-Chih Liao  
Mau-Phon Houng  
Fu-Ken Liu  
Ying-Chung Chen*

## Research Article

# Analysis of the High Conversion Efficiencies $\beta$ -FeSi<sub>2</sub> and BaSi<sub>2</sub> n-i-p Thin Film Solar Cells

Jung-Sheng Huang, Kuan-Wei Lee, and Yu-Hsiang Tseng

Department of Electronic Engineering, I-Shou University, Kaohsiung 840, Taiwan

Correspondence should be addressed to Jung-Sheng Huang; [jshuang@isu.edu.tw](mailto:jshuang@isu.edu.tw)

Received 20 June 2014; Revised 20 September 2014; Accepted 22 September 2014; Published 29 December 2014

Academic Editor: Chien-Jung Huang

Copyright © 2014 Jung-Sheng Huang et al. This is an open access article distributed under the Creative Commons Attribution License, which permits unrestricted use, distribution, and reproduction in any medium, provided the original work is properly cited.

Both  $\beta$ -FeSi<sub>2</sub> and BaSi<sub>2</sub> are silicides and have large absorption coefficients; thus they are very promising Si-based new materials for solar cell applications. In this paper, the dc  $I$ - $V$  characteristics of n-Si/i- $\beta$ FeSi<sub>2</sub>/p-Si and n-Si/i-BaSi<sub>2</sub>/p-Si thin film solar cells are investigated by solving the charge transport equations with optical generations. The diffusion current densities of free electron and hole are calculated first. Then the drift current density in the depletion regions is obtained. The total current density is the sum of diffusion and drift current densities. The conversion efficiencies are obtained from the calculated  $I$ - $V$  curves. The optimum conversion efficiency of n-Si/i- $\beta$ FeSi<sub>2</sub>/p-Si thin film solar cell is 27.8% and that of n-Si/i-BaSi<sub>2</sub>/p-Si thin film solar cell is 30.4%, both are larger than that of Si n-i-p solar cell ( $\eta$  is 20.6%). These results are consistent with their absorption spectrum. The calculated conversion efficiency of Si n-i-p solar cell is consistent with the reported researches. Therefore, these calculation results are valid in this work.

## 1. Introduction

A silicide is a compound that has silicon with more electropositive elements. The metal silicides have been widely investigated for several years because of their potential applications in electronics [1]. Semiconducting beta-phase iron disilicide ( $\beta$ -FeSi<sub>2</sub>) and orthorhombic barium silicide (BaSi<sub>2</sub>) are two transition metal silicides and they are very promising Si-based new materials for solar cell applications. It is desirable for solar cell materials to have a large absorption coefficient to yield high conversion efficiencies.  $\beta$ -FeSi<sub>2</sub> has a large optical absorption coefficient ( $>10^5$  cm<sup>-1</sup> at 1.5 eV) and a direct band gap of  $\sim 0.87$  eV [2–4]. Lin et al. [5] reported a conversion efficiency of 3.7% for p- (or n-) type  $\beta$ -FeSi<sub>2</sub>/n- (or p-) type Si solar cell. Gao et al. [6] simulated a p-Si/i- $\beta$ FeSi<sub>2</sub>/n-Si solar cell structure by using the AMPS-1D software. The conversion efficiency is 24.7%. The orthorhombic barium silicide (BaSi<sub>2</sub>) also has a large absorption coefficient of over  $10^5$  cm<sup>-1</sup> at 1.5 eV [7]. Recent reports on the photoresponse properties of BaSi<sub>2</sub> have shown that BaSi<sub>2</sub> is a new silicide material suitable for solar cell applications [8, 9].

Therefore, in this paper the conversion efficiencies of n-Si/i- $\beta$ FeSi<sub>2</sub>/p-Si and n-Si/i-BaSi<sub>2</sub>/p-Si thin film solar cells are investigated by using self-developed analytical methods. For semiconductor solar cells, the n-i-p structure usually has superior  $I$ - $V$  characteristics than the n-p structure. Since the built-in electric field exists in the intrinsic layer, the generated electron-hole pairs in the intrinsic layer are drifted by the electric field and produce larger short-circuit current and open-circuit voltage. In addition, the intrinsic silicide layer does not need doping and its manufacturing is compatible with the well-established Si solar cells. The distributions of minority carrier concentrations in the neutral n-Si and p-Si regions are calculated first. Then the total current density is the sum of diffusion current densities of free electron and hole and the drift current density in the depletion regions. The conversion efficiencies are calculated from the  $I$ - $V$  curves of the solar cells with illumination of light. The calculated optimum conversion efficiency of  $\beta$ -FeSi<sub>2</sub> n-i-p solar cell is 27.8% and that of BaSi<sub>2</sub> p-i-n solar cell is 30.4% and that of Si n-i-p solar cell is 20.6%. Therefore, the conversion efficiencies of  $\beta$ -FeSi<sub>2</sub> and BaSi<sub>2</sub> n-i-p solar cells are significantly larger than that of the conventional Si n-i-p solar cells. The reported

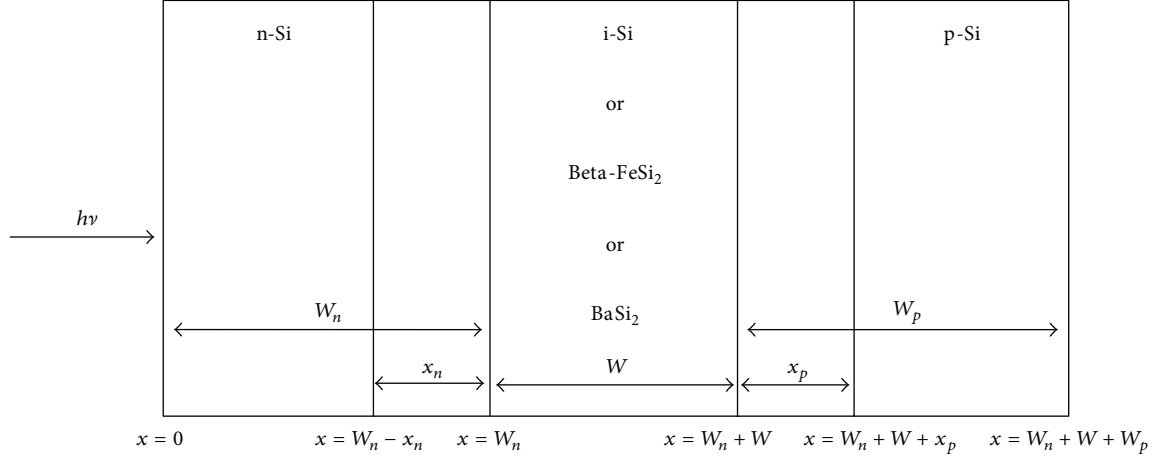


FIGURE 1: A one-dimensional analysis model of n-i-p thin film solar cells.

conversion efficiency of Si n-i-p solar cell is consistent with this calculation work [10]. Therefore, the calculation results are valid in this work.

## 2. Analysis Methods

The n-i-p structure of solar cells under investigation is shown in Figure 1. The calculations are under global AM1.5 solar spectrum ( $\text{Wm}^{-2}$ ) at  $25^\circ\text{C}$ . At the surface of the solar cell (i.e., at  $x = 0$ ), the generation rate of electron-hole pairs,  $G_0(\lambda)$  ( $\text{s}^{-1}\text{m}^{-3}$ ), is [11]

$$G_0(\lambda) = \eta_i [1 - R(\lambda)] \frac{I_{\text{opt}}}{\hbar\omega} \alpha(\lambda), \quad (1)$$

where  $\lambda$  = the wavelength of the incident light (m),  $\eta_i$  = the intrinsic quantum efficiency to account for the average number (100% maximum) of electron-hole pairs generated per incident photon,  $R(\lambda)$  = the optical reflectivity between the air and the semiconductor,  $I_{\text{opt}}$  = the incident optical power intensity ( $\text{Wm}^{-2}$ ),  $\hbar\omega$  = the energy of the incident photon (Joul), and  $\alpha(\lambda)$  = the absorption spectrum ( $\text{m}^{-1}$ ).

The generation rate of electron-hole pairs in the solar cell device ( $x > 0$ ) is

$$G(x, \lambda) = G_0(\lambda) e^{-\alpha(\lambda)x}. \quad (2)$$

In the neutral n-Si region, the charge transport equation for the excess hole concentration,  $\delta P_n$ , is

$$\frac{d^2}{dx^2} \delta P_n(x, \lambda) - \frac{1}{L_p^2} \delta P_n(x, \lambda) = -\frac{1}{D_p} G(x, \lambda), \quad (3)$$

where  $L_p$  = the average diffusion length of holes in n-type region (m) and  $D_p$  = the diffusion coefficient of minority holes ( $\text{m}^2\text{s}^{-1}$ ).

The two boundary conditions to solve (3) are as follows.

(a) At the edge of n-Si depletion region ( $x = W_n - X_n$ ):

$$\delta P_n = P_{no} \left[ e^{qv/kt} - 1 \right]. \quad (4)$$

(b) At the surface of n-Si ( $x = 0$ ):

$$D_p \frac{d}{dx} \delta P_n = S_p \delta P_n, \quad (5)$$

where  $S_p$  is the surface recombination velocity of holes ( $\text{ms}^{-1}$ ).

Then the hole diffusion current density is calculated at the edge of the n-Si depletion region as

$$J_{p,\text{diff}} = -qD_p \frac{d}{dx} \delta P_n \Big|_{x=W_n-x_n}. \quad (6)$$

Similarly, the distribution of free electron density,  $\delta n_p(x, \lambda)$ , in the neutral region of the p-Si can be obtained by solving the charge transport equation for  $\delta n_p$ . And the electron diffusion current density is calculated at the edge of the p-Si depletion region as

$$J_{n,\text{diff}} = qD_n \frac{d}{dx} \delta n_p \Big|_{x=W_n+W+x_p}. \quad (7)$$

The drift current density due to optical generation in the depletion regions is calculated as

$$\begin{aligned} J_{\text{drift}} = & q \int_{\text{n-Si}} G_0(\text{Si}) e^{-\alpha(\text{Si})x} dx \\ & + q \int_{\text{i-region}} G_0(\beta - \text{FeSi}_2) e^{-\alpha(\beta - \text{FeSi}_2)x} dx \\ & + q \int_{\text{p-Si}} G_0(\text{Si}) e^{-\alpha(\text{Si})x} dx, \end{aligned} \quad (8)$$

where the first term accounts for the drift current density obtained from the depletion region in n-Si. The second term is the drift current density from the intrinsic layer and the third term is the drift current density from the depletion region in p-Si.

The total current density for an incident photon flux at a given wavelength is

$$J(\lambda) = J_{p,\text{diff}}(\lambda) + J_{n,\text{diff}}(\lambda) + J_{\text{drift}}(\lambda). \quad (9)$$

TABLE 1: The optimum parameters used in the calculations of n-i-p solar cells with different intrinsic layer materials.

Parameters	Si	$\beta$ -FeSi <sub>2</sub>	BaSi <sub>2</sub>
Energy gap (eV)	1.12	0.85	1.086
Relative permittivity	11.9	22.5	11.17
Diffusion coefficient (cm <sup>2</sup> /s), $D_n$	35		
Diffusion coefficient (cm <sup>2</sup> /s), $D_p$	12.4		
Diffusion length ( $\mu$ m), $L_n$	13.2		
Diffusion length ( $\mu$ m), $L_p$	4.9		
Surface recombination velocity (cm/s), $S_n$	10 <sup>4</sup>		
Surface recombination velocity (cm/s), $S_p$	10 <sup>4</sup>		
Intrinsic quantum efficiency, $\eta_i$	0.6		
Optical reflectivity, $R$	0.1		

Then the total photo current is obtained by integrating all wavelengths from 300 nm to  $(hc/E_g)$  ( $E_g$  = the energy gap of the semiconductor material). The fill-factor (FF) is defined as

$$FF = \frac{V_m I_m}{V_{oc} I_{sc}}, \quad (10)$$

where  $V_m I_m$  = the maximum power output which occurs at a point on the  $I$ - $V$  curve,  $V_{oc}$  = the open-circuit voltage which occurs at the point with  $I = 0$  on the  $I$ - $V$  curve, and  $I_{sc}$  = the short-circuit current which occurs at the point with  $V = 0$ .

Finally, the conversion efficiency,  $\eta$ , is obtained as

$$\eta = \frac{V_{oc} I_{sc}}{P_{opt}} FF, \quad (11)$$

where  $P_{opt}$  = the incident optical power on the solar cell surface (W).

The optimum parameters used in this calculation are given in Table 1. The absorption spectrums of  $\beta$ -FeSi<sub>2</sub> and BaSi<sub>2</sub> are obtained by using the experiment results reported in [2], and the absorption spectrum of Si is obtained from [12].

### 3. Results and Discussion

The calculated p-Si/i- $\beta$ FeSi<sub>2</sub>/n-Si double heterojunction energy band diagram in thermal equilibrium is shown in Figure 2. The doping concentrations for both p-Si and n-Si layers are 10<sup>18</sup> cm<sup>-3</sup>. The thicknesses for both p-Si and n-Si layers are 1  $\mu$ m and for intrinsic  $\beta$ -FeSi<sub>2</sub> (or BaSi<sub>2</sub>) layer is 0.3  $\mu$ m. The p-Si and n-Si layers have larger bandgap energy than  $\beta$ -FeSi<sub>2</sub> and BaSi<sub>2</sub>. The wavelengths of solar radiation absorbed by the semiconductor materials are from 300 nm to  $(hc/E_g)$ . Therefore, the  $\beta$ -FeSi<sub>2</sub> and BaSi<sub>2</sub> have wider wavelength absorption ranges than Si. The generation rate of electron-hole pairs in  $\beta$ -FeSi<sub>2</sub> n-i-p solar cell is shown in Figure 3 by calculating (1) and (2). At the surface of the solar cell (i.e., at  $x = 0$ ), the generation rate of electron-hole pairs,  $G_0(\lambda)$  (s<sup>-1</sup>m<sup>-3</sup>), is proportional to the absorption spectrum,  $\alpha(\lambda)$  (m<sup>-1</sup>). The thickness of intrinsic layer is 0.3  $\mu$ m. The generation rate of electron-hole pairs,  $G(x, \lambda)$ , is a function of position,  $x$ , and the incident wavelength,  $\lambda$ . The

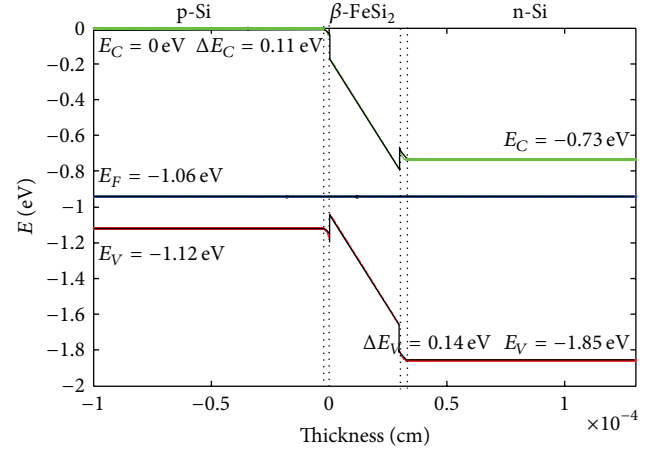


FIGURE 2: The equilibrium energy band diagram for p-Si/i- $\beta$ FeSi<sub>2</sub>/n-Si solar cell.

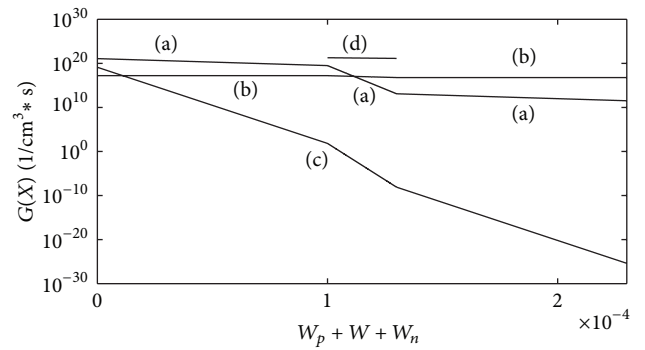


FIGURE 3: The generation rate as a function of position  $x$  with different wavelengths,  $\lambda$ , for  $\beta$ -FeSi<sub>2</sub> n-i-p solar cell. (a)  $\lambda = 0.405 \mu$ m, (b)  $\lambda = 1.101 \mu$ m, (c)  $\lambda = 0.305 \mu$ m, and (d)  $\lambda = 1.193 \mu$ m.

generation rate is exponentially decreased with the position  $x$  increased. There are four curves in Figure 3 corresponding to four different incident wavelengths. Note that, at incident optical wavelength  $\lambda = 1.193 \mu$ m (curve (d)), the generation rate is zero in Si regions, but in  $\beta$ -FeSi<sub>2</sub> region, the generation rate reaches maximum. Figure 4 shows the generation rate of electron-hole pairs in BaSi<sub>2</sub> n-i-p solar cell. Similarly, at incident optical wavelength  $\lambda = 1.086 \mu$ m (curve (d)), the generation rate is zero in Si regions, but in BaSi<sub>2</sub> region, the generation rate is maximum.

The minority carrier density distributions of  $\beta$ -FeSi<sub>2</sub> n-i-p solar cell with applied voltage  $V_a = 0$  are shown in Figure 5 by solving (3) to (5). The doping concentrations in n-Si and p-Si regions are both equal to 10<sup>18</sup> cm<sup>-3</sup>. The intrinsic layer thickness is 0.4  $\mu$ m. The slopes of these minority carrier density distributions at the depletion region edges determine the magnitudes of the diffusion currents (as shown in (6) and (7)). As shown in Figure 5, the maximum reverse hole diffusion current density is at wavelength  $\lambda = 0.55 \mu$ m (because the slope is maximum at this wavelength). The solar radiation is incident from n-Si to p-Si. Thus, the generation rates of electron-hole pairs in n-Si region are

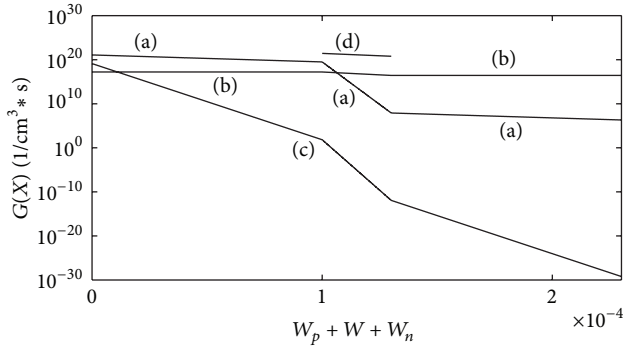


FIGURE 4: The generation rate as a function of position  $x$  with different wavelengths for BaSi<sub>2</sub> n-i-p solar cell. (a)  $\lambda = 0.405 \mu\text{m}$ , (b)  $\lambda = 1.101 \mu\text{m}$ , (c)  $\lambda = 0.305 \mu\text{m}$ , and (d)  $\lambda = 1.086 \mu\text{m}$ .

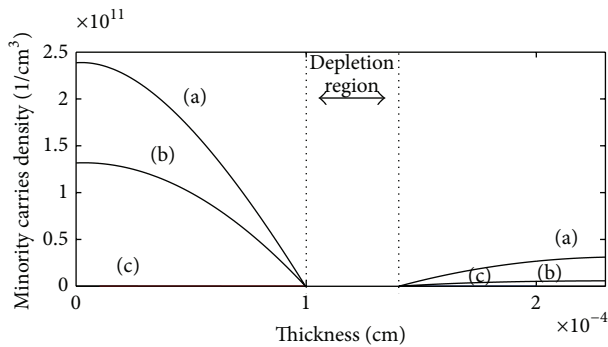


FIGURE 5: The minority carrier density distributions at  $V_a = 0 \text{ V}$  for  $\beta\text{-FeSi}_2$  solar cell with different wavelengths. (a)  $\lambda = 0.455 \mu\text{m}$ , (b)  $\lambda = 0.665 \mu\text{m}$ , and (c)  $\lambda = 1.101 \mu\text{m}$ .

larger than that in p-Si region. Therefore, the minority carrier density in n-Si region is larger than that in p-Si region at all wavelengths (as shown in Figure 5). And the diffusion current density is mainly determined by the hole diffusion current density. When the applied voltage reaches the open-circuit voltage ( $V_{oc} = 0.591 \text{ V}$ , now the total current is zero), the minority carrier density distributions of  $\beta\text{-FeSi}_2$  solar cell are shown in Figure 6. Compared with Figure 5, the minority carrier densities are increased exponentially with applied forward-biased voltage at the edges of depletion region. And the hole diffusion current density is negative at  $\lambda = 0.455 \mu\text{m}$  but is positive at  $\lambda = 1.101 \mu\text{m}$ . The calculated minority carrier diffusion current densities as a function of wavelengths for  $\beta\text{-FeSi}_2$  solar cell are shown in Figure 7 by calculating (6) and (7). When the applied voltage is zero (curve (a)), all of the minority carrier diffusion current densities are negative, and the maximum negative diffusion current density is at wavelength  $\lambda = 0.55 \mu\text{m}$ . When the applied voltage reaches the open-circuit voltage,  $V_{oc} = 0.591 \text{ V}$  (curve(b)), the minority carrier diffusion current densities are still negative at wavelengths  $0.5 \mu\text{m}$  to  $0.7 \mu\text{m}$ , but the magnitudes are decreased. However, at wavelengths between  $0.3 \mu\text{m}$  to  $0.5 \mu\text{m}$  and  $0.7 \mu\text{m}$  to  $1.1 \mu\text{m}$ , the minority carrier diffusion current densities become positive, and the maximum values are at  $0.3 \mu\text{m}$  and  $1.1 \mu\text{m}$ . The calculated

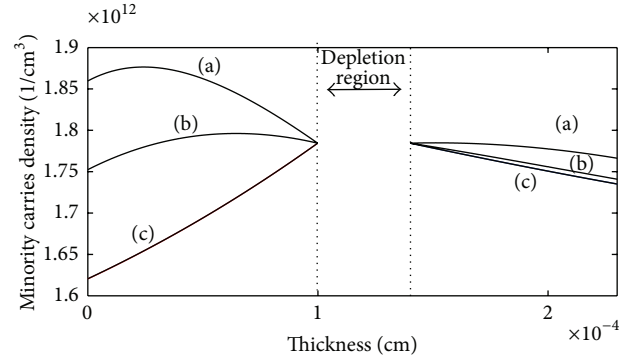


FIGURE 6: The minority carrier density distributions at  $V_a = V_{oc} = 0.591 \text{ V}$  for  $\beta\text{-FeSi}_2$  solar cell with different wavelengths. (a)  $\lambda = 0.455 \mu\text{m}$ , (b)  $\lambda = 0.665 \mu\text{m}$ , and (c)  $\lambda = 1.101 \mu\text{m}$ .

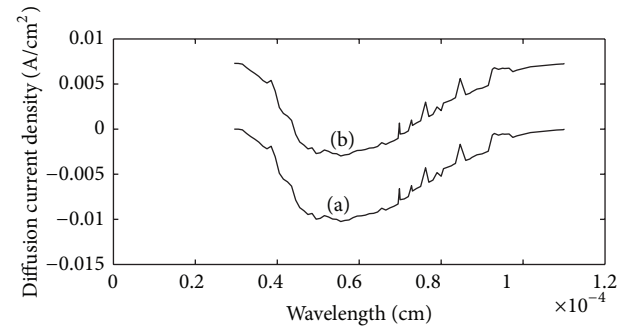


FIGURE 7: The calculated minority carrier diffusion current densities as a function of wavelengths for  $\beta\text{-FeSi}_2$  solar cell. (a)  $V_a = 0 \text{ V}$ , (b)  $V_a = V_{oc} = 0.591 \text{ V}$ .

drift current densities as a function of wavelengths for  $\beta\text{-FeSi}_2$  solar cell are shown in Figure 8 by calculating (8). The drift current densities are calculated in the depletion regions. They are almost the same between  $V_a = 0 \text{ V}$  (curve (a)) and  $V_a = V_{oc} = 0.591 \text{ V}$  (curve (b)). The drift current densities are always negative and are almost a constant for different wavelengths.

The calculated  $I$ - $V$  curves with different intrinsic layer materials (the intrinsic layer thickness is  $0.5 \mu\text{m}$  now) are shown in Figure 9. The reverse current density of BaSi<sub>2</sub> n-i-p solar cell is larger than that of  $\beta\text{-FeSi}_2$  and Si n-i-p solar cells. The calculated results of Figure 9 are listed in Table 2. Note that BaSi<sub>2</sub> has the maximum open-circuit current density ( $|J_{sc}| = 22.93 \text{ mA/cm}^2$ ), the maximum fill factor ( $\text{FF} = 82.63\%$ ), and the maximum conversion efficiency ( $\eta = 30.4\%$ ). The calculated optimum conversion efficiency of  $\beta\text{-FeSi}_2$  n-i-p solar cells is  $27.8\%$  and that of Si n-i-p solar cell is  $20.6\%$ . BaSi<sub>2</sub> has the maximum absorption spectrum and Si has the minimum absorption spectrum. Therefore, the calculation results of conversion efficiency for different materials are consistent with their absorption spectrum. The reported [10] efficiency of amorphous Si:H (pin) solar cell is  $10.1\%$ , and that of polycrystalline Si solar cell is  $20.4\%$  which is consistent with this calculation work. Thus, the calculation results are valid in this work.

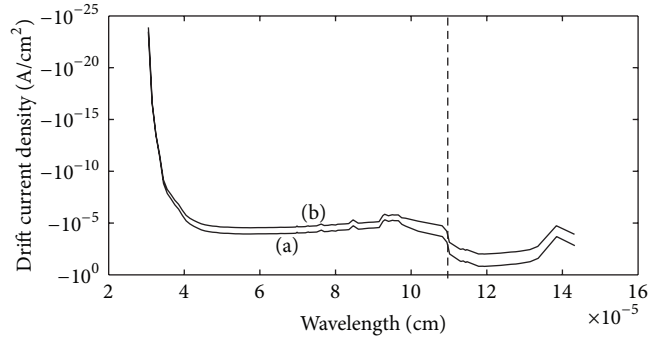


FIGURE 8: The calculated drift current densities as a function of wavelengths for  $\beta$ -FeSi<sub>2</sub> solar cell. (a)  $V_a = 0$  V, (b)  $V_a = V_{oc} = 0.591$  V.

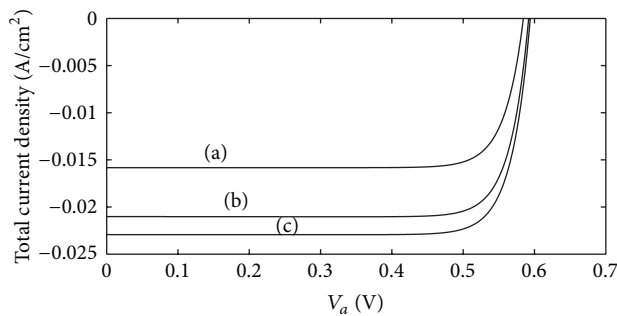


FIGURE 9: The calculated  $I$ - $V$  curves of n-i-p solar cells with different intrinsic layer materials: (a) Si, (b)  $\beta$ -FeSi<sub>2</sub>, and (c) BaSi<sub>2</sub>.

TABLE 2: The calculated results for n-i-p solar cells with different intrinsic layer materials.

Intrinsic layer materials	$V_{oc}$ (V)	$J_{sc}$ (mA/cm <sup>2</sup> )	FF (%)	$\eta$ (%)
Si	0.584	15.83	82.33	20.6
$\beta$ -FeSi <sub>2</sub>	0.591	21.02	82.59	27.8
BaSi <sub>2</sub>	0.594	22.93	82.63	30.4

## 4. Conclusion

The dc  $I$ - $V$  characteristics of  $\beta$ -FeSi<sub>2</sub> and BaSi<sub>2</sub> n-i-p solar cells are investigated by using the analytical calculations. The distributions of minority carrier densities, the diffusion current densities of free electron and hole, and the drift current density in the depletion regions are calculated. The conversion efficiencies are obtained from the calculated  $I$ - $V$  curves. The calculated results show that the conversion efficiency of  $\beta$ -FeSi<sub>2</sub> solar cell is 27.8% and that of BaSi<sub>2</sub> solar cell is 30.4%, both are larger than that of the Si n-i-p solar cell ( $\eta$  is 20.6% which is consistent with the reported results). These results are consistent with their absorption spectrum.

## Conflict of Interests

The authors declare that there is no conflict of interests regarding the publication of this paper.

## References

- [1] S. P. Murarka, "Refractory silicides for integrated circuits," *Journal of Vacuum Science & Technology*, vol. 17, p. 775, 1980.
- [2] D. Leong, M. Harry, K. J. Reeson, and K. P. Homewood, "A silicon/iron-disilicide light-emitting diode operating at a wavelength of 1.5  $\mu$ m," *Nature*, vol. 387, no. 6634, pp. 686–688, 1997.
- [3] K. Noda, Y. Terai, S. Hashimoto, K. Yoneda, and Y. Fujiwara, "Modifications of direct transition energies in  $\beta$ -FeSi<sub>2</sub> epitaxial films grown by molecular beam epitaxy," *Applied Physics Letters*, vol. 94, Article ID 241907, 2009.
- [4] G. K. Dalapati, S. L. Liew, A. S. W. Wong, Y. Chai, S. Y. Chiam, and D. E. Chi, "Photovoltaic characteristics of p- $\beta$ -FeSi<sub>2</sub>(Al)/n-Si(100) heterojunction solar cells and the effects of interfacial engineering," *Applied Physics Letters*, vol. 98, Article ID 013507, 2011.
- [5] Z. Lin, S. Wang, N. Otagawa et al., "A thin-film solar cell of high-quality  $\beta$ -FeSi<sub>2</sub>/Si heterojunction prepared by sputtering," *Solar Energy Materials and Solar Cells*, vol. 90, no. 3, pp. 276–282, 2006.
- [6] Y. Gao, H. W. Liu, Y. Lin, and G. Shao, "Computational design of high efficiency FeSi<sub>2</sub> thin-film solar cells," *Thin Solid Films*, vol. 519, no. 24, pp. 8490–8495, 2011.
- [7] K. Morita, Y. Inomata, and T. Suemasu, "Optical and electrical properties of semiconducting BaSi<sub>2</sub> thin films on Si substrates grown by molecular beam epitaxy," *Thin Solid Films*, vol. 508, no. 1-2, pp. 363–366, 2006.
- [8] D. Tsukada, Y. Matsumoto, R. Sasaki et al., "Fabrication of (111)-oriented Si layers on SiO<sub>2</sub> substrates by an aluminum-induced crystallization method and subsequent growth of semiconducting BaSi<sub>2</sub> layers for photovoltaic application," *Journal of Crystal Growth*, vol. 311, no. 14, pp. 3581–3586, 2009.
- [9] Y. Matsumoto, D. Tsukada, R. Sasaki et al., "Epitaxial growth and photoresponse properties of BaSi<sub>2</sub> layers toward Si-based high-efficiency solar cells," *Japanese Journal of Applied Physics*, vol. 49, no. 4S, Article ID 04DP05, 2010.
- [10] S. O. Kasap, *Optoelectronics and Photonics*, Pearson, 2nd edition, 2013.
- [11] S. L. Chuang, *Physics of Photonic Devices*, John Wiley & Sons, New York, NY, USA, 2nd edition, 2009.
- [12] A. Bosio and A. Romeo, *Thin Film Solar Cells: Current Status and Future Trends*, Nova Science Publishers, New York, NY, USA, 2011.

## Research Article

# Improvement of Short-Circuit Current Density in p-Ni<sub>1-x</sub>O:Li/n-Si Heterojunction Solar Cells by Wet Chemical Etching

Feng-Hao Hsu,<sup>1</sup> Na-Fu Wang,<sup>2</sup> Yu-Zen Tsai,<sup>2</sup> Ming-Hao Chien,<sup>2</sup> and Mau-Phon Houng<sup>1</sup>

<sup>1</sup> Department of Electrical Engineering, Institute of Microelectronics, National Cheng Kung University, No. 1 Dasyue Road, East District, Tainan City 701, Taiwan

<sup>2</sup> Department of Electronic Engineering, Cheng Shiu University, 840 Chengcing Road, Niasong District, Kaohsiung City 833, Taiwan

Correspondence should be addressed to Mau-Phon Houng; [mphoung@eembox.ncku.edu.tw](mailto:mphoung@eembox.ncku.edu.tw)

Received 15 June 2014; Accepted 26 August 2014; Published 21 September 2014

Academic Editor: Chien-Jung Huang

Copyright © 2014 Feng-Hao Hsu et al. This is an open access article distributed under the Creative Commons Attribution License, which permits unrestricted use, distribution, and reproduction in any medium, provided the original work is properly cited.

This study confirms that the surface texturation of window layer (Al-Y codoped ZnO) etched by diluted HCl effectively increases conversion efficiency of p-Ni<sub>1-x</sub>O:Li/n-Si heterojunction solar cells. The results show that the short circuit current density ( $J_{sc}$ ) of cell etched at 10 s increases about 8.5% compared to unetched cell, which also corresponds to the increase of efficient photoelectric conversion in NIR region as shown in external quantum efficiency spectra. It is attributed to the increase of light transmittance of AZOY thin films in the NIR region and the effective light path of the NIR wavelength, which results in increasing of light absorption in the base layer.

## 1. Introduction

A type of silicon heterojunction solar cell, called heterojunction with intrinsic thin-layer (HIT), developed by Sanyo Ltd., in 1994, offers low temperature (<250°C) process for high-efficiency solar cells compared to crystalline silicon solar cells with diffused p-n junctions. Today, the ultra-high conversion efficiency of 25.6% (area = 143.7 cm<sup>2</sup>) has been achieved in HIT solar cell, April 2014. However, the cell still exhibits a high process cost and technical barriers because of its complex structure, despite the fact that it can be fabricated at a rather low temperature (<250°C) [1, 2]. By comparison, the low cost transparent conducting oxide (TCO)/n-Si heterojunction solar cells (HJSCs) are more promising as high-conversion-efficiency and low cost SCs because of the advantages they offer, including a simpler device structure and a lower processing temperature (<250°C) [3–13]. In 2013, our study [14] proposed that low cost p-type Ni<sub>1-x</sub>O:Li thin film was a promising material candidate for other TCO materials (such as n-ZnO-base or n-type indium tin oxide (n-ITO)) in HJSCs applications due to the higher work function

(>5 eV), which can directly increase the built-in potential ( $V_{bi}$ ) and further increase the  $V_{oc}$ . However, the results show that the conversion efficiency of p-Ni<sub>1-x</sub>O:Li/n-Si HJSCs is only 2.33% ( $V_{oc}$ : 345 mV,  $J_{sc}$ : 22.048 mA/cm<sup>2</sup>, and FF: 0.307). We propose that the reduction of interface states ( $D_{it}$ ) of cell and the improvement of optoelectrical properties of p-Ni<sub>1-x</sub>O:Li thin films are very important issues to develop high conversion efficiency p-Ni<sub>1-x</sub>O:Li/n-Si HJSC.

The low  $J_{sc}$  value of p-Ni<sub>1-x</sub>O:Li/n-Si HJSCs is a serious problem to limit the conversion efficiency of cell. It is mainly attributed to high reflectance of n-Si substrate (~25%), low transmittance of p-Ni<sub>1-x</sub>O:Li thin films (~50%), and light absorption loss of n-Si. Surface texturation of TCO thin films window layers by wet chemical etching is a simple and effective method to increase  $J_{sc}$ , which has been reported in many solar cells applications [15–18]. This method performs light scattering to increase the effective light path in a solar cell to enhance overall absorption. This is the so-called “light trapping.” In fact, in these p-Ni<sub>1-x</sub>O:Li/n-Si HJSCs, a high conductivity (high mobility) and dense Al-Y codoped ZnO (AZOY) thin film is deposited on p-Ni<sub>1-x</sub>O:Li thin films as

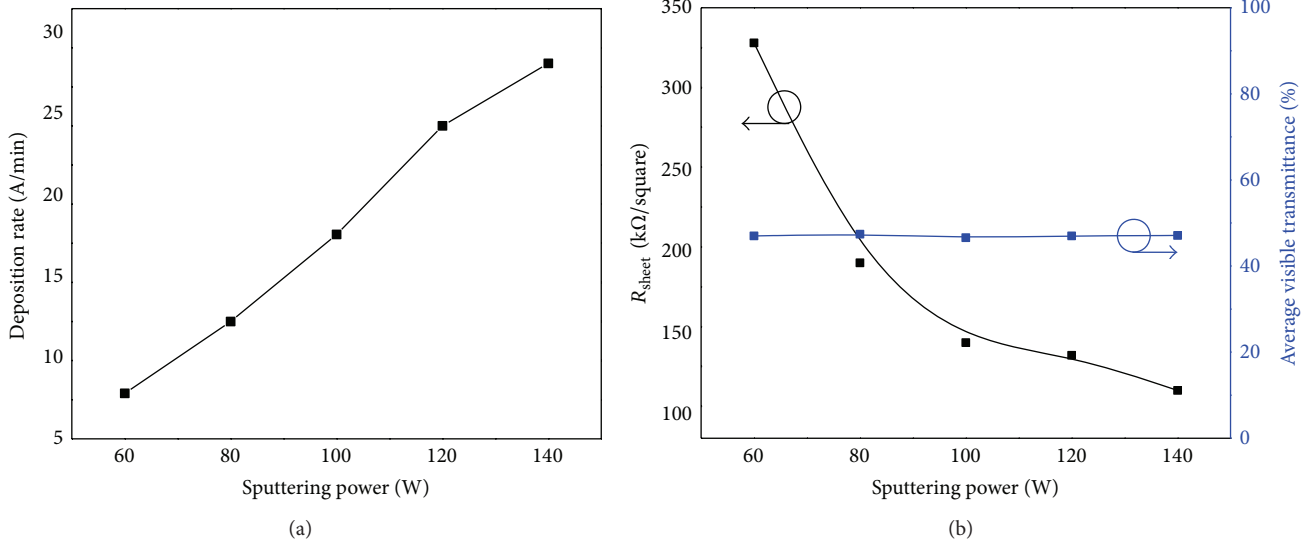


FIGURE 1: Dependence of (a) deposition rate and (b) sheet resistance ( $R_{sheet}$ ) and average visible transmittance (400–800 nm) on the sputtering power for p- $Ni_{1-x}O:Li$  thin films.

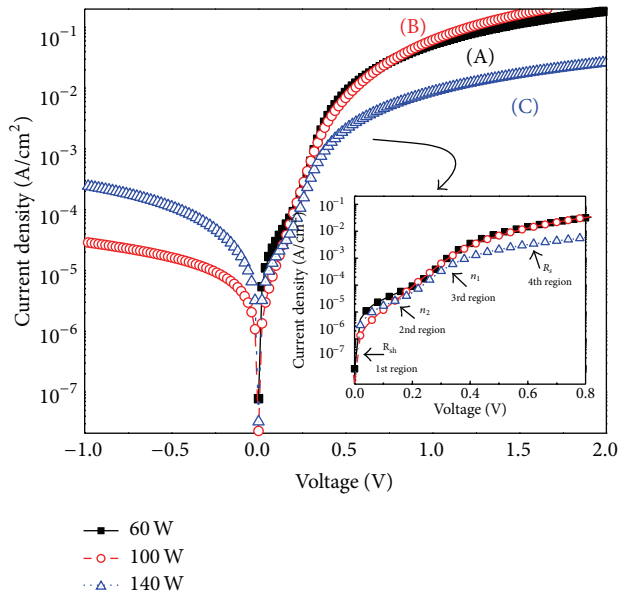


FIGURE 2: Dark current density-voltage ( $DJ-V$ ) curve of p- $Ni_{1-x}O:Li/n-Si$  HJ fabricated at sputtering power of 60 W (line A), 100 W (line B), and 140 W (line C).

a front electrode contact layer (or called window layer). Thus, an appropriate postdeposition etching for AZOY thin film may increase  $J_{sc}$  of p- $Ni_{1-x}O:Li/n-Si$  HJSCs.

In this study, the effects of sputtering power on the optoelectrical properties of p- $Ni_{1-x}O:Li$  thin films were first investigated. And then, low cost p- $Ni_{1-x}O:Li/n-Si$  HJSCs were fabricated, and wet chemical etching with diluted HCl was used to produce the AZOY surface texture. The effect of wet etching on film surface morphology and cell performance was also investigated.

## 2. Experiment

P-type Li-doped  $Ni_{1-x}O$  (p- $Ni_{1-x}O:Li$ ) thin films were deposited on glass and n-type silicon (1 0 0) substrates with a resistivity of 1–10  $\Omega cm$  and a 250  $\mu m$  thickness by RF magnetron sputtering with a 3-inch diameter  $NiO:Li_2O$  (98.5:1.5 wt.%, 99.9% purity) ceramic target. The glass substrates were first cleaned with standard cleaning procedures (acetone and methanol) in an ultrasonic bath for 10 min to remove grease and organic contaminations and then rinsed in deionized water. A turbo molecular pump reduced the base pressure to  $2 \times 10^{-6}$  Torr prior to deposition. In sputtering process, the working pressure was fixed at 4 mTorr in ambient Ar (6%  $O_2$ ) and the films were deposited at room temperature (RT). In order to investigate the effects of the RF sputtering power on the optoelectrical properties of p- $Ni_{1-x}O:Li$  thin films, the sputtering power was manipulated in the range of 60–140 W.

For p- $Ni_{1-x}O:Li/n-Si$  HJSC fabrication, the n-Si substrates were first cleaned by standard RCA procedures. The optimal p- $Ni_{1-x}O:Li$  thin film was then deposited on the n-Si substrate. After p- $Ni_{1-x}O:Li$  thin films deposition, high conductivity Al-Y codoped ZnO (AZOY) thin film was deposited by using RF magnetron sputtering and the Al was thermally deposited onto the back surface of n-Si as a back electrode. And then, a finger-shaped Al layer served as the front electrode. To expose the surface texture, the as-grown AZOY thin films were dipped in a diluted mixture of HCl in  $H_2O$  (0.1 M HCl) at room temperature (etching rate: approximately  $9 \pm 0.1$  nm/s). Finally, the cells area was fixed at  $1 cm^2$  by cutting four edges.

The electrical and optical properties of p- $Ni_{1-x}O:Li$  thin films were measured by four point probes and UV-visible-NIR spectrophotometer (HITACHI U-4100), respectively. A field-emission scanning electron microscope (FE-SEM, JEOL-6700) was used to observe film surface morphology.

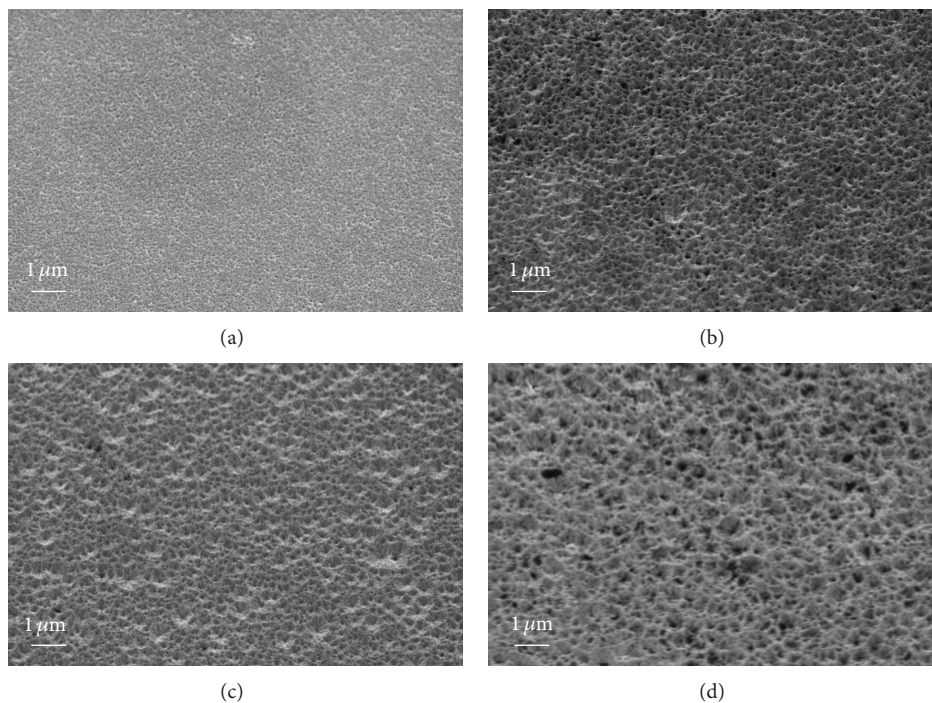


FIGURE 3: SEM micrographs (at 45° tilt) of AZOY thin films etched in 0.1 M HCl for (a) 0 s, (b) 10 s, (c) 20 s, and (d) 30 s.

The 3D images, line profiles, and surface root-mean-square (RMS) roughness of AZOY thin films were estimated by atomic force microscopy (AFM, BASO-SPM). The dark current density-voltage ( $J$ - $V$ ) characteristics of the device were measured by using an Agilent B 1500A semiconductor parameter analyzer. The photovoltaic characteristics of the device were tested using an AM 1.5 standard Newport #96000 solar simulator (Pecell PEC-L11) with an illumination intensity of 100 mW/cm<sup>2</sup>. External quantum efficiency (EQE) measurements were tested by filtering the Xe lamp with a monochromator; the signal was collected by a merlin detector and preamplifier.

### 3. Results and Discussion

Figure 1(a) shows the dependence of the deposition rate of the p-Ni<sub>1-x</sub>O:Li thin film on the sputtering power. A linear increase on growth rate was observed as the sputtering power increased. This indicates that the number of atoms sputtered from the target is proportional to the sputtering power. For higher sputtering power, the sputtered species get a higher energy that contributes to the film growth. These high energy particles have high surface mobility, and therefore a higher growing process at the surface takes place [19]. It also corresponds to electrical properties of p-Ni<sub>1-x</sub>O:Li thin film as seen in Figure 1(b). Clearly, the sheet resistance of films decreases from 328 kΩ/square to 110 Ω/square as the sputtering power increases from 60 W to 140 W. The variations are from improved crystallinity and reduced grain boundary scattering to charge carriers as sputtering power

increased. All of the effects lead to a decrease in the sheet resistance of the p-Ni<sub>1-x</sub>O:Li thin film. In addition, there is no significant change in average visible transmittance (400–800 nm, ~47%) for all films. However, this value, compared to other TCO films (>75%), is still low, which can be attributed to the presence of Ni<sup>3+</sup> in Ni<sub>2</sub>O<sub>3</sub> acting as color centers in Ni<sub>1-x</sub>O films [20].

The dark current density-voltage ( $DJ$ - $V$ ) curve of p-Ni<sub>1-x</sub>O:Li/n-Si HJSCs fabricated at sputtering power of 60 W, 100 W, and 140 W were shown in Figure 2. In this figure, the forward bias log  $J$ - $V$  curve for lines A and C shows four linear regions and for line B shows three linear regions (the slope of 2nd region is similar to 3rd region), separated by transition segments. The slopes in 1st and 4th regions for line B imply that it has the highest  $R_{sh}$  and the lowest  $R_s$ . In addition, if the forward-biased curve is fitted to the standard diode equation, we find that the ideality factors for line A are 3.41 (2nd region) and 1.72 (for 3rd region) and for line B are 1.94 (2nd and 3rd region) and for line C are 3.55 (2nd region) and 1.99 (for 3rd region). The ideality factor close to 2 indicates that the forward current in 3rd region is mainly limited by recombination within the junction space charge region. In particular, lines A and C show a higher ideality factor at lower voltage level (2nd region). The forward current in 2nd region can be mainly explained using a trap-assisted interface recombination model, which is attributed to the recombination of electrons from n-Si with holes from p-Ni<sub>1-x</sub>O:Li thin film, through interface states produce extra current [21, 22]. Moreover, it implies that more interface states are generated at the junction when the sputtering power is either extremely high or extremely low. This high interface

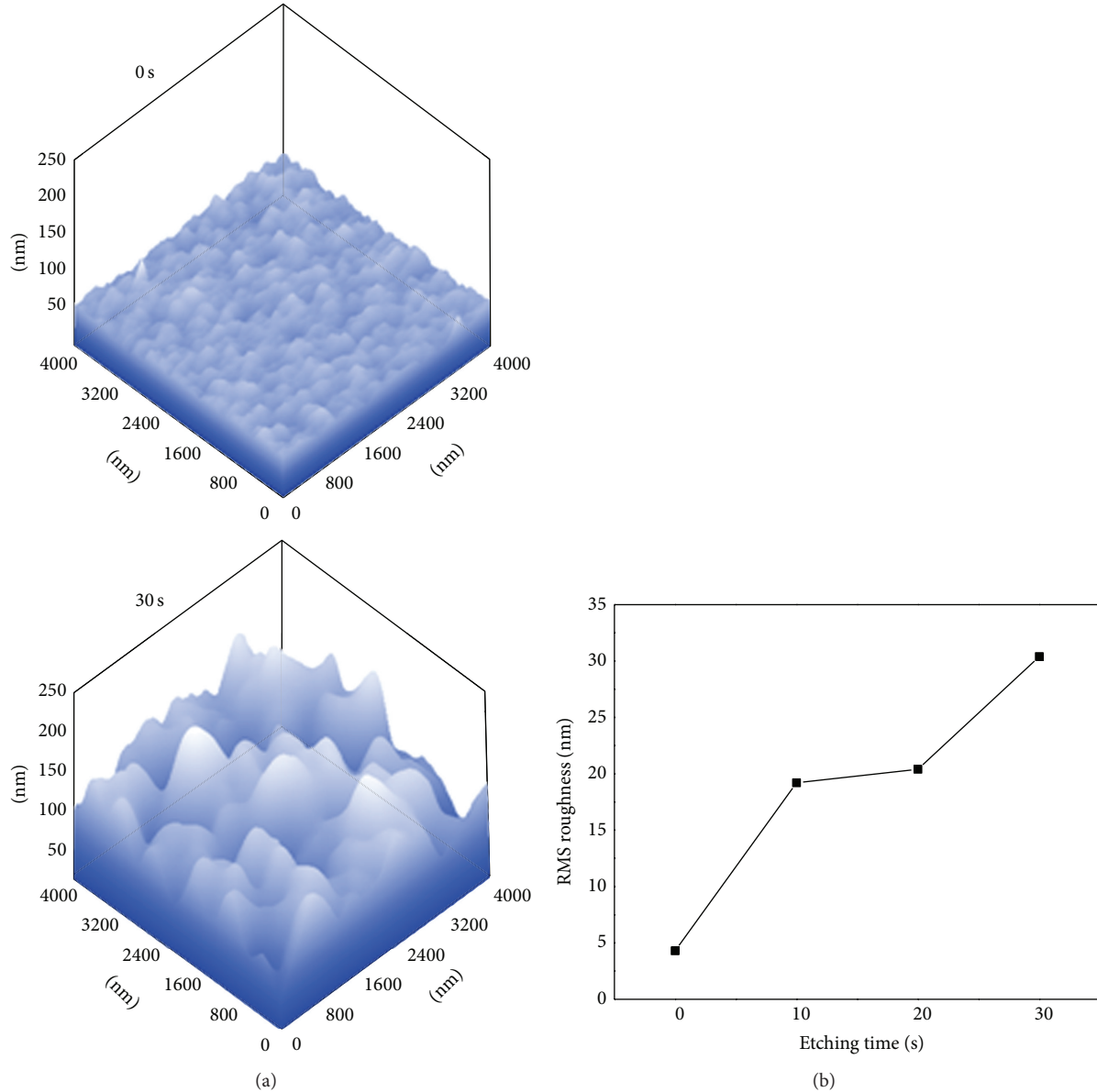


FIGURE 4: Surface RMS roughness of AZOY thin films as a function of etching time.

state can pin the Fermi level and change the  $V_{bi}$ ; they also act as recombination centers that supply a shunt to the light-generated current. Thus, we determine that the sputtering power of 100 W is the best parameter in this study.

Figure 3 shows the surface morphology (at  $45^\circ$  tilt) of AZOY thin film before and after etching. Unetched AZOY surface reveals irregular polyhedral grains with smooth morphology. After etching, the surface morphology changes from smooth to lunar landscape-like with small angles. Figure 4 shows the surface RMS roughness of AZOY thin film etched in various periods. The surface RMS roughness increases with etching time, indicating that adjusting etching time affects AZOY thin-film surface roughness. The AZOY thin-film surface RMS roughness values are estimated as  $4.3 \pm 0.12$  nm (0 s),  $19.2 \pm 0.18$  nm (10 s),  $20.4 \pm 0.17$  nm (20 s), and

$30.4 \pm 0.23$  nm (30 s). This variation in surface morphology and surface RMS roughness may affect the optical properties of films and then influence the conversion efficiency of cell.

Figure 5 shows the optical properties of AZOY thin films deposited on glass substrate etched in various periods. A clear observed oscillation in unetched AZOY thin film (between 85% and 95%) is basically the Fabry-Perot interference [23, 24]. Along with the etching process, the oscillation phenomenon disappears gradually because of the rough surface. The average visible transmittance for all AZOY thin films is approximately 91%, indicating that AZOY thin films have good light transmittance for solar cell applications. Sharp fundamental absorption edge in near ultraviolet region was observed in all spectra, corresponding to energy band gap transition of ZnO. In addition, the transmittances become

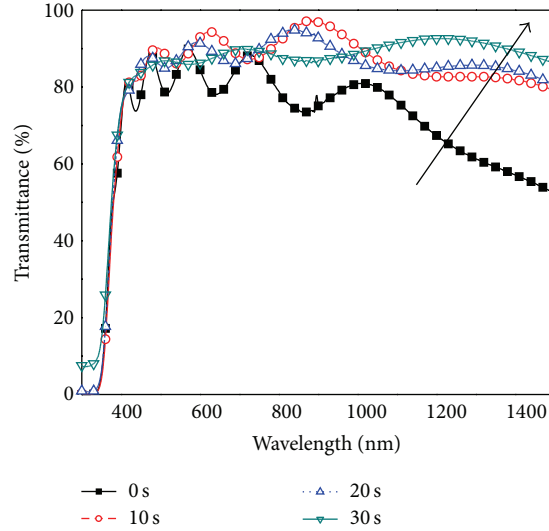


FIGURE 5: Optical transmittance of AZOY films etched in 0.1 M HCl for various etching times.

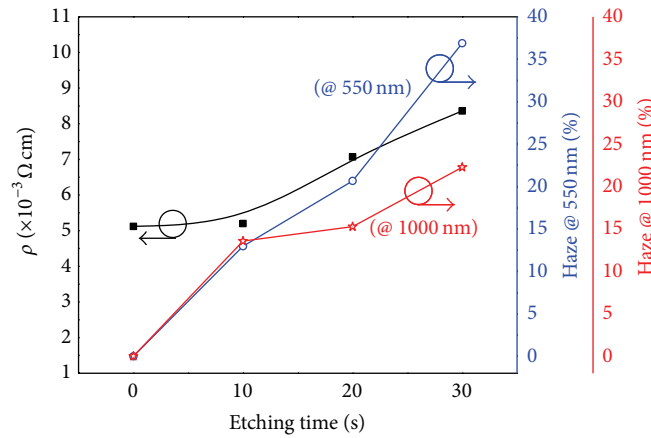


FIGURE 6: Dependence of electrical resistivity ( $\rho$ ) and haze value at 550 nm and 1000 nm on the etching time for AZOY thin films.

higher in the near infrared ray (NIR) region as etching time increases. This shifting NIR wavelength is consistent with the carrier concentration changing with etching time variation [25, 26], which can be reasoned from electrical resistivity ( $\rho$ ) of AZOY thin films (Figure 6). The unetched AZOY thin film has the lowest electrical resistivity of  $5.12 \times 10^{-3} \Omega \text{cm}$ . With an increase in etching time, the resistivity of the AZOY thin film gradually increases to  $8.36 \times 10^{-3} \Omega \text{cm}$ . The electrical resistivity is related to carrier concentration ( $n$ ) through the carrier mobility ( $\mu$ ):

$$\rho = \frac{1}{qe\mu}. \quad (1)$$

Therefore, this variation trend in resistivity may be reasoned as follows: (i) larger effective surface areas cause oxygen adsorption to trap carriers or form film defects, which results in resistivity variation. Also, the larger effective surface area affects carrier motions due to the shortened conduction

path of carriers. (ii) The grain boundary of AZOY thin film deteriorated at long etching time and formed more defect sites (areas) throughout the whole boundary [27]. These defect sites result in an increase in carrier scattering and a decrease in carrier mobility. Therefore, AZOY thin film conductivity decreases with an increase in etching time. Based on the results, the decrease of conductivity of window layer leads to an increase of the lateral resistance, which will directly increase the series resistance ( $R_s$ ) of cell. The haze values at 550 nm and 1000 nm of AZOY thin films etched at various etching times are also shown in Figure 6 and it is concluded that, by using (2) [18, 27],

$$\text{Haze} = \frac{T_{\text{diffuse}}}{T_{\text{total}}}, \quad (2)$$

where  $T_{\text{total}}$  is the total transmittance and  $T_{\text{diffuse}}$  is the diffuse transmittance. For the unetched AZOY thin film,

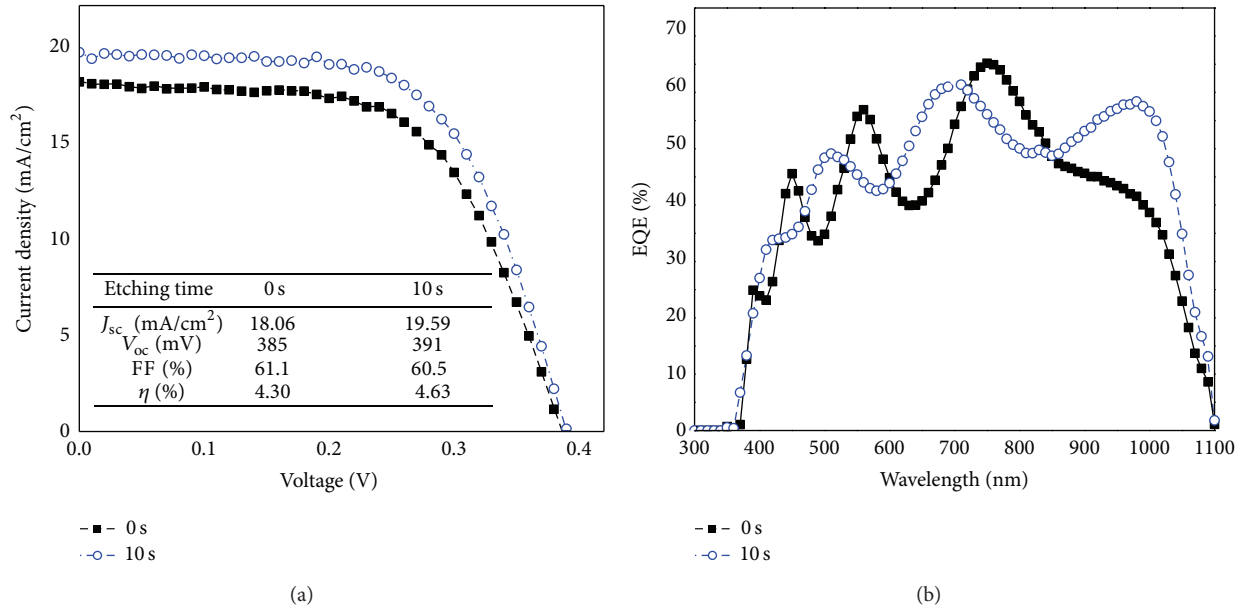


FIGURE 7: Photoelectric effect measurement of p-Ni<sub>1-x</sub>O:Li/n-Si HJSC before and after being etched for 10 s for (a)  $J$ - $V$  and (b) EQE.

the haze value is approximately 0%, indicating that disorderly polyhedral grains with smooth morphology cannot produce light scattering. After postdeposition etching, the AZOY thin film haze values increase to aid the increase in diffuse transmittance and the effect of light trapping becomes more and more obvious. This shows that surface roughness affects light scattering, especially for different lateral feature sizes.

The results show that the increase in etching time affects the series resistance ( $R_s$ ) effect (conductivity loss) and increases the light trapping effect (haze value increase) for p-Ni<sub>1-x</sub>O:Li/n-Si HJSC applications. This implies that the etching time of 10 s and 20 s should be the best choice. However, for etching time of 20 s, a very poor photovoltaic properties of cell are obtained (conversion efficiency of ~0%). This is probably because of the “through-etching” occurring earlier, due to different substrates. Therefore, we will only compare the cell before and after 10 s etching. Figure 7 shows the  $J$ - $V$  curve and EQE spectra of an p-Ni<sub>1-x</sub>O:Li/n-Si HJSC before and after 10 s etching. It shows that the  $J_{sc}$  of cell etched at 10 s increases about 8.5% compared to unetched cell. This increase of  $J_{sc}$  also corresponds to the increase of efficient photoelectric conversion in NIR region as seen in EQE spectra, which can be reasoned as the follows. (i) The light transmittance of AZOY thin films in the NIR region increases; thus, the NIR absorption in the base layer increases. (ii) Haze value affects the amount of light scattering; therefore, the effective light path of the NIR wavelength increases as the light absorption in the base layer increases. Because of these two reasons, more electron-hole pairs are formed and collected, resulting in increase of  $J_{sc}$ . Therefore, it is confirmed that wet etching in a short time is a simple and effective method to increase  $J_{sc}$  in solar cell applications.

## 4. Conclusion

This study successfully fabricates low cost p-Ni<sub>1-x</sub>O:Li/n-Si HJSC using RF magnetron sputtering. From  $J$ - $V$  curve, more interface states are generated at the junction when the sputtering power is either extremely high or extremely low. The results show that the sputtering power of 100 W is the best parameter in this study. SEM images show that AZOY thin film surface morphology changes from smooth to cratered, resulting in an increase in surface RMS roughness. The haze spectra show that surface roughness affects light scattering properties. The EQE of cells in the NIR region increases as the etching time increases, which corresponds to the  $J_{sc}$  of cell etched at 10 s increases about 8.5% (from 18.06 to 19.59 mA/cm<sup>2</sup>) compared with unetched cell.

## Conflict of Interests

The authors declare that there is no conflict of interests regarding the publication of this paper.

## Acknowledgment

The authors gratefully acknowledge the financial support from the National Science Council of Taiwan (Grant nos. NSC-102-2221-E-006-242-MY2 and MOST 103-2221-E-230-019).

## References

- [1] M. Taguchi, K. Kawamoto, S. Tsuge et al., “HITTM cells—high-efficiency crystalline Si cells with novel structure,” *Progress in Photovoltaics*, vol. 8, pp. 503–513, 2000.

- [2] Y. Tsunomura, Y. Yoshimine, M. Taguchi et al., "Twenty-two percent efficiency HIT solar cell," *Solar Energy Materials & Solar Cells*, vol. 93, no. 6-7, pp. 670-673, 2009.
- [3] J. C. Manificier and L. Szepessy, "Efficient sprayed  $\text{In}_2\text{O}_3$ : Sn n-type silicon heterojunction solar cell," *Applied Physics Letters*, vol. 31, no. 7, pp. 459-462, 1977.
- [4] F.-H. Hsu, N.-F. Wang, Y.-Z. Tsai, and M.-P. Houg, "A novel Al and Y codoped ZnO/n-Si heterojunction solar cells fabricated by pulsed laser deposition," *Solar Energy*, vol. 86, no. 11, pp. 3146-3152, 2012.
- [5] H.-W. Fang, T.-E. Hsieh, and J.-Y. Juang, "Influences of  $\text{SiO}_x$  layer thickness on the characteristics of In-Zn-O/ $\text{SiO}_x$ /n-Si hetero-junction structure solar cells," *Surface and Coatings Technology*, vol. 231, pp. 214-218, 2013.
- [6] H. Kobayashi, S. Tachibana, K. Yamanaka, Y. Nakato, and K. Yoneda, "Improvement of "indium-tin-oxide/silicon oxide/n-Si" junction solar cell characteristics by cyanide treatment," *Journal of Applied Physics*, vol. 81, no. 11, pp. 7630-7634, 1997.
- [7] O. Malik, F. J. de la Hidalga-W, C. Zúñiga-I, and G. Ruiz-T, "Efficient ITO-Si solar cells and power modules fabricated with a low temperature technology: results and perspectives," *Journal of Non-Crystalline Solids*, vol. 354, no. 19-25, pp. 2472-2477, 2008.
- [8] D. Song, A. G. Aberle, and J. Xia, "Optimisation of ZnO:Al films by change of sputter gas pressure for solar cell application," *Applied Surface Science*, vol. 195, no. 1-4, pp. 291-296, 2002.
- [9] F.-H. Hsu, N.-F. Wang, Y.-Z. Tsai, M.-C. Chuang, Y.-S. Cheng, and M.-P. Houg, "Study of working pressure on the optoelectrical properties of Al-Y codoped ZnO thin-film deposited using DC magnetron sputtering for solar cell applications," *Applied Surface Science*, vol. 280, pp. 104-108, 2013.
- [10] H. Iimoiri, S. Yamane, T. Kitamura, K. Murakoshi, A. Imanishi, and Y. Nakato, "High photovoltage generation at minority-carrier controlled n-Si/p-CuI heterojunction with morphologically soft CuI," *The Journal of Physical Chemistry C*, vol. 112, no. 30, pp. 11586-11590, 2008.
- [11] N. Gupta, R. Singh, F. Wu et al., "Deposition and characterization of nanostructured  $\text{Cu}_2\text{O}$  thin-film for potential photovoltaic applications," *Journal of Materials Research*, vol. 28, no. 13, pp. 1740-1746, 2013.
- [12] F. Gao, X.-J. Liu, J.-S. Zhang, M.-Z. Song, and N. Li, "Photovoltaic properties of the p-CuO/n-Si heterojunction prepared through reactive magnetron sputtering," *Journal of Applied Physics*, vol. 111, no. 8, Article ID 084507, pp. 084507-1-084507-4, 2012.
- [13] K. V. Rajani, S. Daniels, M. Rahman, A. Cowley, and P. J. McNally, "Deposition of earth-abundant p-type CuBr films with high hole conductivity and realization of p-CuBr/n-Si heterojunction solar cell," *Materials Letters*, vol. 111, pp. 63-66, 2013.
- [14] F. H. Hsu, N. F. Wang, Y. Z. Tsai, Y. S. Cheng, and M. P. Houg, "A new p- $\text{Ni}_{1-x}\text{O}$ : Li/n-Si heterojunction solar cell fabricated by RF magnetron sputtering," *Journal of Physics D: Applied Physics*, vol. 46, no. 27, Article ID 275104, 2013.
- [15] M. Berginski, J. Hüpkes, M. Schulte et al., "The effect of front ZnO:Al surface texture and optical transparency on efficient light trapping in silicon thin-film solar cells," *Journal of Applied Physics*, vol. 101, no. 7, Article ID 074903, 2007.
- [16] J. Springer, B. Rech, J. Müller, and M. Vaneczek, "TCO and light trapping in silicon thin film solar cells," *Solar Energy*, vol. 77, no. 6, pp. 917-930, 2004.
- [17] P. A. Basore, "Numerical modeling of textured silicon solar cells using PC-1D," *IEEE Transactions on Electron Devices*, vol. 37, no. 2, pp. 337-343, 1990.
- [18] N.-F. Wang, Y.-Z. Tsai, and F.-H. Hsu, "Effect of surface texture on Al-Y codoped ZnO/n-Si heterojunction solar cells," *IEEE Transactions on Electron Devices*, vol. 60, no. 12, pp. 4073-4078, 2013.
- [19] X. Yu, J. Ma, F. Ji et al., "Effects of sputtering power on the properties of ZnO:Ga films deposited by r.f. magnetron-sputtering at low temperature," *Journal of Crystal Growth*, vol. 274, no. 3-4, pp. 474-479, 2005.
- [20] Y. Zhou, D. Gu, Y. Geng, and F. Gan, "Thermal, structural and optical properties of  $\text{NiO}_x$  thin films deposited by reactive dc-magnetron sputtering," *Materials Science and Engineering B: Solid-State Materials for Advanced Technology*, vol. 135, no. 2, pp. 125-128, 2006.
- [21] S. Majumdar and P. Banerji, "Temperature dependent electrical transport in p-ZnO/n-Si heterojunction formed by pulsed laser deposition," *Journal of Applied Physics*, vol. 105, no. 4, Article ID 043704, 2009.
- [22] R. K. Gupta, K. Ghosh, and P. K. Kahol, "Fabrication and characterization of NiO/ZnO p-n junctions by pulsed laser deposition," *Physica E: Low-Dimensional Systems and Nanostructures*, vol. 41, no. 4, pp. 617-620, 2009.
- [23] J. Zhu, C.-M. Hsu, Z. Yu, S. Fan, and Y. Cui, "Nanodome solar cells with efficient light management and self-cleaning," *Nano Letters*, vol. 10, no. 6, pp. 1979-1984, 2010.
- [24] T. Dhakal, A. S. Nandur, R. Christian et al., "Transmittance from visible to mid infra-red in AZO films grown by atomic layer deposition system," *Solar Energy*, vol. 86, no. 5, pp. 1306-1312, 2012.
- [25] J. L. Zhao, X. W. Sun, H. Ryu, and Y. B. Moon, "Thermally stable transparent conducting and highly infrared reflective Ga-doped ZnO thin films by metal organic chemical vapor deposition," *Optical Materials*, vol. 33, no. 6, pp. 768-772, 2011.
- [26] H. Kim, A. Piqué, J. S. Horwitz et al., "Effect of aluminum doping on zinc oxide thin films grown by pulsed laser deposition for organic light-emitting devices," *Thin Solid Films*, vol. 377-378, pp. 798-802, 2000.
- [27] W. T. Yen, Y. C. Lin, and J. H. Ke, "Surface textured ZnO:Al thin films by pulsed DC magnetron sputtering for thin film solar cells applications," *Applied Surface Science*, vol. 257, no. 3, pp. 960-968, 2010.

## Research Article

# Effect of Chromium Interlayer Thickness on Optical Properties of Au-Ag Nanoparticle Array

Jing Liu,<sup>1,2,3</sup> Haoyuan Cai,<sup>2</sup> Lingqi Kong,<sup>1,3</sup> and Xianfang Zhu<sup>1,3,4</sup>

<sup>1</sup> Department of Physics, Xiamen University, Xiamen, Fujian 361005, China

<sup>2</sup> School of Information Engineering, Jimei University, Xiamen, Fujian 361021, China

<sup>3</sup> China-Australia Joint Laboratory for Functional Nanomaterials, Xiamen University, Xiamen, Fujian 361005, China

<sup>4</sup> ARC Centre of Excellence for Functional Nanomaterials, University of Queensland, St Lucia, Brisbane, QLD 4072, Australia

Correspondence should be addressed to Xianfang Zhu; zhux@xmu.edu.cn

Received 12 June 2014; Accepted 4 August 2014; Published 19 August 2014

Academic Editor: Fu-Ken Liu

Copyright © 2014 Jing Liu et al. This is an open access article distributed under the Creative Commons Attribution License, which permits unrestricted use, distribution, and reproduction in any medium, provided the original work is properly cited.

The effect of chromium interlayer thickness on optical properties of array of hybrid Au-Ag triangular nanoparticles is systematically investigated. The optical spectrum simulated by discrete dipole approximation (DDA) numerical method shows that with increase of the chromium interlayer thickness both refractive index sensitivity (RIS) and figure of merit (FOM) of localized surface plasmon resonance from the hybrid nanostructures experience remarkable change and the intensity of the extinction efficiency decreases. The nanosphere lithography (NSL) is used to fabricate the hybrid nanostructure arrays with different chromium interlayer thicknesses. The experiment demonstrates that the spectrum as measured from the as-fabricated hybrid nanostructure arrays is essentially in agreement with the simulated results.

## 1. Introduction

Noble metal nanoparticles are well known for their ability to exhibit localized surface plasmon resonance (LSPR) which can be applied in surface-enhanced spectroscopy [1], optical filters [2], plasmonic devices [3, 4], sensors [5], and so forth. The LSPR refers to the excitation of surface plasmons by light from nanometer-sized metallic particles. The position and intensity of LSPR spectrum peaks are sensitively dependent on composition, size, shape, and interparticle spacing of the nanoparticles as well as the dielectric properties of their local environments [6]. The discrete dipole approximation (DDA) is one of the most efficient computational numerical algorithms to simulate LSPR for the nanostructures with arbitrary shapes and dimensions. This method has significant advantages of occupying less computation resource, calculating the mutual action between the light and the metal nanostructures [7–10]. On the other hand, the nanosphere lithography (NSL) is the most low-cost, high-throughput method for producing periodic, geometrically tunable nanostructure arrays [11]. The

NSL makes use of a template formed by the self-assembly of monodisperse nanospheres on flat surface acting as a deposition/etching mask. Nevertheless, even with the NSL, complicated physical and chemical processes are normally involved and thus render it difficult to achieve a designed structure. One of the major problems is the adhesive ability of the deposited metallic particles to the substrate. The cohesive force and wettability of a noble metal, for example, silver or gold, are normally very limited on a glass or silicon substrate. The noble metals are inclined to be lifted off due to the abrupt change of physical and chemical properties across the interface between the metal and the substrate. Both theory and experiments suggest that an interlayer can be deposited to promote the adhesion of metallic nanoparticles to the substrates [6, 12–18]. For example, Haes et al. [6] applied chromium buffer thin film to increased adhesion of Ag nanoparticles to the glass substrate. Xilian and Jianda [13] introduced Cr intermediate layer, which reduced the surface roughness and promoted the reflectivity of Ag film. In addition, Zhu et al. [14] also focused on the study of

the influence of Cr adhesion layer on detection of amyloid-derived diffusible ligands based on localized surface plasmon resonance. To the concern of our knowledge, so far, there is no work investigating the effect of Cr interlayer thickness deposition on the periodic hybrid Au-Ag triangular nanoparticle array. The hybrid nanoparticles can prevent oxidation of pure Ag nanoparticles due to Au protective layer capped on the Ag nanoparticles [19–21]. The refractive index sensitivity (RIS) and figure of merit (FOM) of the LSPR sensor [22–27] are sensitive to the thickness of the Cr interlayer, so the influence of the Cr interlayer thickness on the optical properties and adhesive ability of the hybrid nanostructure is important as the main topic of this paper.

With above considerations, in the present paper, the effect of Cr interlayer thickness deposition on the periodic hybrid Au-Ag triangular nanoparticle array is systematically investigated. DDA method is used to calculate RIS and FOM of the hybrid nanostructure arrays with different Cr interlayer thicknesses. The hybrid nanoparticles are fabricated by NSL with polystyrene (PS) nanospheres as a deposition mask. Thermal evaporation is applied to deposit Au-Ag and Cr films. The structures of the achieved hybrid nanoparticle arrays with different Cr interlayer thicknesses are characterized by scanning electron microscope (SEM). The results suggest that the adhesive ability of the hexagonally arranged triangular Au-Ag nanoparticles to silicon substrate can be remarkably promoted by introducing a certain thickness of Cr interlayer. According to the theoretical calculations and experimental results, we obtain a suitable Cr interlayer thickness.

## 2. DDA Method

The DDA provides a convenient method for describing light scattering from nanoparticles of arbitrary shape. In DDA formalism, the object of interest, usually called “target,” is described as a cubic array lattice of electric dipoles ( $N$ -point dipoles) in which the polarizability and position vector of each dipole are specified as  $\alpha_i$  and  $\mathbf{r}_i$ , respectively. The induced dipole polarization  $\mathbf{P}_i$  in each element is determined from [7–10]

$$\mathbf{P}_i = \alpha_i \mathbf{E}_{\text{loc},i}(\mathbf{r}_i), \quad i = 1, 2, \dots, N, \quad (1)$$

where the local field  $\mathbf{E}_{\text{loc},i}(\mathbf{r}_i)$  is the sum of the field radiated from all of the other  $N - 1$  dipoles. For a given wavelength  $\lambda$ , including the contribution of all of the other dipoles, the local field can be written as

$$\mathbf{E}_{\text{loc},i}(\mathbf{r}_i) = \mathbf{E}_0 \exp(i\mathbf{k} \cdot \mathbf{r}_i) - \sum_{\substack{j=1 \\ i \neq j}}^N \mathbf{A}_{ij} \mathbf{P}_j, \quad i = 1, 2, \dots, N, \quad (2)$$

where  $\mathbf{k}$  and  $\mathbf{E}_0$  are the wave vector and the amplitude of the incident radiation, respectively. The contribution to the electric field at position  $i$  due to the dipole at position  $j$  is contained in the second term on the right side of (2) and is

normally expressed in terms of the dipole-dipole interaction matrix  $\mathbf{A}$  as

$$\mathbf{A}_{ij} \mathbf{P}_j = \frac{\exp(i\mathbf{k} \cdot \mathbf{r}_{ij})}{r_{ij}^3} \left\{ \mathbf{k}^2 \mathbf{r}_{ij} \times (\mathbf{r}_{ij} \times \mathbf{P}_j) + \frac{1 - i\mathbf{k} \cdot \mathbf{r}_{ij}}{r_{ij}^2} \times [r_{ij}^2 \mathbf{P}_j - 3\mathbf{r}_{ij} (\mathbf{r}_{ij} \cdot \mathbf{P}_j)] \right\} \quad (3)$$

$$i = 1, 2, \dots, N, \quad j = 1, 2, \dots, N, \quad j \neq i,$$

where  $\mathbf{r}_{ij}$  and  $r_{ij}$  correspond to the dipole-dipole position difference vector and magnitude that are defined as  $\mathbf{r}_i - \mathbf{r}_j$  and  $|\mathbf{r}_i - \mathbf{r}_j|$ , respectively. Substituting (2) and (3) into (1), we can generate the system of equations

$$\mathbf{A}' \cdot \mathbf{P} = \mathbf{E}, \quad (4)$$

where the off-diagonal elements of the matrix  $\mathbf{A}'_{ij}$  are the same as  $\mathbf{A}_{ij}$ , and the diagonal elements of the matrix  $\mathbf{A}'_{ij}$  are  $\alpha_i^{-1}$ .

For a system with total dipoles,  $N$ ,  $\mathbf{E}$  and  $\mathbf{P}$  are  $3N$ -dimensional vectors, and  $\mathbf{A}'$  is a  $3N \times 3N$  matrix. Solving this set of  $3N$  complex linear equations, the polarizations  $\mathbf{P}_i$  are determined, and from this we can calculate cross section of the extinction as

$$C_{\text{ext}} = \frac{4\pi\mathbf{k}}{|\mathbf{E}_0|^2} \sum_{i=1}^N \text{Im}(\mathbf{E}_{\text{loc},i}^* \cdot \mathbf{P}_i). \quad (5)$$

## 3. Results and Discussions

Using the DDA algorithm, we design and calculate the extinction spectra, RIS, and FOM of the hybrid Au-Ag triangular nanostructure arrays with different Cr interlayer thicknesses. Corresponding schematic illustration of the hybrid nanoprism is shown in Figure 1. The triangle in XY plane contains three equilateral edges, each of which is of 180 nm. The thickness of Au and Ag is fixed on  $h_{\text{Au}} = 5$  nm and  $h_{\text{Ag}} = 25$  nm and the Cr interlayer thickness,  $h_{\text{Cr}}$ , is varying from 4 nm to 20 nm. Here  $h_{\text{Au}}$ ,  $h_{\text{Ag}}$ , and  $h_{\text{Cr}}$  are defined in Figure 1(b).

Extinction is a term used in physics to describe the absorption and scattering of electromagnetic radiation. Any changes in the parameters of metal nanoparticles could lead to the optical drift in extinction spectrum and thus influence the optical applications in practice [28–31]. According to the calculated extinction spectra presented in Figure 2, when the Cr interlayer thickness is increased, the positions of peak wavelengths appear slightly blue shifted while the intensity of the extinction has obviously been decreased. The full width at half maximum (FWHM) increases rapidly by increasing thickness of Cr interlayer from 4 to 16 nm and then increases slowly with increasing Cr interlayer thickness to 20 nm. It is noted that, as can be seen from the extinction spectrum in Figure 2(a), each curve has several peaks independent of the thickness of Cr. This phenomenon not only relates to the hybrid Au and Ag material, but also relates to the optical

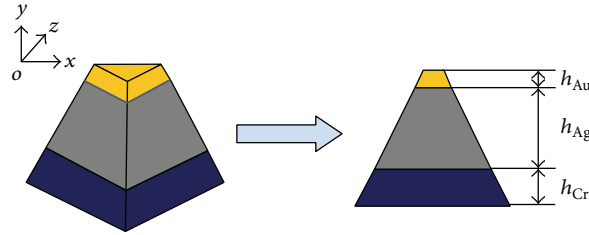
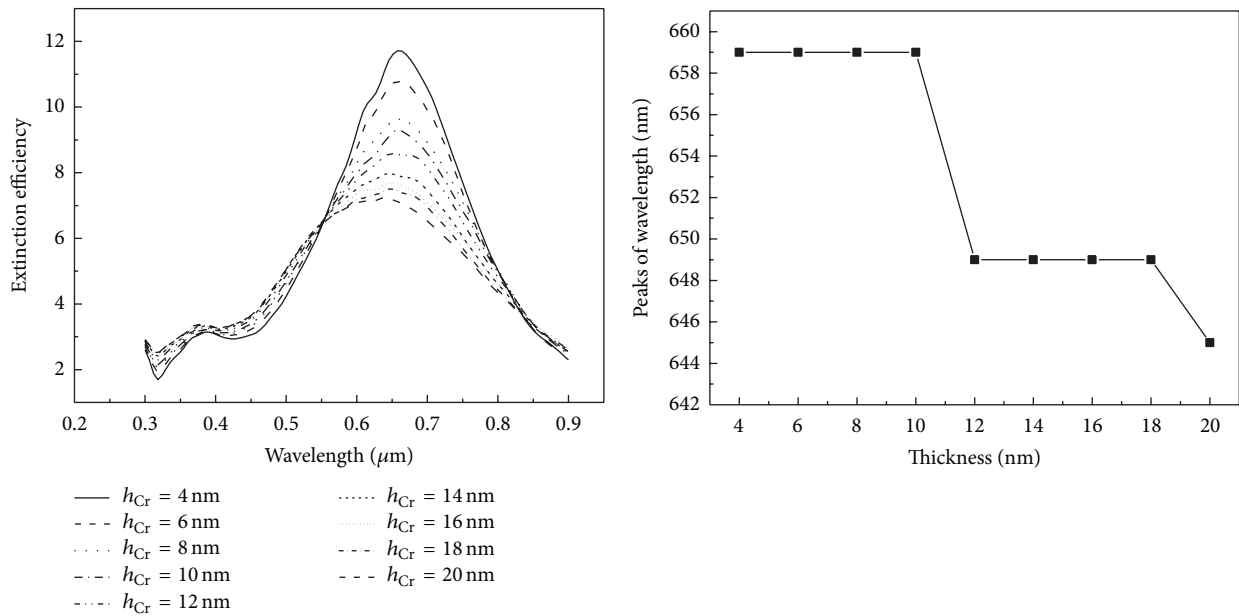
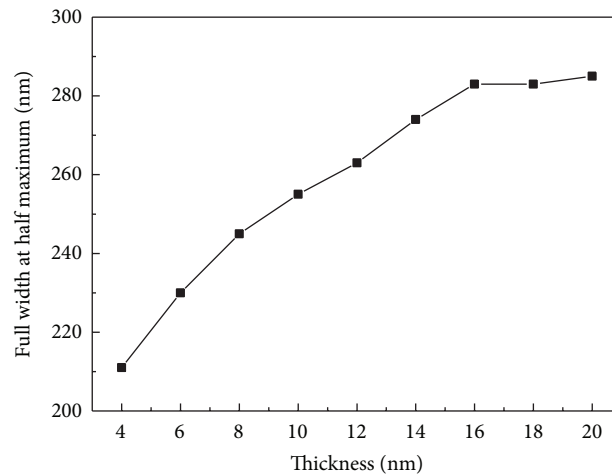


FIGURE 1: Schematic view of a single hybrid Au-Ag triangular nanoparticle.



(a) Extinction spectra for different thickness of the Cr film

(b) Peak wavelength



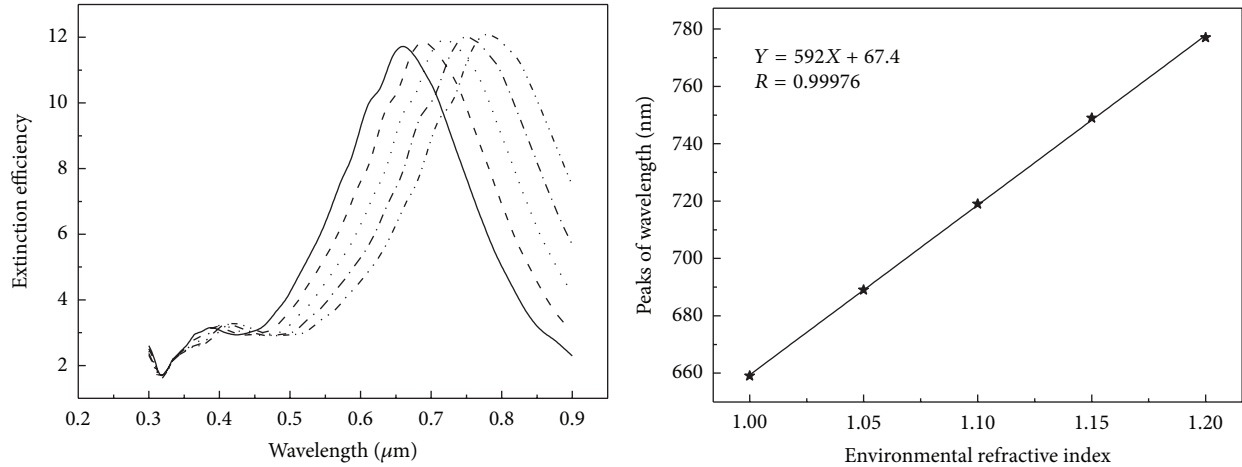
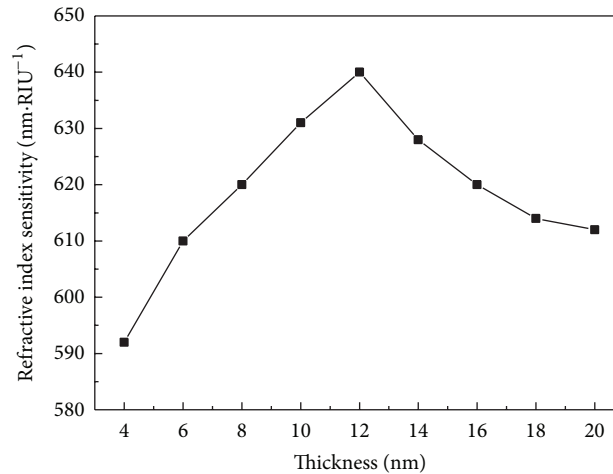
(c) Full width at half maximum as a function of the thickness of Cr film

FIGURE 2: Calculation results of the hybrid Au-Ag triangular nanoparticle arrays with different Cr interlayer thicknesses.

properties of triangular nanoparticle. For Ag or Au triangular nanoprism, the extinction spectrum always shows several peaks due to the in-plane and out-of-plane polarization [32].

In order to investigate the effect of the Cr interlayer thickness on the sensitivity of the hybrid nanostructure array,

we calculated the extinction spectra of the effective refractive index of the medium surrounding the nanostructure array. The RIS is defined as  $m = \Delta\lambda/\Delta n$  [33], where  $\Delta\lambda$  and  $\Delta n$  denote the peak of the wavelength change and the refractive index change, respectively. For the hybrid nanostructure

(a) Extinction spectra in different media for  $h_{Cr} = 4$  nm(b) Refractive index sensitivity curve for  $h_{Cr} = 4$  nm

(c) Refractive index sensitivity distributions for different Cr interlayer thicknesses

FIGURE 3: Sensing performance of the hybrid Au-Ag triangular nanoparticle arrays with different Cr interlayer thicknesses.

array with 4 nm Cr interlayer thickness, the peak wavelength has a red shift when the refractive index  $n$  increases as shown in Figure 3(a). For example, when the refractive index increases from 1.0 to 1.05, the peak wavelength shifts from 659 nm to 689 nm, exhibiting a refractive index sensitivity of 592 nm/RIU (refractive index unit), as indicated in Figure 3(b). Figure 3(c) shows the RIS of the hybrid nanostructure arrays with different Cr interlayer thicknesses. The result shows that the RIS increases with the thickness of Cr interlayer from 4 to 12 nm and then decreases with further increase of Cr interlayer thickness to 20 nm. When the Cr interlayer thickness is increased from 10 to 14 nm, the structure is very sensitive for the refractive index from 1.0 to 1.2, and the RIS is higher than the other thickness.

The FOM for a metal nanostructure is defined as  $p = S/W$  [34], where  $S$  and  $W$  denote the RIS and FWHM, respectively.

According to Figures 2(c) and 3(c), we calculated the FOM and the calculation result is shown in Figure 4. It can be seen from Figure 4 that the thickness of the Cr interlayer causes the change of the FOM of the nanostructure array. The FOM generally decreases with the increasing thickness of Cr thickness; moreover, the FOM at 4–8 nm and 12–16 nm shows more abrupt change than those at 8–12 nm and 16–20 nm. From the calculated results, we can see that the FOM of the hybrid nanostructure array keeps at a more stable and relatively high value (the value less descended), when the thickness of Cr interlayer increases from 8 to 12 nm.

#### 4. Fabrication of Nanostructures

The PS nanospheres with a mean diameter of 360 nm and a concentration of 10 wt% in solution are purchased from

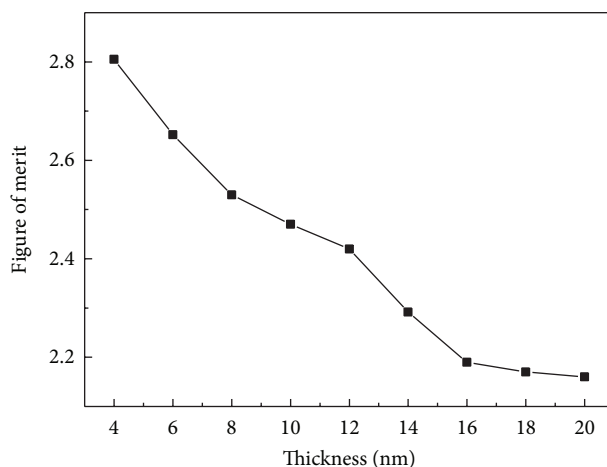


FIGURE 4: Figure of merit of the hybrid Au-Ag triangular nanoparticle arrays with different Cr interlayer thicknesses.

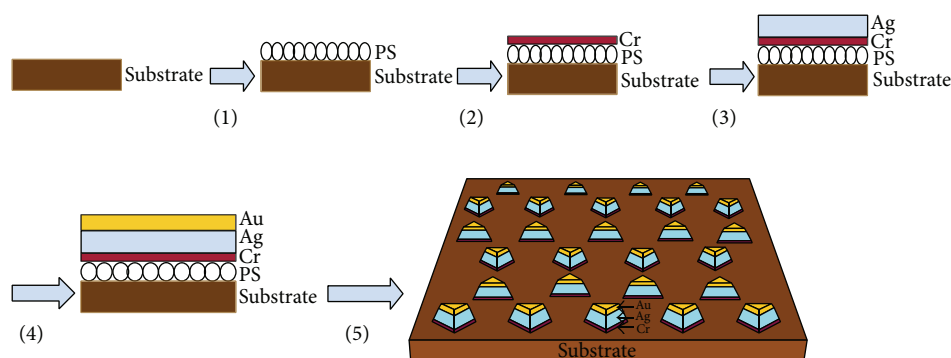


FIGURE 5: Schematic illustration of hybrid Au-Ag nanoparticle array fabrication with the following five steps: (1) drop-coating of monolayered PS nanospheres on substrate; (2) deposition of a thin buffer layer of Cr film over the as-coated monolayered PS nanospheres; (3) a further deposition of a layer of Ag film following the Cr deposition; (4) final deposition of a capped layer of Au thin film on top of the Ag film; (5) a 2D hybrid Au-Ag nanoparticle array formation on substrate after left-off of the monolayered PS nanospheres.

Suzhou Nano-Micro Bio-Tech Co. Ltd. First of all, close-packed nanosphere is a prerequisite. The regular monolayer as a deposition mask is principal to achieve large-area hexagonal structure. To begin with, the PSNS solution is diluted to be 3 wt% with deionized water. The silicon substrates (*n*-type, (100) orientation) are firstly ultrasonic cleaned, in toluene, acetone, and ethanol for 10 min, respectively, and then in piranha solution ( $\text{H}_2\text{SO}_4 : \text{H}_2\text{O}_2 = 3 : 1$ ) for 2 hours to remove organic residues. To achieve a hydrophilic surface, the silicon substrates are ultrasonically bathed in  $\text{NH}_4\text{OH}$ ,  $\text{H}_2\text{O}_2$ , and  $\text{H}_2\text{O}$  solution with the ratio of 1:1:5 for 2 hours. Every sonication followed rinsing with large amount of deionized water. The cleaned substrates are stored in deionized water until used.

Following drop-coating of the PS nanospheres on the substrate, Cr, Ag, and Au layers are deposited on the PS mask sequentially, as shown in Figure 5. When the Cr interlayer is deposited on the PS mask, the tips of the acquired triangle nanoparticles are much sharper, and the density array is much larger than the other cases. It is believed that the structure of the 2D hybrid Au-Ag nanoparticle array with Cr interlayer is better than that without interlayer. The hybrid Au-Ag

particles can protect oxidation and sulfuration of the pure Ag particles from ambient environment.

The deposition of three metallic layers (3N Au, 3N Ag, and 3N Cr) is performed in a home-built thermal evaporator at a pressure of  $5.0 \times 10^{-4}$  Pa. The substrates are rotated at a speed of 16.5 rpm all through the deposition. To achieve homogeneous deposition, the power for heating-up of the source materials is carefully increased. The deposition rate is  $\sim 2.5$  nm/s for Au and Ag layers and  $\sim 4.0$  nm/s for Cr film. The thickness had been monitored using a Dektak 3 Series surface profiler to achieve an identical depth for a low reflectance. It is controlled to be 5 nm for Au film, 25 nm for Ag film, 3, 4, 8, 12, 20, and 64 nm for Cr film, respectively. After deposition of Au film, the PS spheres are lifted off by immersing in absolute ethanol for about 5 s. The PS spheres are also removed by sonication (B3500S-MT, Branson, 140 W, 42 kHz) in absolute ethanol to examine the adhesive ability of the hybrid Au-Ag nanoparticles on silicon substrates. Nanostructures of the achieved PS mask and the hybrid Au-Ag nanoparticle arrays are characterized by LEO-1530 SEM. Ultraviolet visible (UV-vis) spectra are obtained on a Varian Cary 5000 UV-Vis-NIR spectrophotometer.

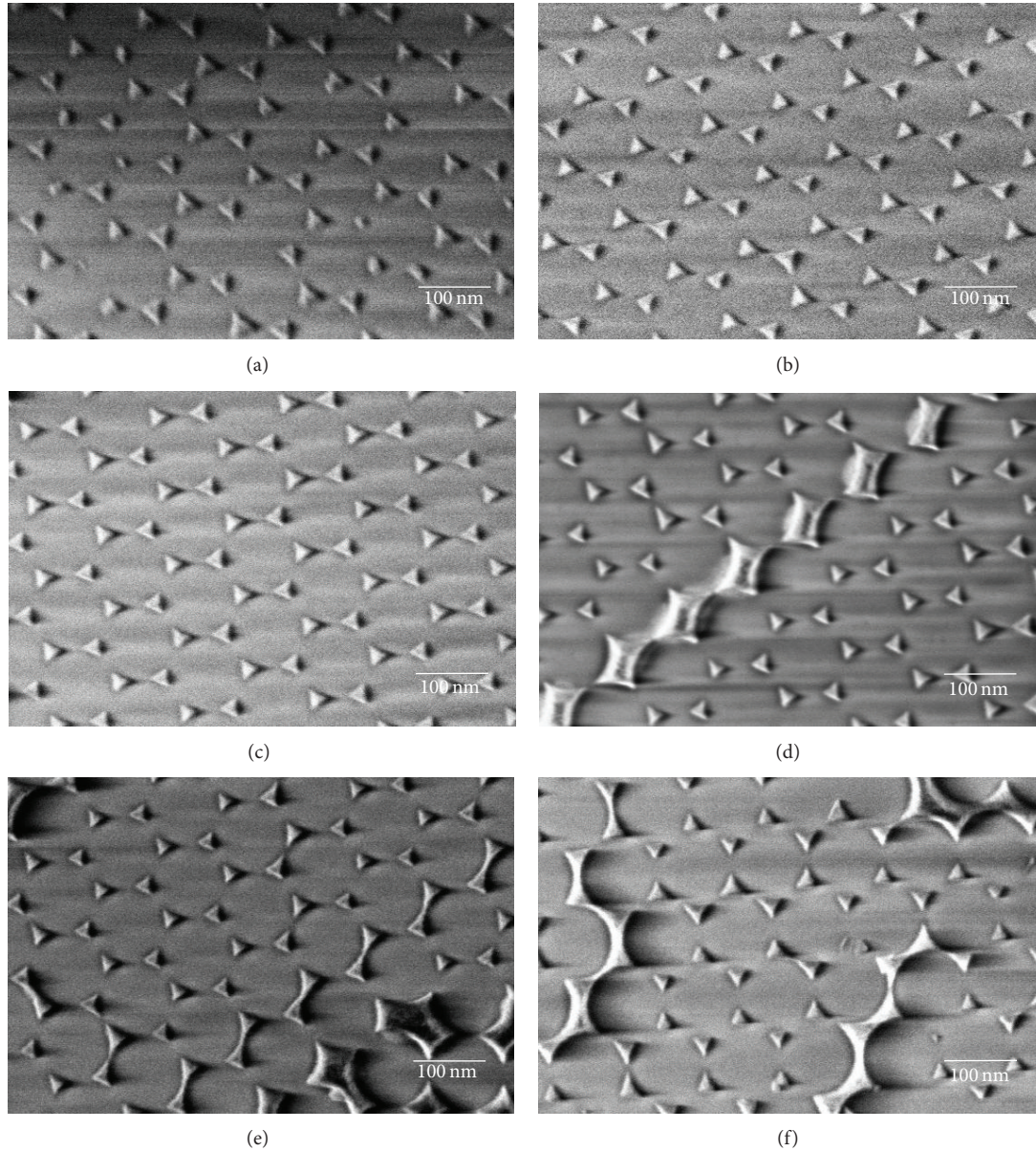


FIGURE 6: The SEM images of the Cr triangular nanoparticle arrays with different thicknesses of Cr film deposited: (a) 3 nm, (b) 4 nm, (c) 8 nm, (d) 12 nm, (e) 20 nm, and (f) 64 nm.

## 5. Results and Discussion

Figure 6 shows the SEM images of the Cr triangular nanoparticle arrays in different thicknesses. Figure 7 shows the SEM images of the hybrid Au-Ag triangular nanoparticles arrays with the different thicknesses of the Cr films.

As showed in Figure 7(a), the hybrid nanoparticles exhibit a hexagonally arranged disc structure rather than triangular structure and many tiny cracks appear in the structure. When the thickness of deposited Cr film is 3 nm, the cohesive force between the PS nanospheres and the silicon substrate seems not to be strong enough, as shown in Figure 6(a). However, as the deposited Cr film thickness increases, the cohesive force between the PS nanospheres and the silicon substrate seems

enhanced; thus the angular structure mounts and tends to be regular or well-defined, as shown in Figure 6(b). After the Ag and Au layers are deposited, the nanoparticles still exhibit similar morphology of the hybrid Au-Ag triangular nanoparticles arrays, as shown in Figure 7(b). As showed in Figure 6(c), when the Cr interlayer thickness is 8 nm, the angular structure turns into regular shape, and its tip becomes sharp. The Cr interlayer of this thickness can be used to improve the structure of the hybrid Au-Ag triangular nanoparticles arrays. After the Ag and Au layers are deposited, the nanoparticles still exhibit similar morphology of the hybrid Au-Ag triangular nanoparticles arrays, as shown in Figure 7(c). As can be seen from Figures 6(d) to 6(f), with the further increase in the thickness of the predeposited Cr

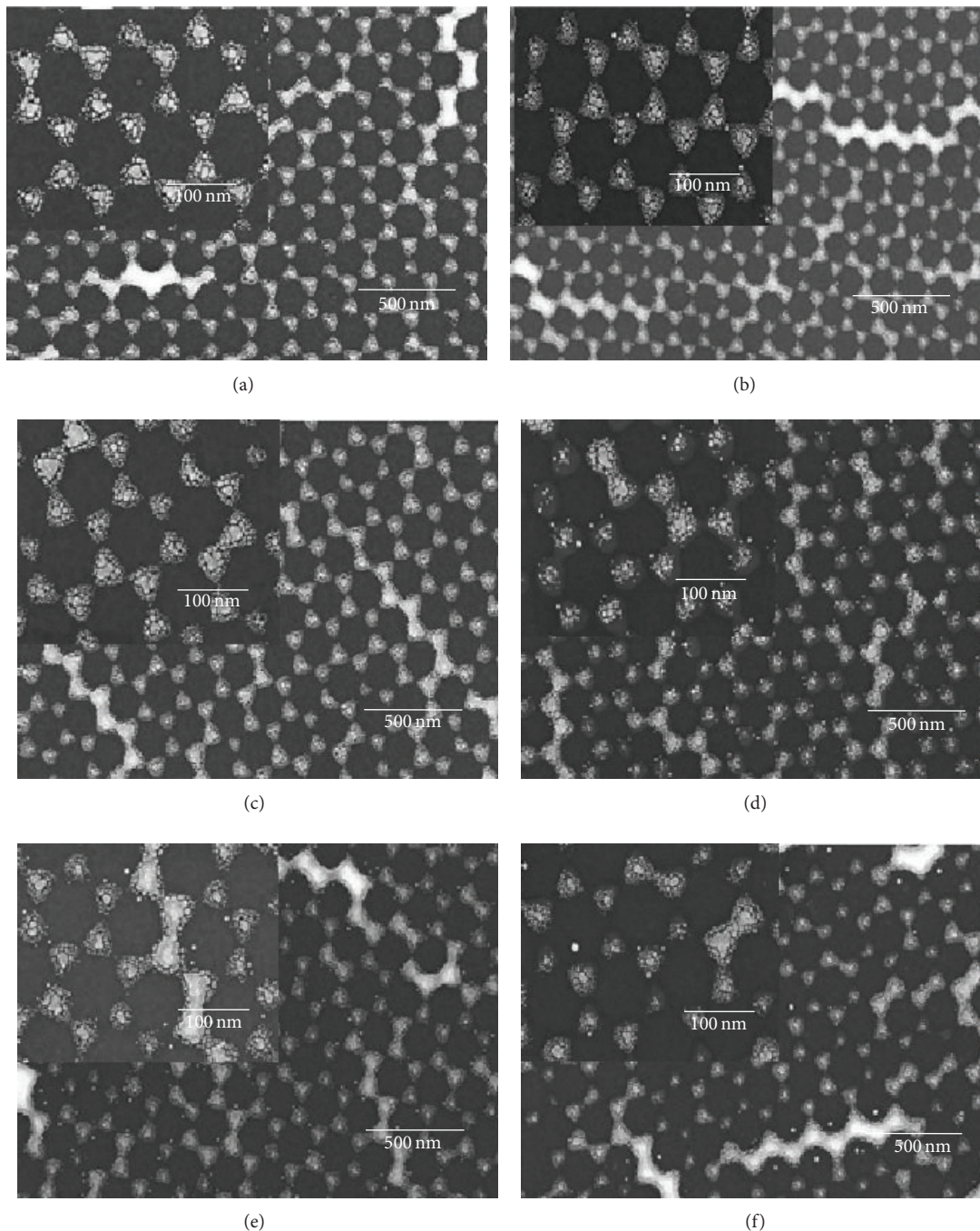


FIGURE 7: The SEM images of the hybrid Au-Ag triangular nanoparticle arrays; the Cr interlayer thickness is 3, 4, 8, 12, 20, and 64 nm, respectively.

film, the Ag and Au deposition in the gap interspaces among the spheres seem to become increasingly blocked with the predeposited Cr nanoparticles, which makes the Au and Ag particles difficult to arrive at the silicon substrate. In doing so, after the PS spheres are removed by sonication in absolute ethanol, the nanoparticles still exhibit a triangular but less uniform structure than the previous cases, as in Figures from 7(d) to 7(f). When thickness of Cr is 3 nm and 8 nm, the hybrid nanoparticles both form a large-scale monolayer array

with the hexagonally close-packed structure. Considering the theoretical calculations and experimental results, 8 nm Cr interlayer thickness is selected in the further experiment.

In the experiments, we detected the extinction efficiency of the representative hybrid Au-Ag triangular nanoparticle array with 8 nm thickness of the Cr interlayer. The experimental and the calculated results are shown in Figure 8. It can be seen apparently that when the wavelength is 621 nm, the extinction efficiency reaches a maximum value.

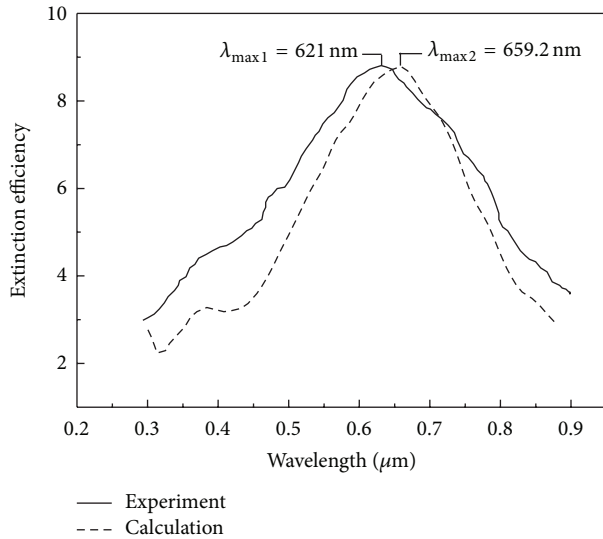


FIGURE 8: Extinction spectra of experiment and calculation.

When DDA calculation is taken to calculate the extinction efficiency, the maximum wavelength of extinction efficiency is 659.2 nm, as shown in Figure 8. The calculated result of the plasmon wavelength with the designed model agrees with recent experimental result. The only major difference with the experiment is that the experimental peak is shifted by 38 nm to the blue compared to the calculated result. This is likely caused by substrate effect (see [35]). The other reason is that fabrication error causes uniformity issue for both size and shape of the particles. In addition, in DDA calculated model, the edge of the triangular nanoparticles is straight while in experiment it is curving. Most of the results presented here are analysis and characterization of the Cr interlayer thickness variation. The results for the 2D hexagonally arranged hybrid Au-Ag triangular nanoparticles arrays show that the perfect Cr interlayer thickness is around 8 nm for our experimental fabrication. The experimental results are generally in agreement with the calculated results.

## 6. Summary

The effect of the Cr interlayer thickness deposition on the periodic hybrid Au-Ag triangular nanostructure is systematically investigated. DDA numerical method is used to study the RIS and FOM of the hybrid nanostructures. The calculation results show that the Cr interlayer thickness ranging from 8 to 12 nm is the better geometrical parameters of the hybrid nanostructures. The NSL is used to fabricate the hybrid nanostructure arrays with different Cr interlayer thicknesses. The experimental results demonstrate that when the thickness is fixed on 3 nm and 8 nm, the nanoparticles exhibit a triangular structure but that is more uniform than the other cases. From the above results, about 8 nm of Cr interlayer thickness is the suitable structure parameter which can be used to fabricate hybrid Au-Ag triangular nanoparticles array with sharp tip and regular angular structure.

## Conflict of Interests

The authors declare that there is no conflict of interests regarding the publication of this paper.

## Acknowledgments

This work was supported by National Key Basic Science Research Program (973 Project) under Grant no. 2007CB936603, Science and Technology Cooperation Plan Key Project from Fujian Province Science and Technology Department (2014–2017), the China—MOST International Sci and Tech Cooperation and Exchange Project under Grant no. 2008DFA51230, S&T Plan Projects of Xiamen City under Grant no. 3502Z20143020 and no. 2012S0484, S&T Plan Projects of Fujian Provincial Education Department under Grant no. JA11157/12200, and Scientific Research Foundation of Jimei University (PanJinlong) under Grant no. C512038.

## References

- [1] C. L. Haynes, A. D. McFarland, L. L. Zhao et al., "Nanoparticle optics: the importance of radiative dipole coupling in two-dimensional nanoparticle arrays," *Journal of Physical Chemistry B*, vol. 107, no. 30, pp. 7337–7342, 2003.
- [2] C. L. Haynes and R. P. van Duyne, "Dichroic optical properties of extended nanostructures fabricated using angle-resolved nanosphere lithography," *Nano Letters*, vol. 3, no. 7, pp. 939–943, 2003.
- [3] P. C. Andersen and K. L. Rowlen, "Brilliant optical properties of nanometric noble metal spheres, rods, and aperture arrays," *Applied Spectroscopy*, vol. 56, no. 5, pp. 124A–135A, 2002.
- [4] Y. Fu, W. Zhou, and L. E. N. Lim, "Near-field behavior of zone-plate-like plasmonic nanostructures," *Journal of the Optical Society of America A: Optics, Image Science, and Vision*, vol. 25, no. 1, pp. 238–249, 2008.
- [5] A. J. Haes, S. L. Zou, G. C. Schatz, and R. P. van Duyne, "A nanoscale optical biosensor: the long range distance dependence of the localized surface plasmon resonance of noble metal nanoparticles," *Journal of Physical Chemistry B*, vol. 108, no. 1, pp. 109–116, 2004.
- [6] A. J. Haes, W. P. Hall, L. Chang, W. L. Klein, and R. P. van Duyne, "A localized surface plasmon resonance biosensor: first steps toward an assay for Alzheimer's disease," *Nano Letters*, vol. 4, no. 6, pp. 1029–1034, 2004.
- [7] R. Jin, Y. Cao, C. A. Mirkin, K. L. Kelly, G. C. Schatz, and J. G. Zheng, "Photoinduced conversion of silver nanospheres to nanoprisms," *Science*, vol. 294, no. 5548, pp. 1901–1903, 2001.
- [8] B. T. Draine and P. J. Flatau, "Discrete-dipole approximation for scattering calculations," *Journal of the Optical Society of America A: Optics and Image Science, and Vision*, vol. 11, no. 4, pp. 1491–1499, 1994.
- [9] N. Félidj, J. Aubard, and G. Lévi, "Discrete dipole approximation for ultraviolet-visible extinction spectra simulation of silver and gold colloids," *The Journal of Chemical Physics*, vol. 111, no. 3, pp. 1195–1208, 1999.
- [10] G. C. Schatz, "Electrodynamics of nonspherical noble metal nanoparticles and nanoparticle aggregates," *Journal of Molecular Structure*, vol. 573, no. 1–3, pp. 73–80, 2001.
- [11] K. H. Lee, Q. L. Chen, C. H. Yip, Q. Yan, and C. C. Wong, "Fabrication of periodic square arrays by angle-resolved nanosphere

- lithography," *Microelectronic Engineering*, vol. 87, no. 10, pp. 1941–1944, 2010.
- [12] Y. B. Zheng, B. K. Juluri, X. Mao, T. R. Walker, and T. J. Huang, "Systematic investigation of localized surface plasmon resonance of long-range ordered Au nanodisk arrays," *Journal of Applied Physics*, vol. 103, no. 1, Article ID 014308, 2008.
- [13] S. Xilian and S. Jianda, "Influence of Cr interlayer on the structure and optical properties of Ag films on glass substrate by magnetron sputtering," *Applied Surface Science*, vol. 253, no. 4, pp. 2093–2095, 2006.
- [14] S. Zhu, C. Du, Y. Fu, Q. Deng, and L. Shi, "Influence of Cr adhesion layer on detection of amyloid-derived diffusible ligands based on localized surface plasmon resonance," *Plasmonics*, vol. 4, no. 2, pp. 135–140, 2009.
- [15] G. H. Jeong, J. K. Park, K. K. Lee et al., "Fabrication of low-cost mold and nanoimprint lithography using polystyrene nanosphere," *Microelectronic Engineering*, vol. 87, no. 1, pp. 51–55, 2010.
- [16] A. Sinitskii, S. Neumeier, J. Nelles, M. Fischler, and U. Simon, "Ordered arrays of silicon pillars with controlled height and aspect ratio," *Nanotechnology*, vol. 18, Article ID 305307, 2007.
- [17] M. C. Gwinner, E. Koroknay, F. Liwei et al., "Periodic large-area metallic split-ring resonator metamaterial fabrication based on shadow nanosphere lithography," *Small*, vol. 5, no. 3, pp. 400–406, 2009.
- [18] Y. Imura, M. Kato, T. Kondo, and T. Kawai, "Strings of metal half-shells fabricated using colloidal particle monolayer as a template," *Langmuir*, vol. 26, no. 13, pp. 11314–11318, 2010.
- [19] J. Liu, H. Yang, X. Luo, W. Ma, and Y. Liu, "Investigation of localized surface plasmons resonance properties of metal composition nanoparticles," *Acta Optica Sinica*, vol. 30, no. 4, pp. 1092–1095, 2010.
- [20] Y. Fu and W. Zhou, "Hybrid Au-Ag subwavelength metallic structures with variant periods for superfocusing," *Journal of Nanophotonics*, vol. 3, no. 1, 2009.
- [21] K. Baba, T. Okuno, and M. Miyagi, "Silver-gold compound metal island films prepared by using a two-step evaporation method," *Applied Physics Letters*, vol. 62, no. 5, pp. 437–439, 1993.
- [22] G. K. Joshi, P. J. McClory, S. Dolai, and R. Sardar, "Improved localized surface plasmon resonance biosensing sensitivity based on chemically-synthesized gold nanoprisms as plasmonic transducers," *Journal of Materials Chemistry*, vol. 22, no. 3, pp. 923–931, 2012.
- [23] J. S. Sekhon, H. K. Malik, and S. S. Verma, "DDA simulations of noble metal and alloy nanocubes for tunable optical properties in biological imaging and sensing," *RSC Advances*, vol. 3, no. 35, pp. 15427–15434, 2013.
- [24] B. Spackova and J. Homola, "Sensing properties of lattice resonances of 2D metalnanoparticle arrays: an analytical model," *Optics Express*, vol. 21, no. 22, pp. 27490–27502, 2013.
- [25] G. H. Chan, J. Zhao, G. C. Schatz, and R. P. V. Duyne, "Localized surface plasmon resonance spectroscopy of triangular aluminum nanoparticles," *Journal of Physical Chemistry C*, vol. 112, no. 36, pp. 13958–13963, 2008.
- [26] C. Novo, A. M. Funston, I. Pastoriza-Santos, L. M. Liz-Marzán, and P. Mulvaney, "Influence of the medium refractive index on the optical properties of single gold triangular prisms on a substrate," *Journal of Physical Chemistry C*, vol. 112, no. 1, pp. 3–7, 2008.
- [27] E. Martinsson, M. M. Shahjamali, K. Enander et al., "Local refractive index sensing based on edge gold-coated silver nanoprisms," *Journal of Physical Chemistry C*, vol. 117, no. 44, pp. 23148–23154, 2013.
- [28] S. Samanta, P. Sarkar, S. Pyne, G. P. Sahoo, and A. Misra, "Synthesis of silver nanodiscs and triangular nanoplates in PVP matrix: Photophysical study and simulation of UV-vis extinction spectra using DDA method," *Journal of Molecular Liquids*, vol. 165, pp. 21–26, 2012.
- [29] P. Sarkar, D. K. Bhui, H. Bar et al., "DDA-based simulation of UV-vis extinction spectra of Ag nanorods synthesized through seed-mediated growth process," *Plasmonics*, vol. 6, no. 1, pp. 43–51, 2011.
- [30] L. P. Jiang, S. Xu, J. Zhu, J. Zhang, and H. Chen, "Ultrasonic-assisted synthesis of monodisperse single-crystalline silver nanoplates and gold nanorings," *Inorganic Chemistry*, vol. 43, no. 19, pp. 5877–5883, 2004.
- [31] B. Tang, J. An, X. Zheng et al., "Silver nanodisks with tunable size by heat aging," *The Journal of Physical Chemistry C*, vol. 112, no. 47, pp. 18361–18367, 2008.
- [32] K. L. Kelly, E. Coronado, L. L. Zhao, and G. C. Schatz, "The optical properties of metal nanoparticles: the influence of size, shape, and dielectric environment," *The Journal of Physical Chemistry B*, vol. 107, no. 3, pp. 668–677, 2003.
- [33] S. L. Zhu, C. L. Du, and Y. Q. Fu, "Localized surface plasmon resonance-based hybrid Au-Ag nanoparticles for detection of *Staphylococcus aureus* enterotoxin B," *Optical Materials*, vol. 31, no. 11, pp. 1608–1613, 2009.
- [34] L. J. Sherry, S. Chang, G. C. Schatz, R. P. Van Duyne, B. J. Wiley, and Y. Xia, "Localized surface plasmon resonance spectroscopy of single silver nanocubes," *Nano Letters*, vol. 5, no. 10, pp. 2034–2038, 2005.
- [35] P. C. Chaumet, A. Rahmani, and G. W. Bryant, "Generalization of the coupled dipole method to periodic structures," *Physical Review B*, vol. 67, Article ID 165404, 2009.

## Research Article

# Development of Tandem Amorphous/Microcrystalline Silicon Thin-Film Large-Area See-Through Color Solar Panels with Reflective Layer and 4-Step Laser Scribing for Building-Integrated Photovoltaic Applications

Chin-Yi Tsai<sup>1</sup> and Chin-Yao Tsai<sup>2</sup>

<sup>1</sup> Department of Applied Physics, National University of Kaohsiung, Kaohsiung 811, Taiwan

<sup>2</sup> Auria Solar, Da-Ye 1st Road 9, Sinshih, Tainan 74146, Taiwan

Correspondence should be addressed to Chin-Yi Tsai; [chinyitsai@hotmail.com](mailto:chinyitsai@hotmail.com)

Received 14 June 2014; Accepted 2 July 2014; Published 20 July 2014

Academic Editor: Chien-Jung Huang

Copyright © 2014 C.-Y. Tsai and C.-Y. Tsai. This is an open access article distributed under the Creative Commons Attribution License, which permits unrestricted use, distribution, and reproduction in any medium, provided the original work is properly cited.

In this work, tandem amorphous/microcrystalline silicon thin-film large-area see-through color solar modules were successfully designed and developed for building-integrated photovoltaic applications. Novel and key technologies of reflective layers and 4-step laser scribing were researched, developed, and introduced into the production line to produce solar panels with various colors, such as purple, dark blue, light blue, silver, golden, orange, red wine, and coffee. The highest module power is 105 W and the highest visible light transmittance is near 20%.

## 1. Introduction

Building-integrated photovoltaic (BIPV) is an important application area for photovoltaic industry and commerce [1, 2]. It not only broadens and expands the usages for photovoltaic (PV) applications but also makes solar electricity more accessible and integrated to our daily lives. In BIPV applications, photovoltaic modules or panels are fabricated as an integral part of building materials, such as windows, skylights, facades, roof covers, and exterior walls. As a result, BIPV is an ideal solution for utilizing solar electricity while maintaining buildings' architecture functions and aesthetics at the same time. However, the current mainstream commercial PV modules are made from single-crystalline or multicrystalline silicon wafers. It would be very difficult or even impossible to tailor their functions and configurations for various BIPV applications, for example, the see-through function for BIPV windows or skylights. In addition, the production of the wafer-based silicon PV modules comprises different and separate processes for polysilicon materials, wafers, cells, and modules; it could be rather involved to

commercially coordinate these different production procedures and customize their functions or configurations for designated specifications required by various BIPV applications. On the contrary, material/cell/module manufacture processes are usually integrated into one production line for thin-film solar modules. As a result, it will be relatively easier to modify these manufacture processes to commercially customize the functions or configurations of solar modules; in particular, different types of large-area substrates, such as glass, plastic, ceramic, graphite, or metal, could be employed for thin-film solar modules to meet various BIPV specifications.

Currently, there are three major types of thin-film solar cells: silicon, cadmium telluride (CdTe), and copper indium gallium diselenide (CIGS). The efficiency of CdTe and CIGS thin-film solar cells could still contend with the wafer-based silicon ones. Nevertheless, they use either precious metals such as In or toxic and hazardous metals such as Cd; certain questions and concerns still exist for their large-scale applications. Particularly, the *n*-type cadmium sulfide (CdS) used by both CdTe and CIGS thin-film solar cells contains

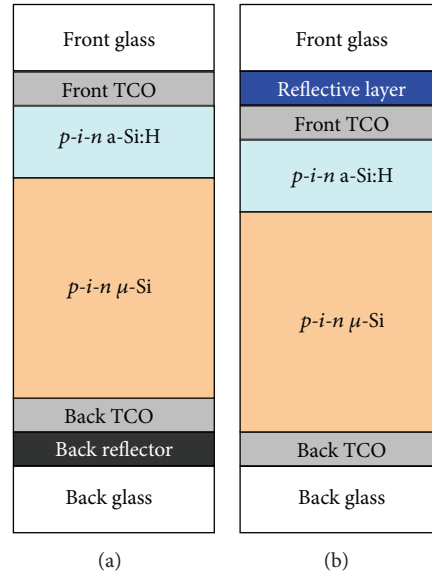


FIGURE 1: Schematic diagrams of a thin-film tandem amorphous/microcrystalline silicon solar cell of (a) a regular solar module and (b) a see-through color BIPV module.

the Cd element which remains a safety issue for their BIPV applications. Therefore, it is generally believed that silicon thin-film solar cell still has its certain advantages for BIPV applications. Moreover, it is worth mentioning that thin-film silicon solar cells generally have a lower temperature coefficient and better low light performance. For PV systems with the same value of power of kilowatt (kW), thin-film silicon ones could generate higher energy yield of kilowatt-hour (kWh). In other words, PV systems of thin-film silicon usually could generate 5 to 10 percent more electricity than other types of systems due to their lower temperature coefficient and better low light performance.

Due to the demand for specific BIPV applications, there exist some conventional methods of making BIPV panels to appear with a specifically designed color. These conventional methods include the direct attachment of an organic color film outside the module, the spray or coating of color paint on the front glass, and the utilization of a dyed front glass. These conventional methods are impractical and have their limitations and problems for commercial BIPV products. For example, organic color films and paints are usually not very durable and thus could not be compatible with the 20- to 25-year warranty associated with solar modules. Dyed front glass usually reflects too much incident sunlight which will make solar modules suffer enormous optical losses and thus have worse efficiency. From commercial consideration, additional materials incurred by these conventional methods are simply not very cost effective. As a result, in this work, many innovative technologies are researched, developed, and introduced into the production line of the large-area tandem amorphous/microcrystalline silicon thin-film solar module for BIPV applications. These novel and key technologies, including reflective layers and 4-step laser scribing, are not only compatible with the existing manufacture processes but also very cost effective. They were successfully introduced

into the production line to manufacture BIPV panels with various colors, such as purple, dark blue, light blue, silver, golden, orange, red wine, and coffee. The details of these technologies and the resulted products will be discussed in what follows.

## 2. Technologies

In this work, the tandem amorphous/microcrystalline (also called as “micromorph”) silicon thin-film solar modules are produced from the 60 MW production line of Auria Solar [3–10]. The structure of a regular cell in tandem amorphous/microcrystalline silicon thin-film solar modules is schematically shown in Figure 1(a). In general, the thickness of the front and back glasses is about 3.2 mm, the back reflector 0.5 mm, the a-Si:H cell layer 300 nm, the  $\mu$ -Si cell layer 1400 nm, the back TCO 1500 nm, and the front TCO 1800 nm. In contrast, the structure of a see-through color BIPV module is schematically shown in Figure 1(b), where the back reflector in a regular cell will be dispelled for the purpose of see-through. In addition, a front reflector, named as the “reflective layer” in this work, will be added onto the front-glass substrate to reflect a certain part of spectrum of the incident sunlight and consequently make the solar panel appear with a specifically designed color. The thickness of the reflective layer is usually several tens of nanometers according to the specification of the designed color panels.

The manufacture processes of these modules are briefly outlined in Figure 2, in which a front-glass substrate is grown with a reflective layer first. After the growth of the reflective layer, the first laser scribing process was applied onto the layer to open a “color window” for preventing the reflectively layer from blocking the subsequent laser scribing processes in which the laser beams go through the glass into the scribed material. The low-pressure chemical vapor

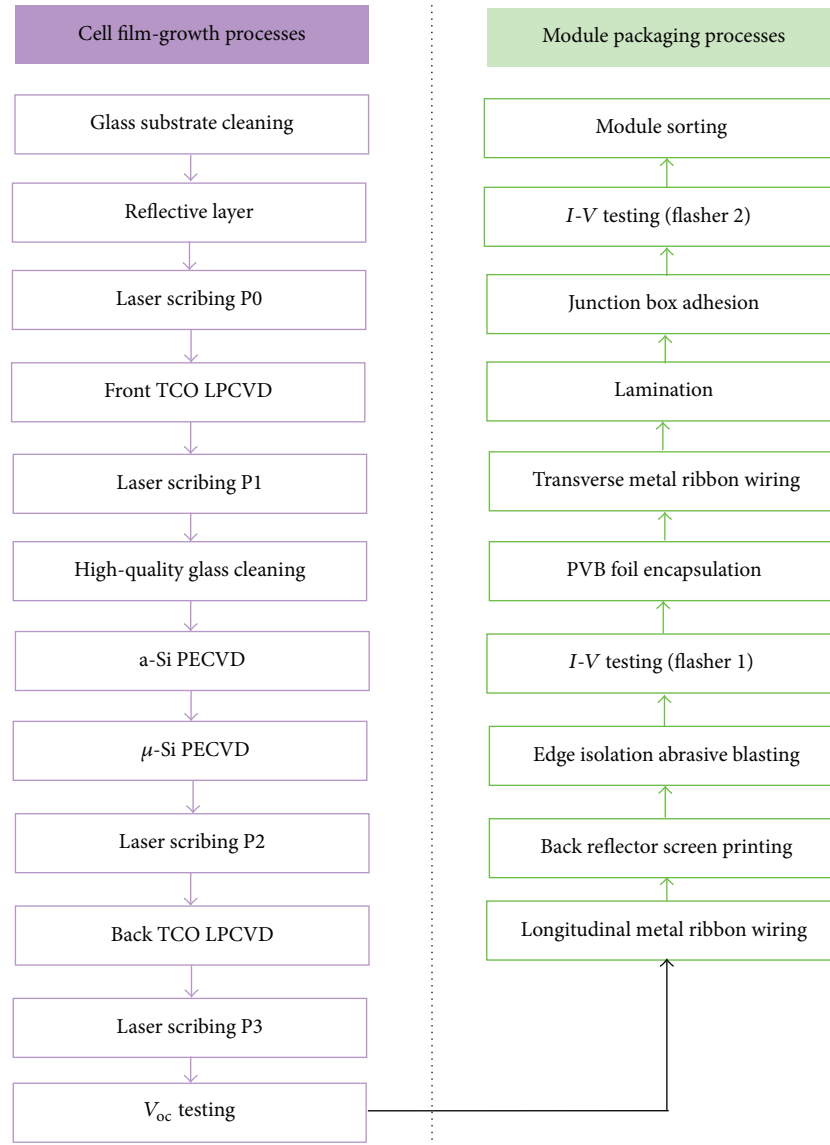


FIGURE 2: Schematic diagram illustrating the flow of manufacture processes of thin-film tandem amorphous/microcrystalline silicon see-through color BIPV modules.

deposition (LPCVD) front TCO film was then grown and the second laser scribing process was applied on it to define the physical boundaries of cells. Subsequently, the plasma-enhanced chemical vapor deposition (PECVD) hydrogen-rich amorphous silicon (a-Si:H) and microcrystalline silicon ( $\mu$ -Si) thin film was grown and the third laser scribing process was applied on it. Afterwards, the LPCVD back TCO film was grown and the fourth laser scribing process was applied on it to form the basic structure of each solar cell and serially connect them to comprise a solar module. At this stage, the panel is in fact a fully functioned photovoltaic device; yet it needs to be further packaged to become a commercial photovoltaic module. The module packaging processes involved the metal ribbon wiring, abrasive blasting edge isolation, PV foil encapsulation, lamination, and junction-box adhesion. The size of a panel is  $1.3 \text{ m} \times 1.1 \text{ m}$  which is determined by the area

of the glass substrate. A module is usually laser-scribed into 99 cells and its output voltage is regularly about 100 V.

To produce modules with see-through function and various colors appearance, many technologies were researched, developed, and introduced into the production line. These technologies are required to ensure that the color appearance is uniformly observed of the produced modules. Furthermore, the color appearance is required to maintain its uniformity on the whole area of each individual module. The throughput and yield in every production process is also demanded not to be compromised when introducing these technologies into the production line. These key technologies will be, respectively, discussed in what follows.

**2.1. Reflective Layer.** As shown in Figure 1, in order to achieve the see-through function for BIPV applications, the back

reflective layer (usually called as the “back reflector”) was removed from the regular thin-film solar modules. On the other hand, the front reflective layer was introduced between the front glass and the front TCO film to reflect parts of the incident sunlight and thus to make the panels appear with a specifically designed color. There exist some conventional methods of making BIPV panels appear with a specifically designed color. These conventional methods include the direct attachment of an organic colored film outside the module, the spray or coating of color paint on the front glass, and the utilization of a dyed front glass. These conventional methods are impractical and have their limitations and problems for commercial BIPV products. On the contrary, the reflective layer overcomes all these problems and limitations and thus makes the color BIPV panels much more cost effective for commercial products.

The reflective index of the reflective layer material and the thickness of the reflective layer should be carefully selected and designed to cooperate with the TCO and light-absorbing films to make BIPV panels appear with a specifically designed color. However, a material with high bandgap energy is normally preferred in order to minimize its light absorption. Therefore, hydrogen-rich amorphous silicon carbide (a-SiC:H) grown by PECVD was selected as the material for the reflective layer in this work because it can be fabricated by the same PECVD equipment of growing a-Si:H and  $\mu$ -Si. a-SiC:H has a higher bandgap energy than a-Si:H and  $\mu$ -Si, and it also can form a good material interface between the a-SiC:H reflective layer and the ZnO TCO film. This will certainly minimize the cost and complexity of the overall color BIPV manufacture processes. It should be noted that other materials (except PECVD-grown a-Si:H,  $\mu$ -Si, and a-SiC:H) could potentially be utilized as the reflective layer, and their performance might be possibly better than a-SiC:H. However, they could also incur additional cost and further complexity in manufacture processes when introducing them into the production lines.

The thickness of the reflective layer is several tens of nanometers. For such a nanosize film, its quality and uniformity need to be closely monitored and controlled in order to ensure that its designated reflective index and film thickness would not be compromised to yield the different color appearance. Of course, ideally, the reflective layer should be as thin as possible to minimize the light absorption. However, the film uniformity of the reflective layer is very difficult to be precisely controlled when the film thickness is at several tens of nanometers, especially for large-area thin-film solar panels. If the thickness of the reflective layer is not carefully controlled, solar panels will suffer severe problems of film nonuniformity and thus different solar panels will have different colors. In the worst case, different colors will even appear at a single solar panel that makes the product unsuitable for BIPV applications.

**2.2. 4-Step Laser Scribing.** In general, a large-area thin-film solar panel requires 3-step laser scribing processes (named as P1, P2, and P3) to partition the whole panel into several cells

and to serially connect cells into a module, as schematically shown in Figure 3. The P1 process scribes the front TCO film and thus defines the boundary of each cell. The P2 process scribes the light-absorbing film and the P3 process scribes the back TCO film and light-absorbing film. The widths of the laser scribing lines are generally determined by the spot sizes of the laser beams and usually several tens of micrometers. Since these 3-step laser scribing processes cannot be overlapped with each other, the areas occupied by them are called the “dead zones” which indicate no photocurrent being contributed from them. In this work, the laser scribing system employed diode-pumped solid-state lasers (DPSSL) with wavelengths of 355 nm for P1 and 532 nm for P2 and P3 of the 3-step laser scribing, respectively. The lasers were operated through the glass in order to minimize the scribing debris to contaminate the lenses of the laser system. As a result, if the reflective layer is grown first on the glass substrate, parts of the laser beams used in scribing the TCO and light-absorbing films will be reflected or scattered by the reflective layer. The reflection and scattering of the laser beams by the reflective layer will cause the scribing lines to be nonuniform or even broken at some places.

In order to solve this problem, an innovative method of 4-step laser scribing was devised in this work, as shown schematically in Figure 4. After the reflective layer was grown on the glass substrate, a laser scribing was employed to scribe lines on the reflective layer. The width of these lines is larger than the dead zone of the 3-step laser scribing, as shown in Figure 5. As a result, these scribing lines will generate “windows” (which are denominated as “color windows” in this work) to avoid the reflection and scattering of the laser beams in the subsequent laser scribing processes. The laser scribing for color windows combined with 3-step ones for TCO and light-absorbing films are hence called the 4-step laser scribing process. It should be noted that the laser scribing for color windows is denominated as the P0 process in order to preserve the conventional designation of P1, P2, and P3 processes.

**2.3. Pen-Type Junction Box.** For Auria’s regular solar panels, the junction box is box type one and located at the center of the upper part of the panel which of course is unacceptable to be used in the see-through BIPV panel. In order to achieve the see-through function, box-type junction boxes used in the regular solar panel were replaced by pen-type ones. The pen-type junction boxes are located at the edge of the panel to minimize their visual obstacle for the see-through function. As a result, the transverse metal wiring in the manufacture processes needs to be rearranged in order to employ the pen-type junction boxes. However, it should be noted that conventional box-type junction boxes will still be used if the see-through function is not required for specific applications.

### 3. Results and Discussion

The see-through panels without the reflective layer will appear from light brown to dark brown according to

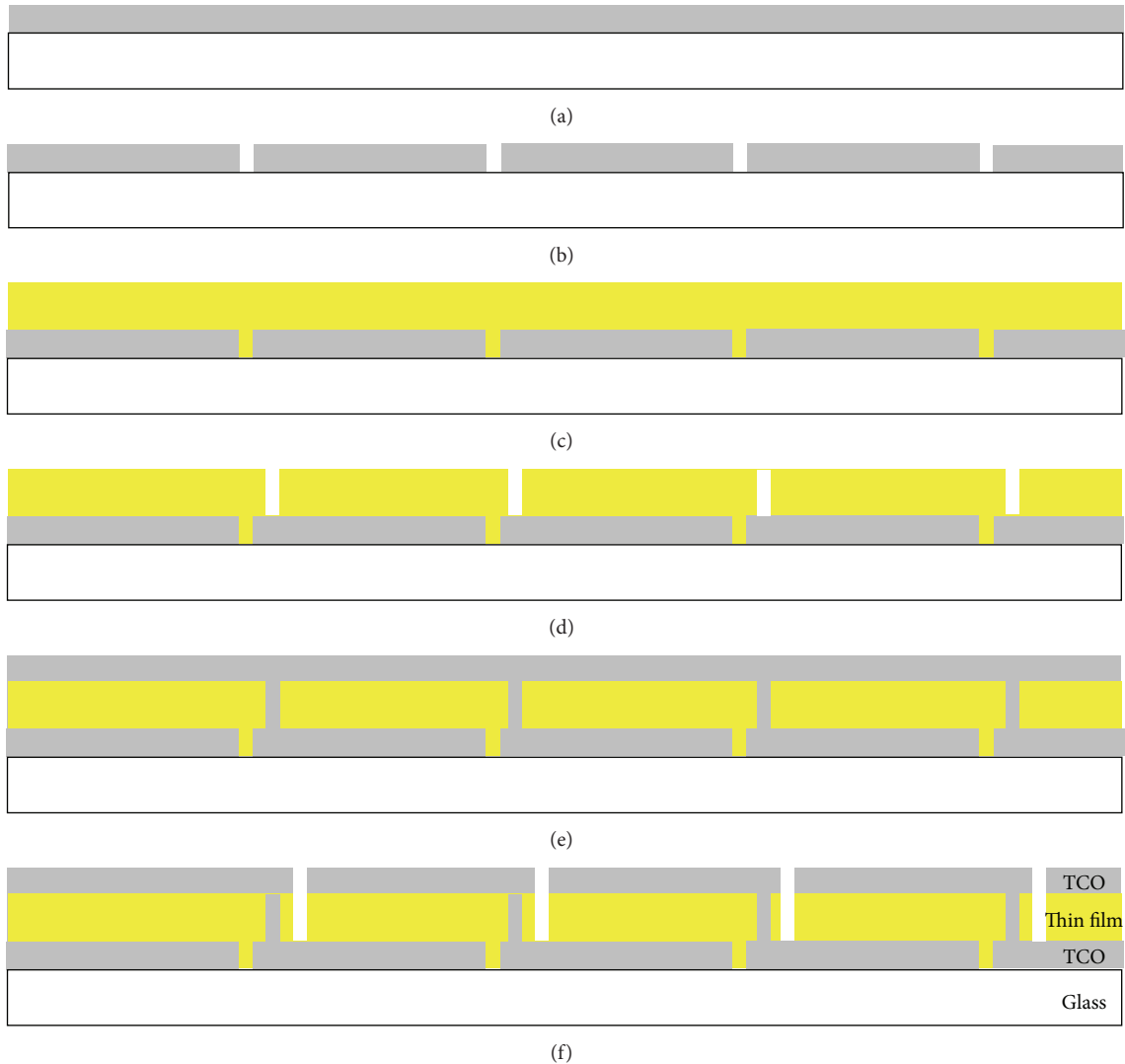


FIGURE 3: 3-step laser scribing processes of a regular thin-film tandem amorphous/microcrystalline silicon solar module. The schematic diagrams illustrate (a) the growth of the TCO film onto the glass substrate, (b) the first laser scribing process P1 on the TCO film, (c) the growth of the light-absorbing film onto the TCO film, (d) the second laser scribing process P2 on the light-absorbing film, (e) the growth of the TCO film onto the light-absorbing film, and (f) the third laser scribing process P3 on the TCO film and the light-absorbing film.

the variations of the thickness of the amorphous/microcrystalline silicon light-absorbing films, as shown in Figure 6. With the technologies of the reflective layer and the 4-step laser scribing, eight different colors of purple, dark blue, light blue, silver, gold, orange, red, and coffee tandem amorphous/microcrystalline silicon thin-film see-through solar modules were successfully designed and mass-produced in Auria's 60 MW production line, as shown in Figure 7. It should be noted that the see-through function is defined as viewing from the back glass through the front glass. If viewing from the front glass through the back glass, the light reflection from the reflective layer will dominate and the see-through function is then almost diminished as demonstrated in Figure 7. The BIPV solar panels produced by Auria are fully commercialized. They have passed not only the TÜV IEC-61646 and IEC-61730 certifications but also the IEC-61701 salt

mist test. Examples of their commercial installations are given in Figure 8.

The output power ( $P_{mpp}$ ), voltage ( $V_{mpp}$ ), current ( $I_{mpp}$ ) at the maximum peak power (mmp), open-circuit voltage ( $V_{oc}$ ), short-circuit current ( $I_{sc}$ ), and the transmittance of the visible light for these see-through BIPV modules with different colors of purple, dark blue, light blue, silver, gold, orange, red, and coffee are given in Table 1. A best-recorded regular solar module of black brown without the see-through function is also listed for the purpose of comparison. All the color modules have approximately similar open-circuit voltages, but their short-circuit currents vary significantly. The silver and gold modules have the worst output power. It should be noted that the short-circuit current has no direct correlation with the transmittance of the visible light measured at the side of the back glass. The exceptionally low output power from

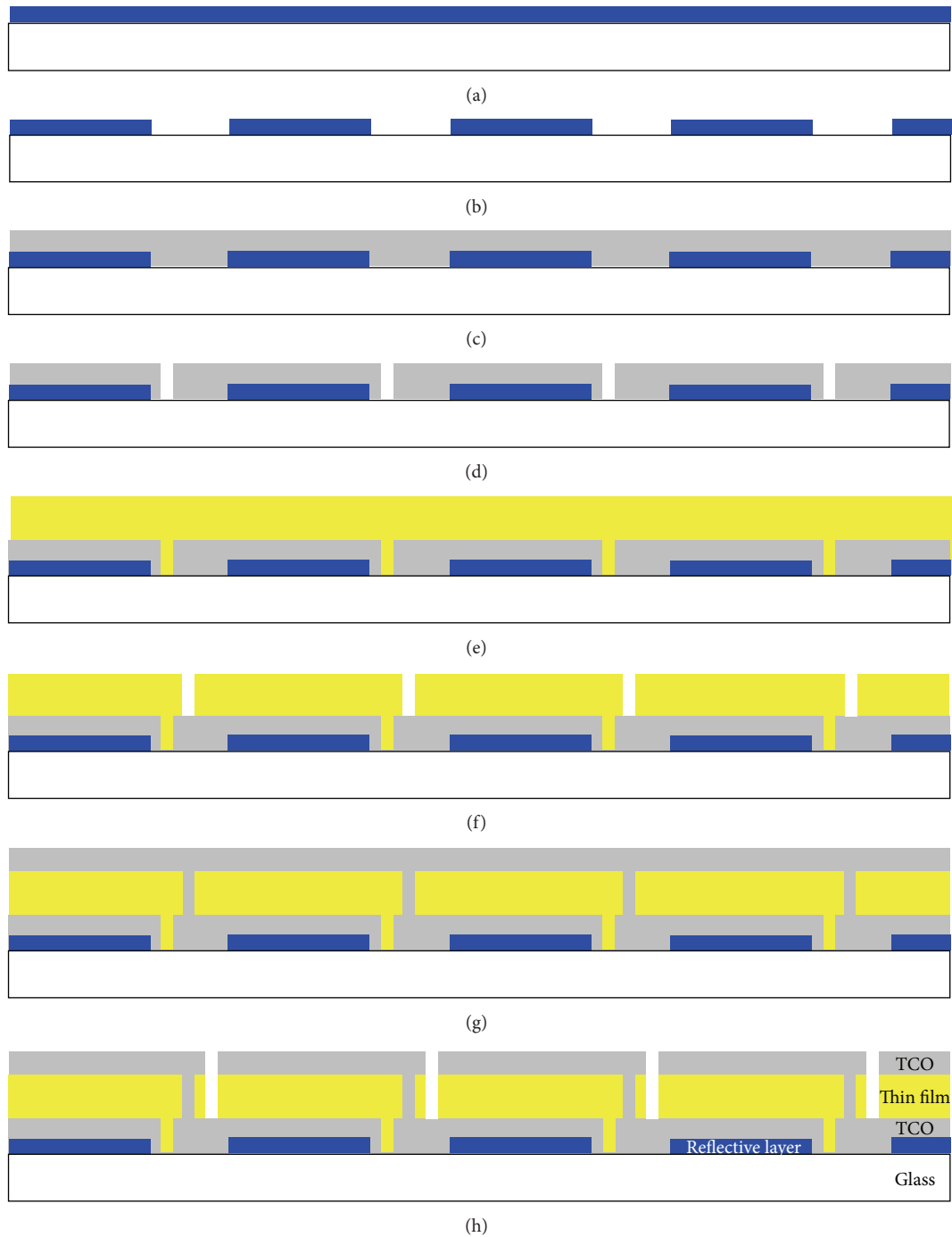


FIGURE 4: 4-step laser scribing processes of a thin-film tandem amorphous/microcrystalline silicon color see-through BIPV solar module. The schematic diagrams illustrate (a) the growth of the reflective layer onto the glass substrate, (b) the first laser scribing process P1 on the reflective layer, (c) the growth of the TCO film onto the reflective layer, (d) the second laser scribing process P2 on the TCO film, (e) the growth of the light-absorbing film onto the TCO film, (f) the third laser scribing process P3 on the light-absorbing film, (g) the growth of the TCO film onto the light-absorbing film, and (h) the fourth laser scribing process P4 on the TCO film and the light-absorbing film.

the silver and gold modules can be examined by their spectral reflectivity, as shown in Figure 9. The maximal reflected wavelengths were located at 465 nm and 625 nm for the silver and gold modules, respectively. The average magnitudes of the reflectivity of the silver and gold modules are almost twice

of those of the dark blue and purple ones. As a result, the output power of the silver and gold modules is almost half of that of the dark blue and purple ones. This example just illustrates that although the thickness of the reflective layer is just several tens of nanometers, its effect on the performance

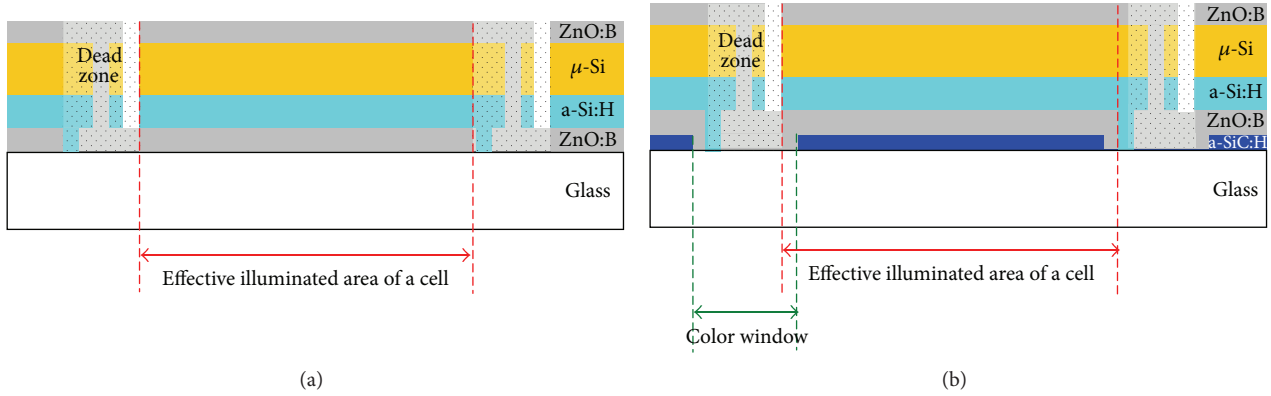


FIGURE 5: Schematic diagrams of a thin-film tandem amorphous/microcrystalline silicon solar module of (a) a regular solar module and (b) a see-through color BIPV module.

TABLE 1: The output power ( $P_{mpp}$ ), voltage ( $V_{mpp}$ ), current ( $I_{mpp}$ ) at the maximum peak power (mmp), open-circuit voltage ( $V_{oc}$ ), short-circuit current ( $I_{sc}$ ), and the transmittance of the visible light for see-through BIPV modules with different colors of purple, dark blue, light blue, silver, gold, orange, red, and coffee. A best-recorded regular solar module of black brown without the see-through function is listed for the purpose of comparison.

Solar module	$P_{mpp}$ (W; $\pm 3\%$ )	$V_{mpp}$ (V)	$I_{mpp}$ (A)	$V_{oc}$ (V)	$I_{sc}$ (A)	Transmittance (%; 400~800 nm)
Purple	75	86.1	0.89	116.3	1.03	11.6
Dark blue	75	85.2	0.88	114.7	1.01	10.9
Light blue	60	89.9	0.66	117.0	0.76	9.5
Silver	45	89.8	0.51	117.5	0.61	9.5
Gold	45	91.6	0.51	116.5	0.58	6.3
Orange	80	97.2	0.84	126.3	0.94	19.9
Red	90	95.1	0.95	124.8	1.06	16.2
Coffee	105	100.4	1.04	129.0	1.24	5.9
Regular	151	132.5	1.14	171.5	1.25	0



FIGURE 6: 4 Auria's silicon thin-film see-through BIPV modules of different film thicknesses and without the reflective layers.



FIGURE 7: 4 Auria's silicon thin-film see-through BIPV modules of different colors: dark blue, silver, gold, coffee, and purple from left to right.

of the color modules is nevertheless enormously significant. It should be mentioned that the performances of all the color modules presented here have not fully optimized yet, if compared to those of regular modules, especially to the first-rate regular module as given in Table 1. It should be noted that the see-through color thin-film modules without the back reflective layer will certainly lose a significant amount

of photocurrent in conjunction with the light-reflection loss from the reflective layer. In short, the overall manufacture parameters need to be carefully modified and properly fine-tuned to accommodate the optical and electrical properties changes from the introduction of the reflective layer on the color modules.

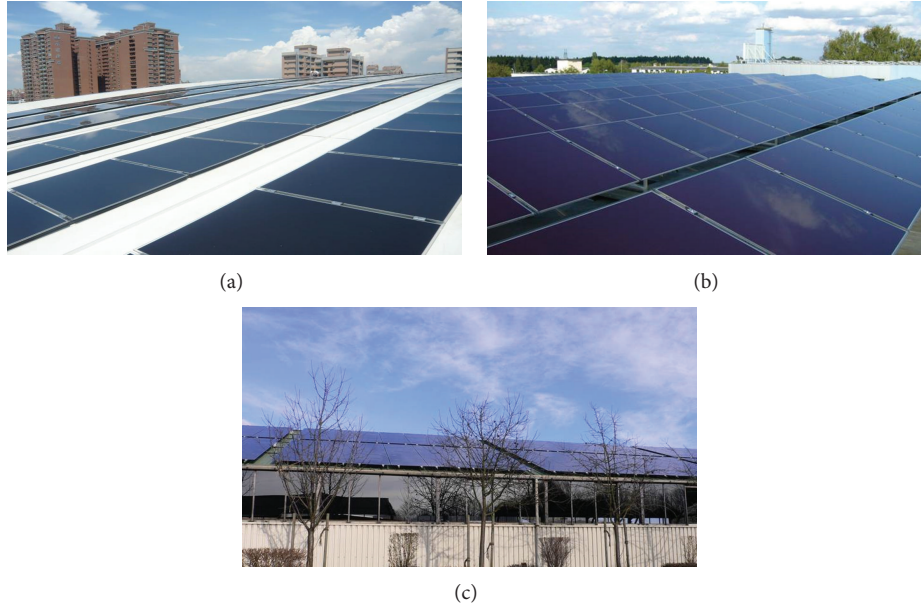


FIGURE 8: The installations of the Auria dark blue BIPV modules in 3 different locations: (a) 20.7 kW in Kaohsiung, Taiwan, (b) 78 kW in Sofia, Bulgaria, and (c) 50 kW in Dortmund, Germany.

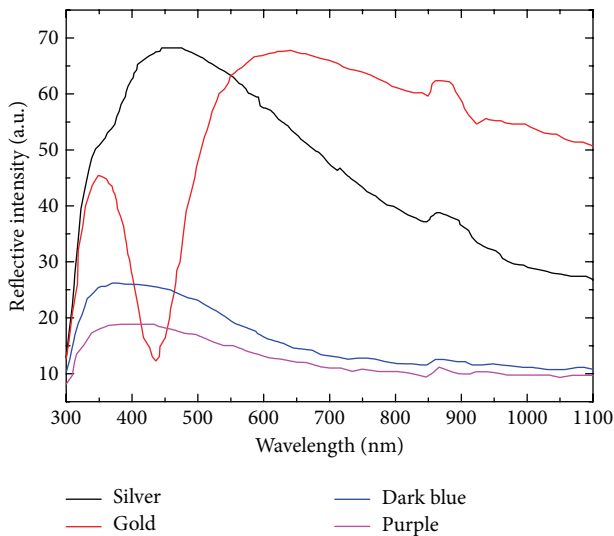


FIGURE 9: The spectrums of the reflective light intensity from thin-film tandem amorphous/microcrystalline silicon see-through BIPV modules of different colors.

#### 4. Conclusion

In this work, tandem amorphous/microcrystalline silicon thin-film large-area see-through color solar modules were successfully designed and developed for building-integrated photovoltaic applications. Novel and key technologies of reflective layers and 4-step laser scribing were researched, developed, and introduced into the production line to produce solar panels with various colors, such as purple, dark blue, light blue, silver, golden, orange, red wine, and coffee.

The highest module power is 105 W and the highest visible light transmittance is near 20%.

#### Conflict of Interests

The authors declare that there is no conflict of interests regarding the publication of this paper.

#### Acknowledgments

The authors would like to thank the help from all the colleagues in Auria Solar. This work is partially funded by the Bureau of Energy of Ministry of Economic Affairs and the National Science Council of Taiwan.

#### References

- [1] P. Eiffert and G. J. Kiss, *Building-Integrated Photovoltaic Designs for Commercial and Institutional Structures: A Source Book for Architect*, National Renewable Energy Laboratory, Golden, Colo, USA, 2000.
- [2] S. Roberts and N. Guariento, *Building Integrated Photovoltaics*, Birkhäuser, Berlin, Germany, 2009.
- [3] H. Keppner, J. Meier, P. Torres, D. Fischer, and A. Shah, "Microcrystalline silicon and micromorph tandem solar cells," *Applied Physics A: Materials Science and Processing*, vol. 69, no. 2, pp. 169–177, 1999.
- [4] A. Shah, J. Meier, E. Vallat-Sauvain et al., "Microcrystalline silicon and "micromorph" tandem solar cells," *Thin Solid Films*, vol. 403–404, pp. 179–187, 2002.
- [5] J. Meier, S. Dubail, S. Golay et al., "Microcrystalline silicon and the impact on micromorph tandem solar cells," *Solar Energy Materials and Solar Cells*, vol. 74, no. 1–4, pp. 457–467, 2002.

- [6] A. V. Shah, H. Schade, M. Vanecek et al., "Thin-film silicon solar cell technology," *Progress in Photovoltaics: Research and Applications*, vol. 12, no. 2-3, pp. 113–142, 2004.
- [7] K. Yamamoto, M. Yoshimi, Y. Tawada, Y. Okamoto, and A. Nakajima, "Thin film Si solar cell fabricated at low temperature," *Journal of Non-Crystalline Solids*, vol. 266-269, pp. 1082–1087, 2000.
- [8] K. Yamamoto, M. Yoshimi, Y. Tawada et al., "Large area thin film Si module," *Solar Energy Materials and Solar Cells*, vol. 74, no. 1–4, pp. 449–455, 2002.
- [9] K. Yamamoto, A. Nakajima, M. Yoshimi et al., "A high efficiency thin film silicon solar cell and module," *Solar Energy*, vol. 77, no. 6, pp. 939–949, 2004.
- [10] A. Nakajima, M. Gotoh, T. Sawada et al., "Development of thin-film Si HYBRID solar module," *Solar Energy Materials and Solar Cells*, vol. 93, no. 6-7, pp. 1163–1166, 2009.

## Research Article

# Characterization of the Nanoporous Template Using Anodic Alumina Method

Mau-Phon Houng,<sup>1</sup> Wei-Lun Lu,<sup>1</sup> Tsung-Hsin Yang,<sup>2</sup> and Kuan-Wei Lee<sup>2</sup>

<sup>1</sup> Institute of Microelectronics, Department of Electrical Engineering, National Cheng-Kung University, Tainan 701, Taiwan

<sup>2</sup> Department of Electronic Engineering, I-Shou University, Kaohsiung 840, Taiwan

Correspondence should be addressed to Kuan-Wei Lee; kwlee@isu.edu.tw

Received 14 April 2014; Accepted 3 June 2014; Published 30 June 2014

Academic Editor: Chien-Jung Huang

Copyright © 2014 Mau-Phon Houng et al. This is an open access article distributed under the Creative Commons Attribution License, which permits unrestricted use, distribution, and reproduction in any medium, provided the original work is properly cited.

Porous anodic aluminum oxide (AAO) is deposited on a 5 cm × 5 cm tin-doped indium oxide (ITO)/glass substrate, and the AAO/ITO/glass structure thus formed is used to reduce the amount of unreacted Al inside the AAO template, thereby reducing the transmittance of the AAO/glass structure. The enhancement of transmittance is achieved by modulating the diameter of the pores and varying the applied bias. The proposed AAO can be used at a high applied bias (up to 120 V) to improve the uniformity of the current density. Following pore-widening treatment and posttreatment annealing, the morphologies and transmittance of the AAO/ITO/glass structure were also investigated.

## 1. Introduction

Nanoporous anodic aluminum oxide (AAO) has become a commonly used material with potential applications in a wide range of areas, such as catalysis, electronics, photonics, and sensing. Owing to their regular structures and narrow size distributions of pore diameters and interpore spacings, porous alumina membranes are used in the fabrication of nanometer-scale composites [1–3]. AAO is optically transparent, electrically insulating, and mechanically robust; it is the most suitable template for nanomaterial fabrication because of its simple, intrinsically anisotropic, and self-organized porous morphology. The diameter of the pores, the pore density, and the length of the AAO template can be controlled by varying process parameters such as operating voltage, type of electrolyte acids, temperature or concentration of the electrolyte solution, and oxidation time [4–6].

The AAO method offers two main advantages. First, the fabrication of an AAO template is cost-effective and easily controlled; it yields a high aspect ratio and highly uniform pore sizes. The AAO process is better than other conventional template fabrication methods, such as atomic layer deposition [7], focused ion-beam etching [8], and

scanning probe-based nanolithography. These methods are time-consuming and uneconomical and cannot be used for large-area fabrication. Additionally, the arrangement of the pores that are formed using the traditional anodization method is highly disordered. Second, the roughness of an AZO film that is deposited on an AAO nanostructure [9, 10] can be increased by increasing the pore diameter of the AAO film, to improve light transmittance. Based on the aforementioned advantages, the nanoporous anodic alumina has great potential for use in optoelectronic devices, including thin film solar cells and light-emitting diodes. Chu et al. [11] proposed an improved method for fabricating a transparent porous alumina nanostructure; they formed it on a glass covered tin-doped indium oxide (ITO) substrate by the anodization of a sputtered aluminum (Al) layer. The ITO film was used as a conductive layer to convert the entire Al to alumina. Porous materials can be used as templates in the fabrication of various nanostructures (oxides and metals) on glass, for use in photocatalysis, dye-sensitive photocells, solar energy utilization, and so on.

This work demonstrates an AAO structure and an AAO/ITO structure on 5 cm × 5 cm glass substrates. The AAO/ITO structure is more suitable for use in optoelectronic devices

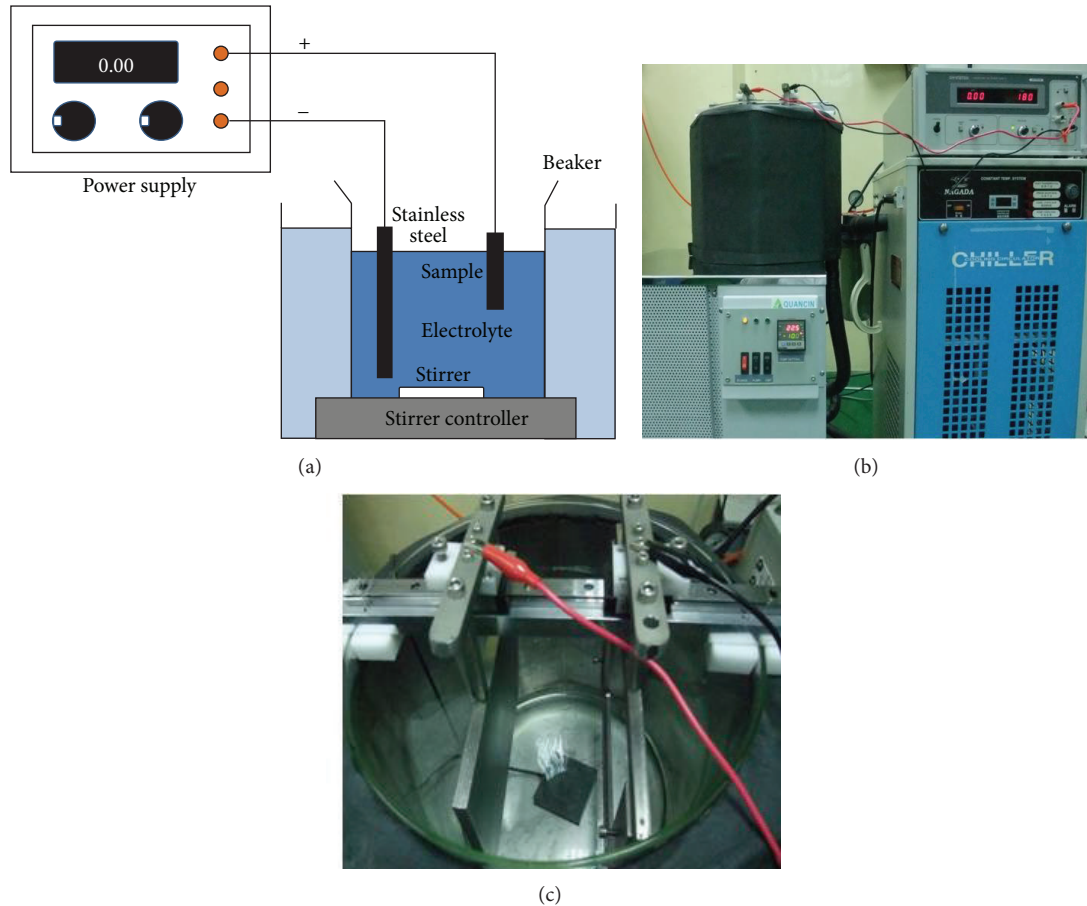


FIGURE 1: Setup for anodic oxidation: (a) experimental apparatus, (b) power supply, and (c) holder.

owing to its improved light transmittance in the near-infrared region, based on the optical transmittance of the AAO/ITO/glass structure following pore-widening treatment and posttreatment annealing. Posttreatment annealing reduces the density of defects that arise from the chemical anodic reaction and make the surface of the anodic alumina much denser and of higher quality.

## 2. Experimental

Based on previous investigations, obtaining pores with large diameters in an AAO nanostructure is difficult if only a single Al film is used as the anodizing layer. Therefore, in this work, another layer is firstly deposited on the glass substrate. Two kinds of structures are formed in this experiment. One is the Al/glass structure that is formed by depositing an Al film that is deposited on a glass substrate. The other is the Al/ITO/glass structure, which is formed by depositing an Al film on glass that has been coated with an ITO film. After the AAO and pore-widening processes, the samples with pores of various sizes in the anodic alumina structure are observed using a scanning electron microscope (SEM) (JEOL JSM-6700F). The transmittances of the AAO/glass and AAO/ITO/glass structures were measured using a UV-Vis-NIR spectrophotometer (Hitachi U-4100) at wavelengths

from 300 nm to 1100 nm. Following pore-widening treatment and posttreatment annealing, the morphology and optical transmittance of AAO/glass and AAO/ITO/glass structures were obtained.

Figure 1 schematically depicts the experimental setup for anodic oxidation. A power supply and the material of the cathode are required. However, the cathode does not participate in the oxidation process; therefore, a stable material that does not easily react is required. In this work, the cathode is made of stainless steel; the anode is the sample. The sample is placed vertically in the electrolyte such that it faces the stainless steel cathode. A beaker is utilized as a holder in the anodic oxidation experiment and its use ensures that electric field is uniform. The electrolyte is 0.3 M phosphoric acid ( $\text{H}_3\text{PO}_4$ ). A stirrer is placed in a beaker to ensure uniformity of concentration of the electrolyte during the reaction process. The beaker is put inside a cooling system, which is controlled by a bath circulator at a constant temperature. Figure 2 shows the procedure for fabricating the AAO template, which was utilized to produce the orderly array of pores.

The first step is the use of acetone solvent to remove organic contamination from the glass substrate ultrasonically for 5 minutes. The second step is the use of methanol as a solvent to remove acetone residue from the glass substrate

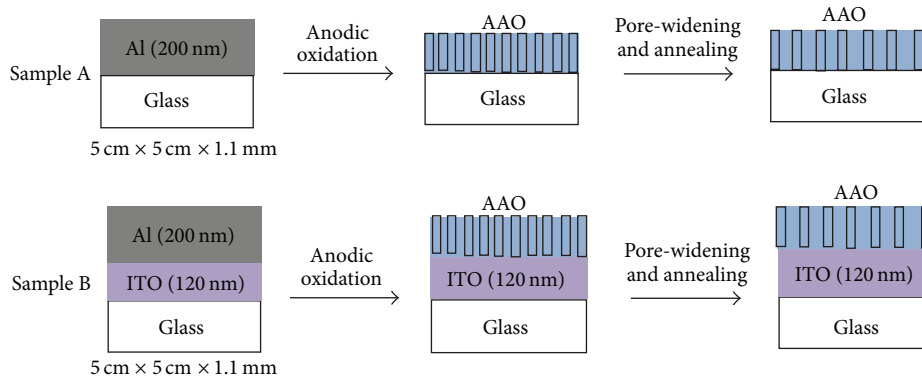


FIGURE 2: AAO process on 5 cm × 5 cm glass substrate and 5 cm × 5 cm ITO/glass substrate.

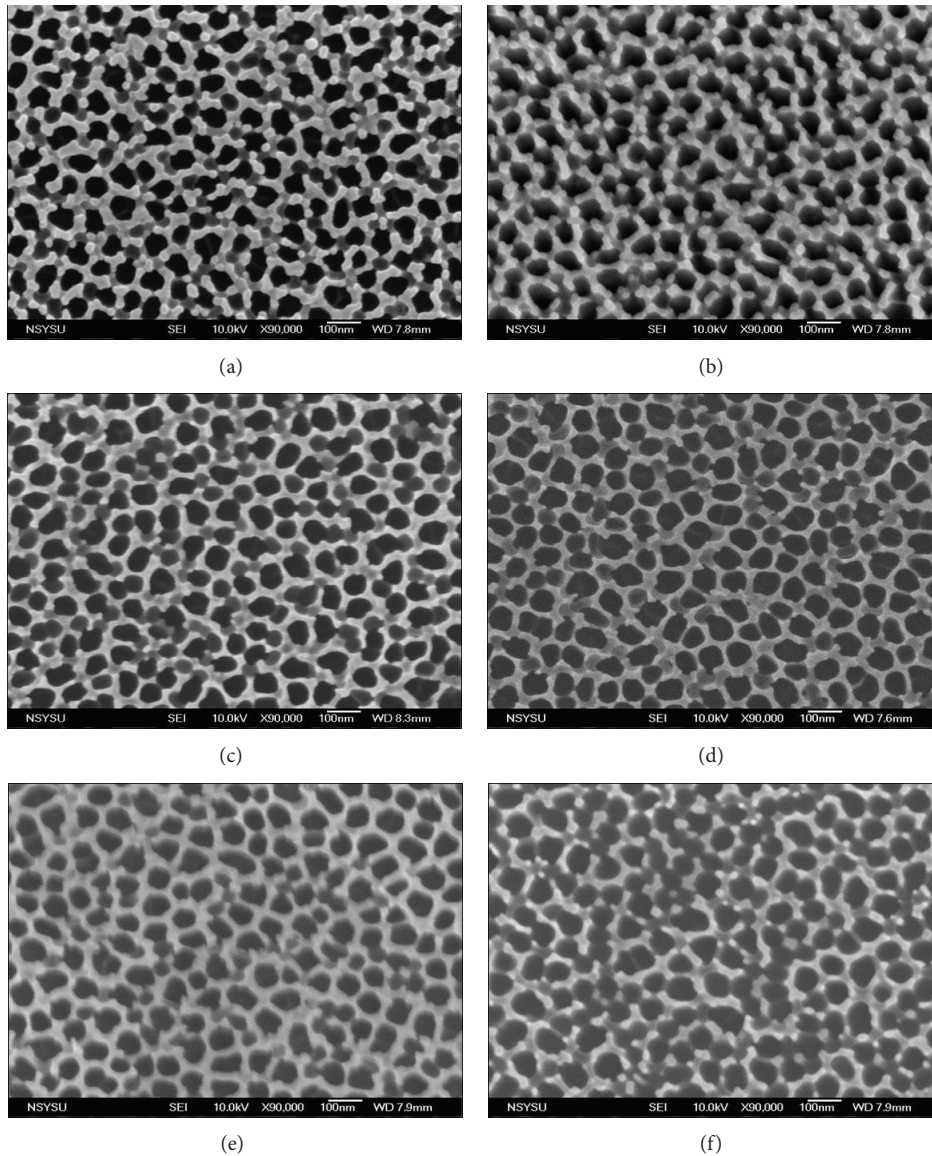


FIGURE 3: SEM micrographs of AAO films (sample A) at various concentrations: (a) 0.1 M, (b) 0.2 M, (c) 0.3 M, (d) 0.4 M, (e) 0.5 M, and (f) 0.6 M. After anodic oxidation, pore-widening treatment was performed in 6 wt%  $\text{H}_3\text{PO}_4$  at 30°C.

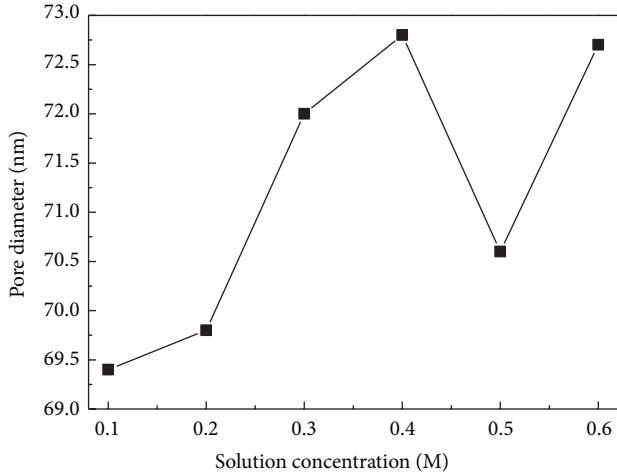


FIGURE 4: Diameter of pores in AAO/glass structures anodized using various concentrations.

ultrasonically for 5 minutes. The third step is the use of DI water to remove residual methanol from the glass substrates ultrasonically for 10 minutes, followed by drying using nitrogen gas.

A 200 nm thick Al film was deposited on 5 cm × 5 cm glass substrates to form sample A and on 5 cm × 5 cm glass substrates that were coated with an ITO film (ITO thickness ≈ 120 nm, ITO resistance ≈ 15 Ω/□) to form sample B; a DC magnetron sputtering system with a power density of 3 kW was used. Next, sample A with the Al/glass structure were anodized using various parameters—0.1–0.6 M H<sub>3</sub>PO<sub>4</sub>, 5–35°C and 20–60 V; sample B with the Al/ITO/glass structure were anodized in 0.3 M H<sub>3</sub>PO<sub>4</sub> at 3°C at 20–120 V. A porous alumina structure was then formed on the glass substrate. Following anodic oxidation, samples A and B were immersed in a 6 wt% H<sub>3</sub>PO<sub>4</sub> solution at 30°C with lower anodic oxidation voltages (20–60 V); sample B were immersed in a 6 wt% H<sub>3</sub>PO<sub>4</sub> solution at 45°C with higher anodic oxidation voltages (80–120 V). Etching with H<sub>3</sub>PO<sub>4</sub> enlarged the pores and removed the barrier layer. After the pores had been widened, samples A and B were annealed in the ambient atmosphere at 520°C for 9 min to make the residual Al to convert them to alumina.

### 3. Results and Discussion

#### 3.1. Fabricating AAO under Various Anodization Conditions

**3.1.1. Concentration of Electrolyte.** The rate of pore growth is generally related to the concentration of hydrogen ions. The reaction rate increases linearly with concentration, accelerating the dissolution of the alumina film, slowing its growth rate, and reducing its hardness. According to the experience, the barrier layer and porous oxide films are not conductive. Therefore, the volume of pores becomes a higher proportion; the equivalent resistance decreases. Sample A with the Al/glass structure were anodized at 25°C at 30 V. Figure 3 presents the SEM morphologies of AAO films at

0.1–0.6 M H<sub>3</sub>PO<sub>4</sub> following pore-widening treatment. The diameter of the pores slightly increased with the concentration, as shown in Figure 4; regularity of the shape of the pores also increased. In Figure 4, the pore diameter increases with the concentration of the solution from 0.1 to 0.4 M; the anodic reaction is suspected to have become saturated at a concentration of 0.4 M, before the concentration reached its final value of 0.6 M. The pore diameter that was obtained at 0.5 M is suspected to be the deviation from measurement or inaccurate sample.

**3.1.2. Reaction Temperature.** The effect of reaction temperature is similar to the concentration of electrolyte in the anodic oxidation for growing alumina films. Therefore, when the Al is anodized, the temperature of the electrolyte must be strictly controlled; a low-temperature circulatory system is generally used to keep the temperature of the electrolyte at a fixed value, ensuring that the obtained alumina films have high quality. Under constant current conditions, the thickness of the oxide layer is proportional to the charge accumulation. The formation of oxide thickness should maintain identically, but the higher operating temperature increases the erosive rate of the alumina by the acid solution. Therefore, the pores in the alumina become large, so the equivalent resistance is reduced. Figure 5 shows the SEM top-view morphology of AAO films that were anodized using 0.3 M H<sub>3</sub>PO<sub>4</sub> at 30 V at 5–35°C and then underwent pore-widening treatment. The diameter of the pores in the AAO films did not increase significantly with the reaction temperature, as shown in Figure 6. However, the reaction rate increased with the reaction temperature, because if the current density is too high, then thermal effect increases the temperature of the electrolyte, accelerating the dissolution of the alumina films.

**3.1.3. Applied Voltage.** The anodizing voltage is varied to yield pores with various diameters in the AAO template. Sample B with the Al/ITO/glass structure were anodized using 0.3 M H<sub>3</sub>PO<sub>4</sub> at 3°C. After the pore-widening treatment at 80–120 V, the SEM morphologies of the AAO films were obtained, as shown in Figure 7. The average pore diameter increased from 155 nm to 225 nm as the bias voltage increased from 80 V to 120 V, as plotted in Figure 8. The bias voltage significantly affected the diameter and regularity of the shape of the pores in the AAO films. Therefore, nanopore size increased with operating voltage, and pore diameter was linearly proportional to the applied voltage.

#### 3.2. Analysis of Optical Properties

**3.2.1. AAO/Glass Structure.** In fact, the anodic oxidation reaction proceeded strongly at the interface between acid solution and Al film resulting in the beginning of oxidation, and the newly formed porous alumina cut off the conductive path to the contact point, leaving a small amount of unreacted Al as isolated islands inside the sample [12]. The rate of conversion of Al to alumina is proportional to the bias voltage, so the amount of Al converted to alumina also increases with the bias voltage. However, once the anodic

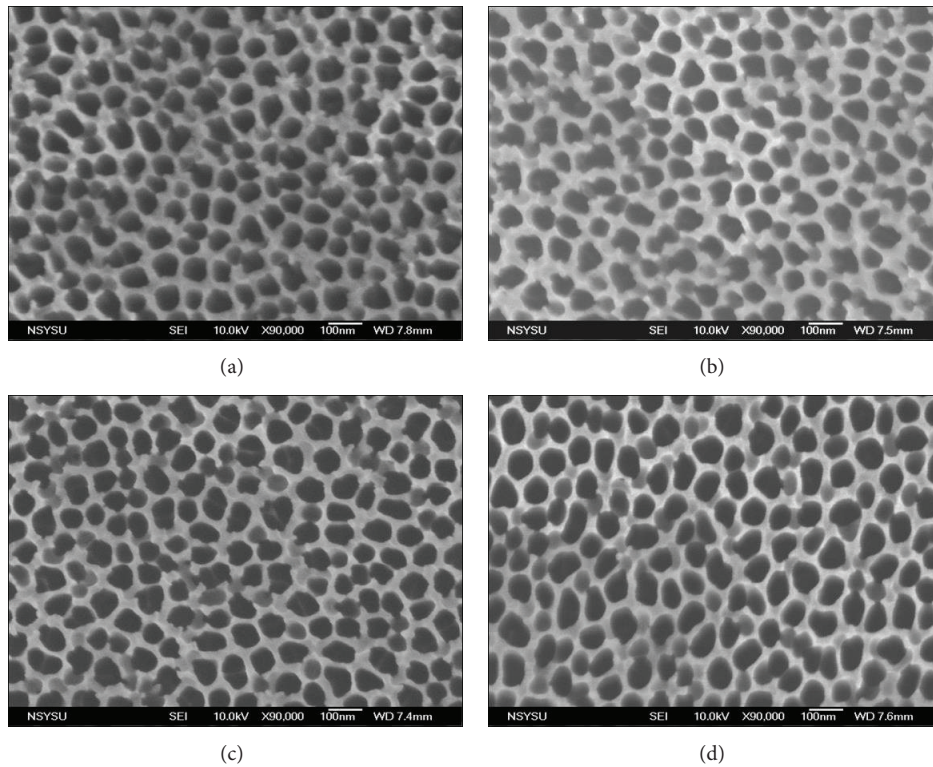


FIGURE 5: SEM micrographs of AAO films (sample A) at various reaction temperatures: (a) 5°C, (b) 15°C, (c) 25°C, and (d) 35°C. Following anodic oxidation, pore-widening treatment was performed in 6 wt%  $\text{H}_3\text{PO}_4$  at 30°C.

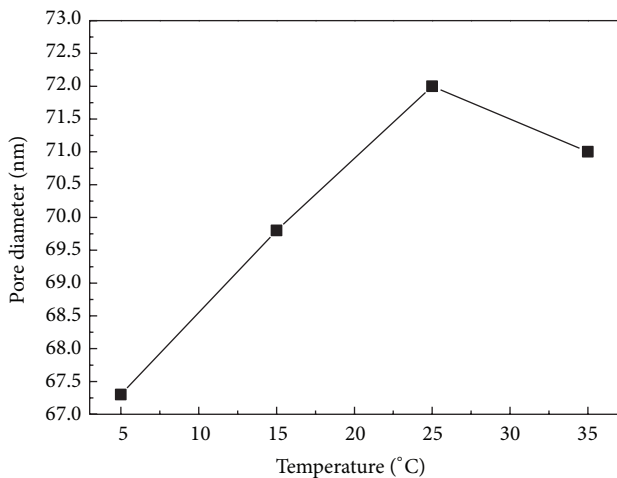


FIGURE 6: Diameter of pores in AAO/glass structures anodized at various reaction temperatures.

oxidation was stopped early, the quantity of unreacted Al increases. Hence, the average transmittance of AAO film decreases as the bias voltage increases.

The average transmittance of AAO/glass decreases from 93% to 72% as the bias voltage increases from 20 V to 60 V for wavelength from 450 nm to 1100 nm after posttreatment

annealing, as shown in Figure 9. The average transmittance of the AAO film at various bias voltages increased greatly because the unreacted Al is converted to alumina by the posttreatment annealing [13]. Despite the fact that the transmittance of AAO is increased by the posttreatment annealing, not all of the residual Al can be converted to alumina. The average transmittance of the AAO film at 60 V is less than 75% at a wavelength of 550 nm. Therefore, the amount of unreacted Al is a problem when the AAO process is performed at a high bias voltage.

**3.2.2. AAO/ITO/Glass Structure.** In Figure 10, the transmittance of the AAO films on the ITO conductive layers at various voltages from 20 V to 120 V after posttreatment annealing is compared with that of the as-grown ITO/glass structure. The average transmittance of the sample with the porous anodic structure at a wavelength of 550 nm exceeds 85% at bias voltages from 20 V to 120 V and exceeds that of the as-grown ITO/glass substrate, especially at wavelengths from 600 nm to 1100 nm, because adding the ITO conductive layer to the interface between the glass and the Al film increases the duration of conversion of Al to alumina. The decrease in the number of free electrons that are generated by intrinsic vacancies in the as-grown ITO film is argued to inhibit the absorption of free carriers by the ITO film, so that the transmittance of the ITO film with the AAO structure is more strongly enhanced than that of the as-grown ITO film without

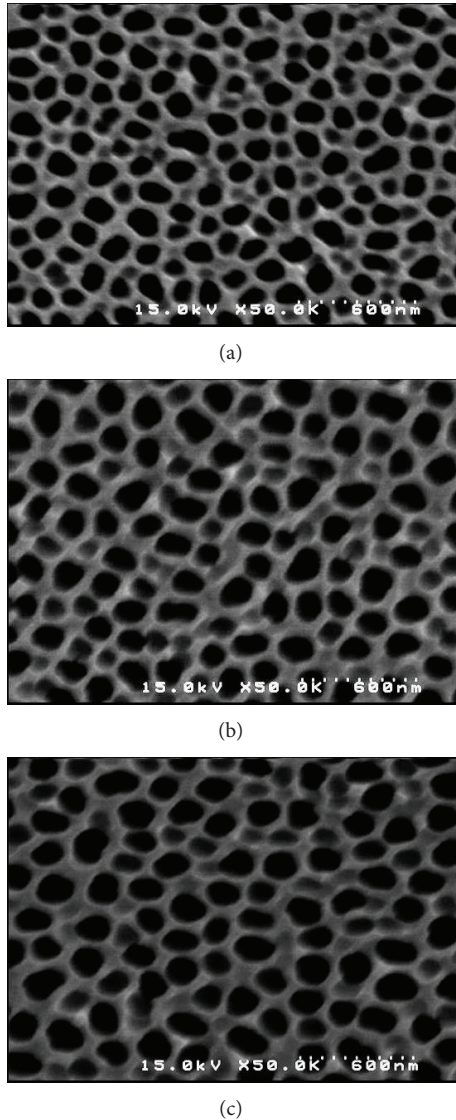


FIGURE 7: SEM micrographs of AAO films with ITO conductive layer (sample B) at various bias voltages: (a) 80 V, (b) 100 V, and (c) 120 V. After anodic oxidation, pore-widening treatment was performed in 6 wt%  $H_3PO_4$  at 45°C.

the AAO structure. Since the ITO conductive layer also reacts very strongly at the interface between the acid solution and Al film, the anodic oxidation stops quickly. Hence, the anodic oxidation reaction proceeds very strongly at high voltage, so the average transmittance decreases as bias voltage increases to 120 V at wavelengths from 600 nm to 1100 nm.

The above trend is similar to that of large scale (20 cm  $\times$  20 cm) AAO/ITO/glass structure [14]. Therefore, this periodic structure can serve as an optical trap in photovoltaic applications or enhance light extraction in light-emitting diodes as dielectric characteristics modulate the refractive index. Moreover, this AAO template can potentially be used for passivation in crystalline silicon solar cells owing to its native charges.

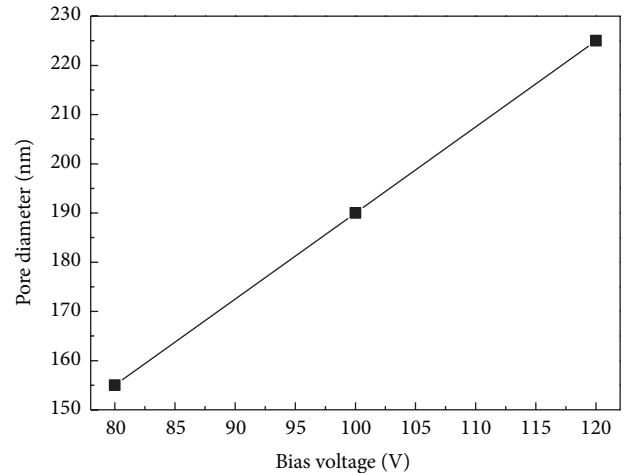


FIGURE 8: Diameter of pores in AAO/ITO/glass structure anodized at various bias voltages.

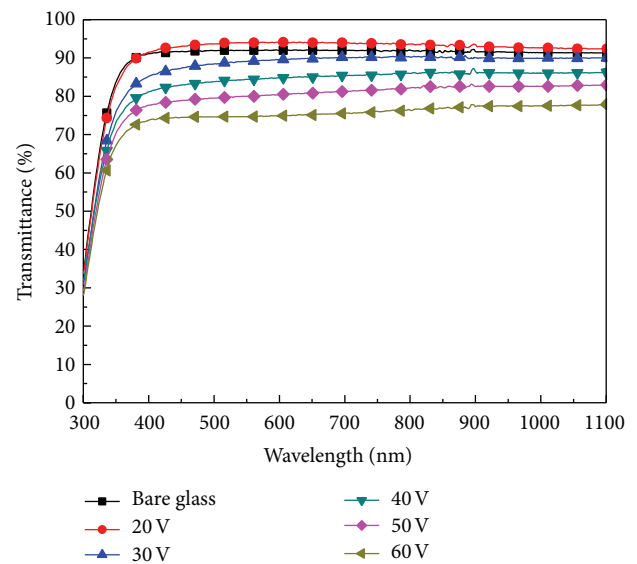


FIGURE 9: Optical transmittance of AAO/glass structure at bias voltages of 20 V, 30 V, 40 V, 50 V, and 60 V after posttreatment annealing.

#### 4. Conclusion

The study of porous anodic alumina on a 5 cm  $\times$  5 cm ITO/glass substrate was demonstrated. The AAO/ITO/glass structure was used to solve the problem of unreacted Al inside the AAO template, which reduces the average transmittance in the AAO/glass structure. The enhancement of transmittance was observed by varying the diameter of pores and applying various biases. Pore-widening treatment and posttreatment annealing enhanced the optical transmittance of the AAO/ITO/glass structure in the near-infrared range.

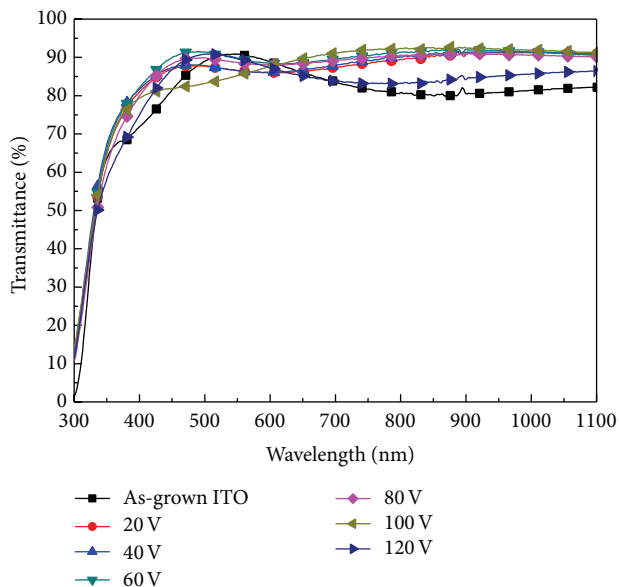


FIGURE 10: Optical transmittance of AAO/ITO/glass structure at bias voltages of 20 V, 40 V, 60 V, 80 V, 100 V, and 120 V after posttreatment annealing.

The results thus obtained indicate that the AAO/ITO/glass structure has great potential for use in optoelectronic devices.

### Conflict of Interests

The authors declare that they have no conflict of interests regarding the publication of this paper.

### Acknowledgments

The authors would like to thank NexPower Technology Corporation for helpful discussions. They would also like to thank Mr. Yu-Yao Chen, the Chief Technology Officer of E-HENG Technology Co., Ltd., for assistance using the technical sputtering machinery. This work was also supported by the National Science Council of Taiwan under Contract no. NSC 97-2221-E-006-239-MY2.

### References

- [1] C. R. Martin, "Membrane-based synthesis of nanomaterials," *Chemistry of Materials*, vol. 8, no. 8, pp. 1739–1746, 1996.
- [2] D. Routkevitch, A. A. Tager, J. Haruyama, D. Almawlawi, M. Moskovits, and J. M. Xu, "Nonlithographic nano-wire arrays: fabrication, physics, and device applications," *IEEE Transactions on Electron Devices*, vol. 43, no. 10, pp. 1646–1658, 1996.
- [3] X. Wang and G.-R. Han, "Fabrication and characterization of anodic aluminum oxide template," *Microelectronic Engineering*, vol. 66, no. 1–4, pp. 166–170, 2003.
- [4] S. Ono, M. Saito, M. Ishiguro, and H. Asoh, "Controlling factor of self-ordering of anodic porous alumina," *Journal of the Electrochemical Society*, vol. 151, no. 8, pp. 473–478, 2004.
- [5] G. D. Sulka and K. G. Parkola, "Temperature influence on well-ordered nanopore structures grown by anodization of aluminium in sulphuric acid," *Electrochimica Acta*, vol. 52, no. 5, pp. 1880–1888, 2007.
- [6] A. L. Friedman, D. Brittain, and L. Menon, "Roles of pH and acid type in the anodic growth of porous alumina," *Journal of Chemical Physics*, vol. 127, no. 15, Article ID 154717, 2007.
- [7] J. S. King, C. W. Neff, C. J. Summers et al., "High-filling-fraction inverted ZnS opals fabricated by atomic layer deposition," *Applied Physics Letters*, vol. 83, no. 13, pp. 2566–2568, 2003.
- [8] N. W. Liu, A. Datta, C. Y. Liu, and Y. L. Wang, "High-speed focused-ion-beam patterning for guiding the growth of anodic alumina nanochannel arrays," *Applied Physics Letters*, vol. 82, no. 8, pp. 1281–1283, 2003.
- [9] O. Kluth, B. Rech, L. Houben et al., "Texture etched ZnO:Al coated glass substrates for silicon based thin film solar cells," *Thin Solid Films*, vol. 351, no. 1-2, pp. 247–253, 1999.
- [10] Z. Fang, Y. Wang, X. Peng, X. Liu, and C. Zhen, "Structural and optical properties of ZnO films grown on the AAO templates," *Materials Letters*, vol. 57, no. 26-27, pp. 4187–4190, 2003.
- [11] S. Z. Chu, K. Wada, S. Inoue, and S. Todoroki, "Formation and microstructures of anodic alumina films from aluminum sputtered on glass substrate," *Journal of the Electrochemical Society*, vol. 149, no. 7, pp. B321–B327, 2002.
- [12] K. Nielsch, J. Choi, K. Schwirn, R. B. Wehrspohn, and U. Gösele, "Self-ordering regimes of porous alumina: the 10% porosity rule," *Nano Letters*, vol. 2, no. 7, 2002.
- [13] C.-W. Wu, *The effect of light current on amorphous thin film solar cell by the AAO/AZO front contact [M.S. thesis]*, National Cheng Kung University, 2010.
- [14] K.-W. Lee, T.-H. Yang, W.-L. Lu, and M.-P. Houn, "Fabricating 20 cm × 20 cm porous template using anodic aluminum oxide," *Integrated Ferroelectrics*, vol. 143, no. 1, pp. 47–57, 2013.

## Research Article

# Nanographene-Based Saturable Absorbers for Ultrafast Fiber Lasers

**Hsin-Hui Kuo and Shuo-Fu Hong**

*Department of Electrical Engineering, National University of Kaohsiung, Kaohsiung 81148, Taiwan*

Correspondence should be addressed to Hsin-Hui Kuo; [hhkuo@nuk.edu.tw](mailto:hhkuo@nuk.edu.tw)

Received 10 February 2014; Accepted 16 February 2014; Published 20 March 2014

Academic Editor: Chien-Jung Huang

Copyright © 2014 H.-H. Kuo and S.-F. Hong. This is an open access article distributed under the Creative Commons Attribution License, which permits unrestricted use, distribution, and reproduction in any medium, provided the original work is properly cited.

The generation of femtosecond pulse laser in the erbium-doped fiber laser system is presented by integrating of the nanographene-based saturable absorbers (SAs). A simplified method of dispersed nanographene-based SAs side-polished fiber device with controllable polished length and depth was also developed. The dependence of geometry of a graphene-deposited side-polished fiber device on optical nonlinear characteristics and on the performance of the MLFL was screened. We found that the 10 mm polished length with 1.68 dB insertion loss had the highest modulation depth (MD) of 1.2%. A stable MLFL with graphene-based SAs employing the optimized side-polished fiber device showed a pulse width, a 3 dB bandwidth, a time-bandwidth product (TBP), a repetition rate, and pulse energy of 523 fs, 5.4 nm, 0.347, 16.7 MHz, and 0.18 nJ, respectively, at fundamental soliton-like operation. The femtosecond pulse laser is achieved by evanescent field coupling through graphene-deposited side-polished fiber devices in the laser cavity. This study demonstrates that the polished depth is the key fabrication geometric parameter affecting the overall optical performance and better results exist within the certain polished range.

## 1. Introduction

Ultrafast lasers are interesting to researchers in diverse fields including ultrafast spectroscopy, optical coherence tomography, frequency comb generation, and material processing [1, 2]. Mode locking is one of the techniques generating optical pulses from picosecond to femtosecond regime and a nonlinear optical element is used for producing side-band coupling to transform a continuous-wave laser into a train of optical ultrashort pulses [3–5]. The main features of a nonlinear element characterize broadband nonlinear loss modulation with fast response time and easy integration into the laser system. In passive mode locking, a semiconductor saturable absorber mirror (SESAM) was widely used [6]. However, a SESAM usually has drawbacks of cost-ineffective and time-consuming fabrication process. Recent studies have indicated that nanomaterials such as single-wall carbon nanotube (SWCNT) and graphene can be alternative media for a SA [7, 8]. The nonlinear optical applications of CNT and graphene are well documented [9]. The first passively mode-locked fiber laser (MLFL) based on

SWCNT-SA was reported in 2003 [10]. However, in spite of the high nonlinearity of CNTs, they still have some inherent difficulties including aggregation, difficult alignment, and variable diameters for energy band gap design. Recently, it was reported that graphene has significant advantages with an ultrafast relaxation time and a wide spectral operation range due to its zero-gap linear band structure [11, 12]. Graphene-based SAs were recently reported for passively mode-locked lasers [13, 14] in the generation of femtosecond-scaled pulses [15, 16]. The interaction between SAs and the signal light can be directional transmission or evanescent field coupling [9]. To avoid the thermal damage induced by the optical power, the evanescent field interaction is adopted through a side-polished fiber or tapered fiber devices [17–19]. In addition, nonlinear effect can be controlled through the interaction length adjustment and the polished depth. The whole optical system is an all-fiber configuration.

In this study, the optical properties of mica-dispersed graphene-deposited side-polished fiber devices and the performance of a MLFL output are demonstrated. We report the effects of different polished lengths and polished depths

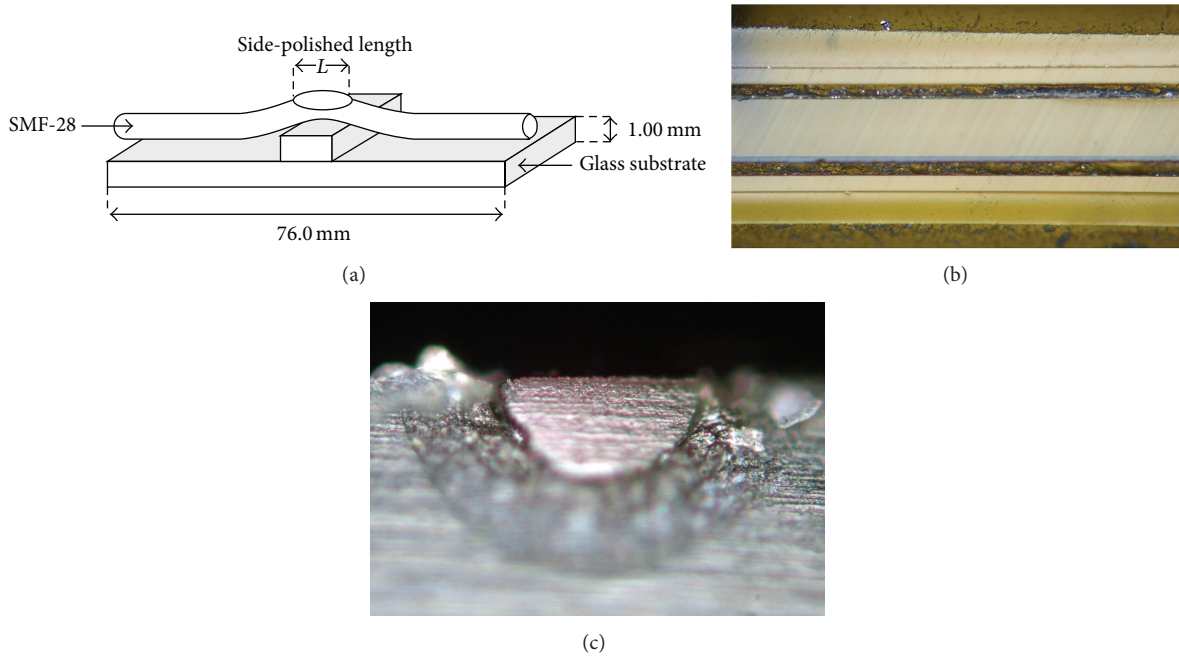


FIGURE 1: The fabrication of a side-polished fiber device. (a) The setup of the mounting, (b) the microscope image of the polished surface, and (c) the microscope image of the cross section of a side-polished fiber.

on the optical nonlinearities and on the MLFL outputs. It was found that the 10 mm polished length with 1.68 dB loss had the highest modulation depth (MD) of 1.2% in our experiments. A stable MLFL with graphene-based SAs employing the optimized side-polished fiber device showed a pulse width of 523 fs, a 3 dB bandwidth of 5.4 nm, and a time-bandwidth product of 0.347. This study of the graphene-deposited side-polished fiber device with controllable polished length and depth could provide an effective approach for the femtosecond pulse generation in the fiber laser and the polished depth of a side-polished fiber device has the stronger effect on the optical nonlinearities and the laser performance.

## 2. Experimental Details

The nanographene-deposited side-polished fiber device functions with the evanescent field interaction between the graphene-based SAs and the propagating light. We designed an easy method to make a side-polished fiber and the polished length and depth can be well controlled. A side-polished fiber was prepared by mounting a SMF28 with some curvature on stacked glass-substrates as shown in Figure 1(a). The polished length was adjusted by the length  $L$  of the top glass. The fiber together with the substrates was polished by the polisher (ULTRATEC YM-380WP) with four different grain-size diamond films of 9, 6, 1, and 0.1  $\mu\text{m}$  in sequence to ensure the noncracked and smoothly polished surface as shown in Figure 1(b). Figure 1(c) shows the cross section of the side-polished fiber. During the polishing process, the insertion loss (IL) was continuously monitored and IL indicates the polished depth  $D$ , the distance from the outer cladding to the polished surface. The losses of 1~3 dB in air were fabricated. To verify the correlation between the

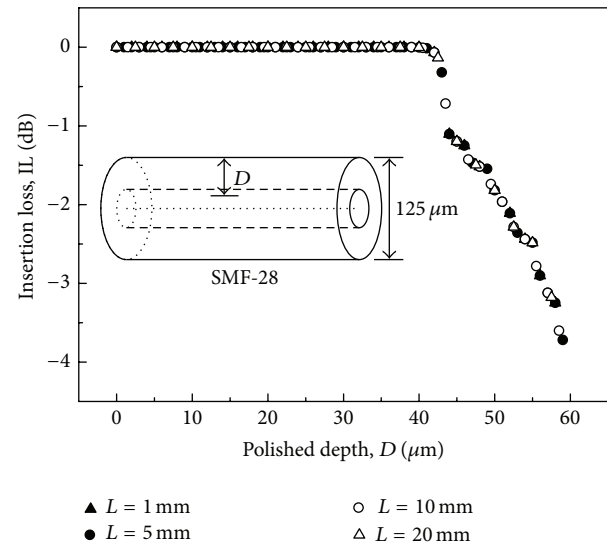


FIGURE 2: The simulated result of insertion loss IL versus the polished depth  $D$  with the polished length  $L = 1, 5, 10,$  and  $20$  mm.

polished geometry and the insertion loss (i.e.,  $IL = IL(L, D)$ ), the simulated result is shown in Figure 2. It shows that the dominating fabrication parameter is the polished depths rather than the lengths. In the following experiments we chose the polished lengths  $L$  of 5 mm and 10 mm for comparison.

A process for making the nanographene-based SAs was also developed. Graphitic plates with average thickness of 12 nm, lateral dimension of 4.5  $\mu\text{m}$ , and specific surface

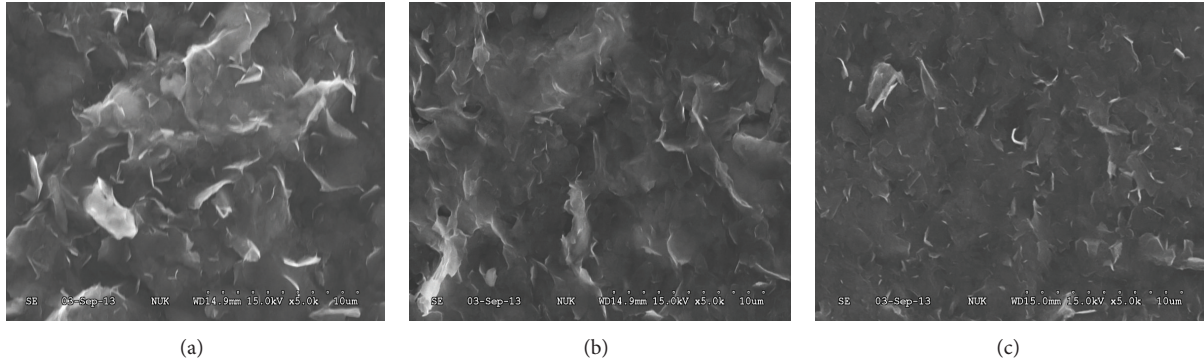


FIGURE 3: The SEM images of the mica-dispersed graphene-based SAs for different concentrations of (a) 1 wt%, (b) 2 wt%, and (c) 3 wt%.

area of  $80 \text{ m}^2/\text{g}$  were supplied by UP Co. (USA). Since the pristine graphitic plates tend to self-aggregate, it is difficult for solvating in water or organic solvents. The self-aggregation and plate-to-plate stacking are mainly caused by van der Waals force attraction. The selected layered silicate clays, the fluorinated mica (mica), were used as the dispersant to deaggregate graphene [20]. The procedures of mixing graphene and mica in water rendered the fine dispersion owing to the mutual interactions in their primary units. In [21], it was found that graphene can be well dispersed by the presence of mica and the physical mixture became readily dispersible in water. Graphenes of 0.1, 0.2, and 0.3 g with mica of 0.3, 0.6, and 0.9 g were ground adequately in an agate mortar and pestle, respectively. The mixture was then dispersed in 10 g of deionized water and agitated by ultrasonic treatment operated on a BRANSON 5510R-DTH in a water bath for 2 hours. The precursor solution of homogenous mica-graphene dispersion was obtained. By using a simple solution-drop process, the graphene-based nanocomposite film was made after being dried thoroughly at ambient temperature. The concentrations of our graphene-based SA film were 1, 2, and 3 wt% representing the weight ratios of graphene to deionized water. Figure 3 shows the SEM images of the mica-dispersed graphene-based SAs for three different concentrations. We found that the sample of 3 wt% gave the better surface uniformity and it was used for the following experiments.

### 3. Results and Discussion

**3.1. Optical Properties.** The linear absorption spectrum of 3 wt% mica-dispersed graphene-based SA films examined by a UV-VIS-NIR spectrophotometer is shown in Figure 4. The trace shows the smooth absorption feature from 400 to 2000 nm due to its zero-gap linear band structure, as theoretically expected [11, 12]. It is different from the carbon nanotube that has specific absorption peaks originated from the energy band gap.

The optical nonlinearity of graphene-based SAs can be characterized by the intensity-dependent absorption coefficient as  $\alpha(I, \lambda) = \alpha_0(\lambda)/(1 + I/I_s) + \alpha_{ns}$ , where  $\alpha_0$  is the linear absorption coefficient,  $I_s$  is the saturation intensity of the graphene-based SAs, and  $\alpha_{ns}$  is the nonsaturable

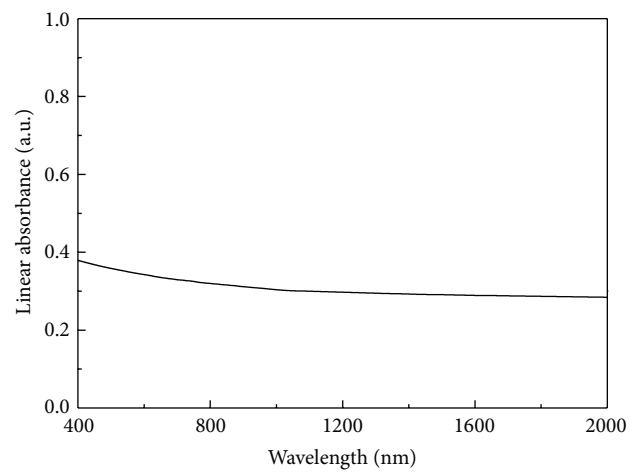


FIGURE 4: The linear absorption spectrum of 3 wt% mica-dispersed graphene-based SA films.

loss contributed from scattering of mica and graphene. The nonlinear transmission characteristics of graphene-deposited side-polished fiber devices were measured using a pulse laser that operated at the central wavelength of 1554.97 nm with a repetition rate of 25.1 MHz and pulse duration of 383 fs. The measurement setup is depicted in Figure 5. The tested samples of insertion losses of 1~3 dB for both polished lengths of 5 mm and 10 mm were measured. The modulation depth (MD) is related to the coupling strength between the graphene-based SAs and the optical pulse. Therefore, MD depends on the polished depth. Figure 6 shows the dependence of MD on the polished depths and the highest MD occurred around 1.5 dB for both polished lengths. The MDs of IL = 1.5 dB,  $L = 5 \text{ mm}$  and IL = 1.68 dB,  $L = 10 \text{ mm}$  were 0.8% and 1.2%, respectively. The nonlinear transmissions of these two samples are shown in Figure 7. Although the sample of the IL = 1.68 dB,  $L = 10 \text{ mm}$  had the slightly higher MD, it had larger linear nonsaturable losses of 65%. The results showed that the higher MD only existed within certain polished depth region and MD dropped rapidly when polished more deeply. It might be because of the asymmetry of the mode field profile and severe scattering losses. Another observation of a side-polished fiber device was sensitive to the optical pulse's state

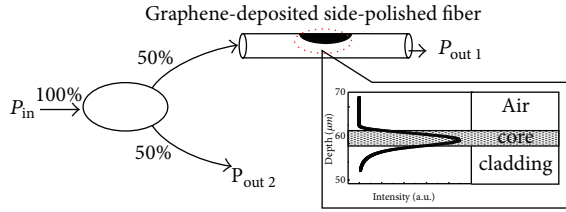


FIGURE 5: The setup of the nonlinear transmission measurement.

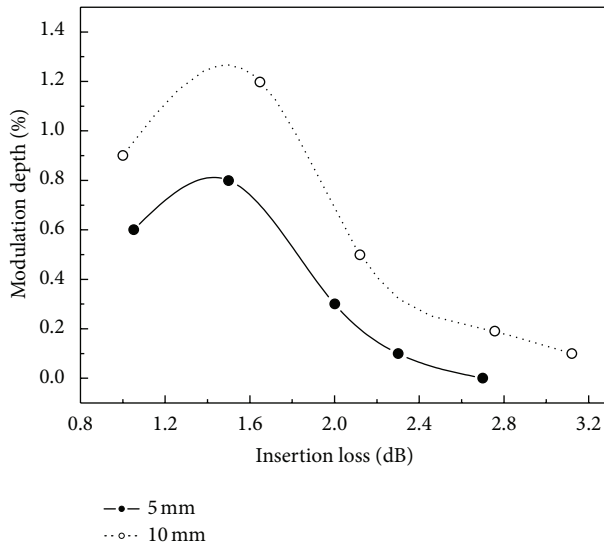


FIGURE 6: The modulation depths versus the insertion losses.

of polarization (SOP). The polarization dependent loss (PDL) of a side-polished fiber was measured about 0.6 dB and it was enhanced to  $\sim 7.1$  dB with the dispersed-graphene deposition.

**3.2. Laser Performance.** Figure 8 depicts our all-fiber passively mode-locked ring laser system incorporating a mica-dispersed graphene-deposited side-polished fiber device. An 85 cm long erbium-doped fiber (EDF) was used as a gain medium. It was pumped by a 980 nm laser diode via a wavelength division multiplexer (WDM). An isolator ensured the unidirectional operation. A polarization controller (PC) in this setup was a key element since our designed side-polished fiber device is sensitive to the state of polarization of the optical pulse. It was utilized to optimize mode locking. Total cavity length was 11.7 m. The 30% of the intracavity power was tapped out by an output coupler, connecting to a power meter, an autocorrelator, an oscilloscope, and an optical spectrum analyzer to observe the power, the temporal pulse trace, the pulse train, and the optical spectrum, respectively. The remaining 70% of the optical power was fed back into the system. To clarify the source of mode locking, we verified and excluded the contribution from nonlinear polarization rotation (NPR) [22] and confirmed that the MLFL output of our cavity configuration was mainly contributed from the graphene-based SAs.

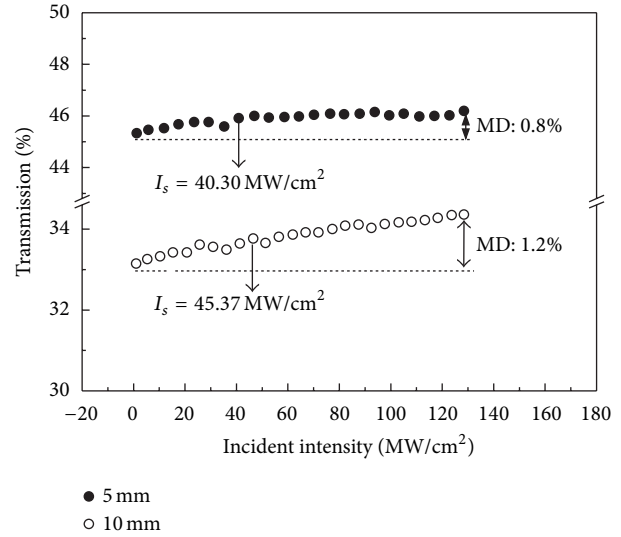


FIGURE 7: The nonlinear transmissions of tested samples of IL = 1.5 dB,  $L = 5$  mm and IL = 1.68 dB,  $L = 10$  mm.

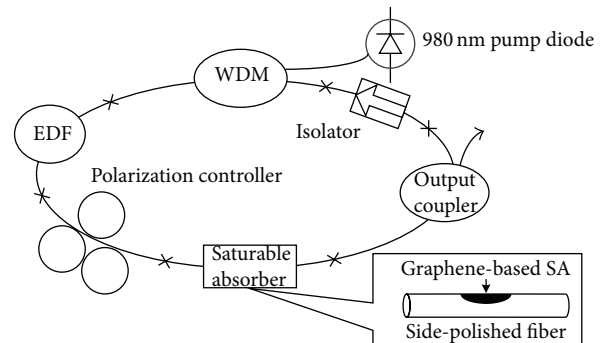


FIGURE 8: The configuration of our all-fiber passively mode-locked ring laser system.

All of the prepared samples have been tested and used as saturable absorbers for laser mode locking. We found that not all of them could be used as effective mode-locked SA elements. For those MDs which were smaller than 0.6% the nonlinear modulation was too weak to maintain laser mode locking. The better performance of a MLFL corresponded to the larger MD of 0.8~1.2% in our laser system. Figure 9 shows the dependence of 3 dB bandwidth on the polished depths which is indicated by the insertion loss. The optimized optical spectrum and the temporal pulse trace of IL = 1.5 dB,  $L = 5$  mm and IL = 1.68 dB,  $L = 10$  mm are shown in Figure 10. Both pulse trains observed from the oscilloscope had the repetition rate of 16.7 MHz. A transform-limited pulse of  $\text{sech}^2$  is assumed to estimate the pulse width. The operated range of fundamental mode locking was very wide starting from 100 to 360 mA and the 3 dB bandwidth increased with the larger pumping current. The comparison of the passively MLFL optimized performance of two polished lengths is shown in Table 1. The sample of 10 mm polished length exhibited slightly shorter pulse width. It was also found that the different order of harmonic mode locking could be

TABLE I: Laser performance of graphene-deposited side-polished fibers.

Polished length, $L$ (mm)	Insertion loss, IL (dB)	3 dB bandwidth (nm)	Pulse width (fs)	TBP	Pulse energy (nJ)
5	1.50	5.0	583	0.357	0.23
10	1.68	5.4	523	0.347	0.18

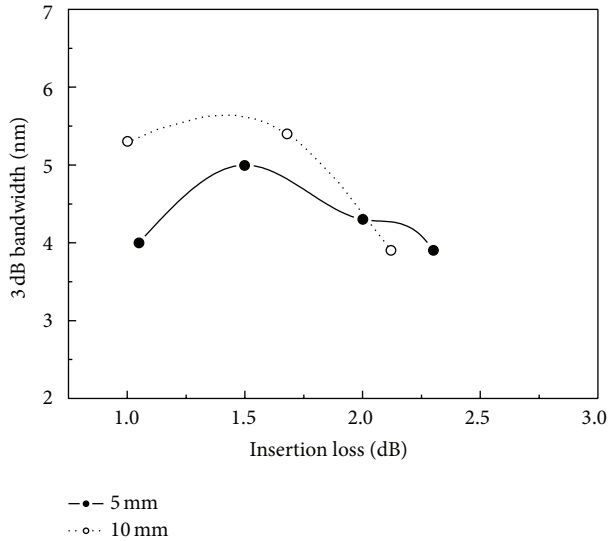
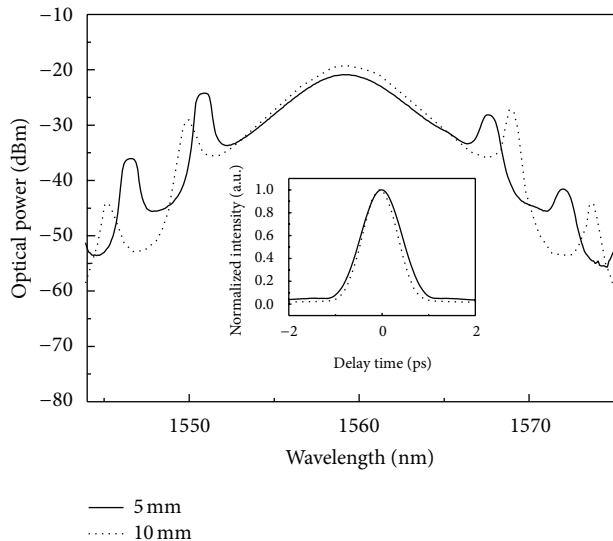


FIGURE 9: The 3 dB bandwidth versus the insertion losses.

FIGURE 10: The optimized optical spectrum and the temporal pulse trace for samples of IL = 1.5 dB,  $L$  = 5 mm and IL = 1.68 dB,  $L$  = 10 mm.

easily tuned by adjusting the polarization controller without changing the pumping power. The 16th harmonic mode locking was observed in our laser system.

#### 4. Conclusion

The optical nonlinear properties of mica-dispersed graphene-deposited side-polished fiber devices with the different

polished lengths and polished depths indicated by the insertion losses were investigated. The results were found that the higher MD only existed within certain polished depth region, and MD was slightly enhanced as the polished length increased. The insertion loss around 1.5 dB for both polished lengths showed the highest MD of 0.8% and 1.2%. A MLFL employing the nanographene-based SA side-polished fiber was presented. For that MD which was smaller than 0.6%, the nonlinear modulation was too weak to maintain mode locking. The better stable performance of a MLFL corresponded to the larger MD of 0.8~1.2% in our laser system. A stable MLFL employing the IL = 1.68 dB,  $L$  = 10 mm side-polished fiber device had the optimized performance with a pulse width of 523 fs, a 3 dB bandwidth of 5.4 nm, a time-bandwidth product of 0.347, a repetition rate of 16.7 MHz, and pulse energy of 0.18 nJ. This study demonstrates that the femtosecond pulse could be easily achieved by evanescent field coupling through graphene-deposited side-polished fiber devices in the laser cavity. The polished depth is the key fabrication geometric parameter affecting the overall optical performance.

#### Conflict of Interests

The authors declare that there is no conflict of interests regarding the publication of this paper.

#### Acknowledgments

The authors would like to thank the National Science Council, Taiwan, for financially supporting this research under Contract NSC 101-2221-E-390-015. The authors also thank Professor Wood-Hi Cheng's Laboratory of National Sun Yat-Sen University for the support of the instrument use.

#### References

- [1] F. Dausinger, F. Lichtner, and H. Lubatschowski, *Femtosecond Technology for Technical and Medical Applications*, vol. 96 of *Topics in Applied Physics*, Springer, Berlin, Germany, 2004.
- [2] U. Keller, "Recent developments in compact ultrafast lasers," *Nature*, vol. 424, no. 6950, pp. 831–838, 2003.
- [3] E. G. Arthurs, D. J. Bradley, and A. G. Roddie, "Buildup of picosecond pulse generation in passively mode-locked rhodamine dye lasers," *Applied Physics Letters*, vol. 23, no. 2, pp. 88–89, 1973.
- [4] H. A. Haus, "Mode-locking of lasers," *IEEE Journal on Selected Topics in Quantum Electronics*, vol. 6, no. 6, pp. 1173–1185, 2000.
- [5] H. A. Haus, "Theory of mode locking with a fast saturable absorber," *Journal of Applied Physics*, vol. 46, no. 7, pp. 3049–3058, 1975.

- [6] M. E. Fermann, "Ultrafast fiber oscillators," in *Ultrafast Lasers: Technology and Applications*, Marcel Dekker, New York, NY, USA, 2003.
- [7] I. Hernandez-Romano, D. Mandridis, D. A. May-Arrijoa, J. J. Sanchez-Mondragon, and P. J. Delfyett, "Mode-locked fiber laser using an SU8/SWCNT saturable absorber," *Optics Letters*, vol. 36, no. 11, pp. 2122–2124, 2011.
- [8] T. Hasan, Z. Sun, F. Wang et al., "Nanotube—polymer composites for ultrafast photonics," *Advanced Materials*, vol. 21, no. 38–39, pp. 3874–3899, 2009.
- [9] S. Yamashita, "A tutorial on nonlinear photonic applications of carbon nanotube and graphene," *Journal of Lightwave Technology*, vol. 30, no. 4, pp. 427–447, 2012.
- [10] S. Y. Set, H. Yaguchi, Y. Tanaka, and M. Jablonski, "Laser mode locking using a saturable absorber incorporating carbon nanotubes," *Journal of Lightwave Technology*, vol. 22, no. 1, pp. 51–56, 2004.
- [11] A. K. Geim and K. S. Novoselov, "The rise of graphene," *Nature Materials*, vol. 6, no. 3, pp. 183–191, 2007.
- [12] F. Bonaccorso, Z. Sun, T. Hasan, and A. C. Ferrari, "Graphene photonics and optoelectronics," *Nature Photonics*, vol. 4, no. 9, pp. 611–622, 2010.
- [13] Q. Bao, H. Zhang, Y. Wang et al., "Atomic-layer craphene as a saturable absorber for ultrafast pulsed lasers," *Advanced Functional Materials*, vol. 19, no. 19, pp. 3077–3083, 2009.
- [14] Z. Sun, T. Hasan, F. Torrisi et al., "Graphene mode-locked ultrafast laser," *ACS Nano*, vol. 4, no. 2, pp. 803–810, 2010.
- [15] P. L. Huang, S.-C. Lin, C.-Y. Yeh et al., "Stable mode-locked fiber laser based on CVD fabricated graphene saturable absorber," *Optics Express*, vol. 20, no. 3, pp. 2460–2465, 2012.
- [16] P. L. Huang, H. H. Kuo, R. X. Dong et al., "Performance of graphene mediated saturable absorber on stable mode-locked fiber lasers employing different nano-dispersants," *Journal of Lightwave Technology*, vol. 30, no. 21, pp. 3413–3419, 2012.
- [17] Y.-W. Song, S. Yamashita, C. S. Goh, and S. Y. Set, "Carbon nanotube mode lockers with enhanced nonlinearity via evanescent field interaction in D-shaped fibers," *Optics Letters*, vol. 32, no. 2, pp. 148–150, 2007.
- [18] Y.-W. Song, S.-Y. Jang, W.-S. Han, and M.-K. Bae, "Graphene mode-lockers for fiber lasers functioned with evanescent field interaction," *Applied Physics Letters*, vol. 96, no. 5, Article ID 051122, 2010.
- [19] Y.-W. Song, K. Morimune, S. Y. Set, and S. Yamashita, "Polarization insensitive all-fiber mode-lockers functioned by carbon nanotubes deposited onto tapered fibers," *Applied Physics Letters*, vol. 90, no. 2, Article ID 021101, 2007.
- [20] Y.-F. Lan and J.-J. Lin, "Observation of carbon nanotube and clay micellelike microstructures with dual dispersion property," *The Journal of Physical Chemistry A*, vol. 113, no. 30, pp. 8654–8659, 2009.
- [21] H. H. Kuo, P. L. Huang, C. Y. Yeh, and W. H. Cheng, "Few-layer graphene-based saturable absorbers employing mica dispersant for stable mode-locked fiber lasers," *IEEE Photonics Technology Letters*, vol. 25, no. 7, pp. 633–636, 2013.
- [22] G. P. Agrawal, *Application of Nonlinear Fiber Optics*, Academic Press, New York, NY, USA, 2nd edition, 2008.

## Research Article

# Development of Amorphous/Microcrystalline Silicon Tandem Thin-Film Solar Modules with Low Output Voltage, High Energy Yield, Low Light-Induced Degradation, and High Damp-Heat Reliability

Chin-Yi Tsai<sup>1</sup> and Chin-Yao Tsai<sup>2</sup>

<sup>1</sup> Department of Applied Physics, National University of Kaohsiung, Kaohsiung 811, Taiwan

<sup>2</sup> Auria Solar, Da-Ye 1st Road 9, Sinshih, Tainan 74146, Taiwan

Correspondence should be addressed to Chin-Yi Tsai; [cytsai@nuk.edu.tw](mailto:cytsai@nuk.edu.tw)

Received 26 January 2014; Accepted 3 February 2014; Published 16 March 2014

Academic Editor: Chien-Jung Huang

Copyright © 2014 C.-Y. Tsai and C.-Y. Tsai. This is an open access article distributed under the Creative Commons Attribution License, which permits unrestricted use, distribution, and reproduction in any medium, provided the original work is properly cited.

In this work, tandem amorphous/microcrystalline silicon thin-film solar modules with low output voltage, high energy yield, low light-induced degradation, and high damp-heat reliability were successfully designed and developed. Several key technologies of passivation, transparent-conducting-oxide films, and cell and segment laser scribing were researched, developed, and introduced into the production line to enhance the performance of these low-voltage modules. A 900 kWp photovoltaic system with these low-voltage panels was installed and its performance ratio has been simulated and projected to be 92.1%, which is 20% more than the crystalline silicon and CdTe counterparts.

## 1. Introduction

Tandem amorphous/microcrystalline silicon (a-Si/ $\mu$ -Si) thin-film solar modules with low output voltage have gained many attentions recently, because the high output voltage (around 100 V) of regular modules will put a critical demand on the specifications of the associated balance of system (e.g., electrical connection cables) and it could not be compatible with the low output voltage (around 30 V) of the mainstream products of crystalline silicon wafer-based solar modules. As a result, it is expected that the cost of balance of systems associated with the low-voltage a-Si/ $\mu$ -Si thin-film solar modules could be lower than the regular high-voltage ones. In addition, low-voltage modules are more suitable for stand-alone applications, for example, the conventional 12 V battery charging for consumer electronics.

An amorphous/microcrystalline silicon solar panel is usually laser scribed into cells and the cells are series connected. In order to achieve the low output voltage, the panel needs to be additionally laser scribed into several

segments and the segments are then parallel connected. Conceptually, this segment laser scribing contributes only a few additional processes and the realization of the low-voltage modules should be rather straightforward. However, in reality, there exist several technical challenges, especially in the mass production line. For example, the additional laser scribing will not only inevitably decrease the effective illuminated area and thus increase the area of dead zones, but also create many material defects along the edge of the scribed lines. The defects resulted from laser scribing will provide channels for leakage current and thus decrease the shunt resistance of solar modules. Therefore, the first technical challenge in developing the low-voltage modules will be to minimize the detrimental effects resulted from the laser scribing processes. Furthermore, because of the connection arrangements of series-connected cells and parallel-connected segments, the module performance inevitably will suffer from the mismatching effects results from the different physical characteristics of individual cells and segments. Due to this mismatching effect, the output current will be

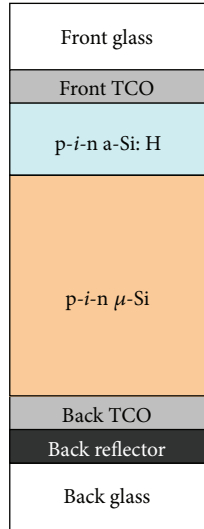


FIGURE 1: Schematic diagram of the structure of a tandem amorphous/microcrystalline silicon thin-film solar cell.

determined by and suffered from the cell with the lowest short-circuit current and the output voltage will be determined by and suffered from the segment with the lowest open-circuit voltage. The mismatching effects caused by the different physical characteristics of cells and segments are mostly resulted from the nonuniformity of thin films due to the spatial variation of manufacture processes on large-area substrates, especially, the transparent-conducting-oxide (TCO) films grown by the low-pressure chemical vapour deposition (LPCVD) processes in which the nonuniformity of the film thickness could be over 20%. How to improve the uniformity of manufacture processes and thus minimize the mismatching effects among cells and segments is another technical problem that needs to be resolved in order to develop the low-voltage solar modules. In the following, we will give a brief description on the developments of these key technologies and the performance of the low-voltage modules enabled by these technologies.

## 2. Technologies

In this work, the tandem amorphous/microcrystalline (also called as “micromorph”) silicon thin-film solar modules are produced from the 60 MW production line of Auria Solar [1–8]. The structure of a cell in a-Si/ $\mu$ -Si thin-film solar modules is schematically shown in Figure 1. In general, the thickness of the front and back glasses is about 3.2 mm, the back reflector 0.5 mm, the a-Si:H cell layer 300 nm, the  $\mu$ -Si cell layer 1400 nm, the back TCO 1500 nm, and the front TCO 1800 nm. The manufacture processes of these modules are briefly outlined in Figure 2 in which a front-glass substrate goes through the LPCVD TCO film growth, plasma-enhanced chemical vapor deposition (PECVD) a-Si:H and  $\mu$ -Si film growth, and 3-step laser scribing to form the basic structure of solar cells and then metal ribbon wiring, back-reflector screen printing, abrasive blasting edge

isolation, PV foil encapsulation, lamination, and junction-box adhesion to form a finished module. The size of a panel is 1.3 m  $\times$  1.1 m. A module is usually laser scribed into 99 cells and its output voltage is regularly about 100 V. To produce modules with lower output voltage, many technologies were researched, developed, and introduced into the production line. These technologies are required to ensure the efficiency of the low-voltage modules to be better than the regular ones. At the same time, the throughput and yield in every production process are demanded not to be compromised when introducing these technologies into the production line. These key technologies will be discussed in the following.

**2.1. Passivation.** A low-voltage panel needs to be laser scribed into several segments. These additional laser scribing lines function as edge isolations between two segments in a panel. The scribing line widths of segments are usually much larger than those of cells. As a result, segment laser scribing lines inevitably create many material defects along the edge of the scribed lines. The defects resulted from laser scribing will provide channels for leakage current and thus decrease the shunt resistance of modules. A passivation scheme for laser scribing lines, named as the moon technology, is designed and implemented to solve the problem of low shunt resistances resulted from laser scribing. The moon technology is denominated because the solar modules, after the treatment of this passivation technology, can effectively generate measurable power even at night under the feeble moon light. With the moon technology, the material defects resulted from laser scribing can be very effectively passivated and thus the shunt resistance can dramatically increase by one order of magnitude, for example, from original 2000  $\Omega$  to more than 20,000  $\Omega$ . This will increase the module stabilized efficiency by an amount of more than 5~10%. It has been investigated and reported that high shunt resistances will give monocrystalline silicon solar cells a much better low-light performance [9]. The similar conclusion can also be seen

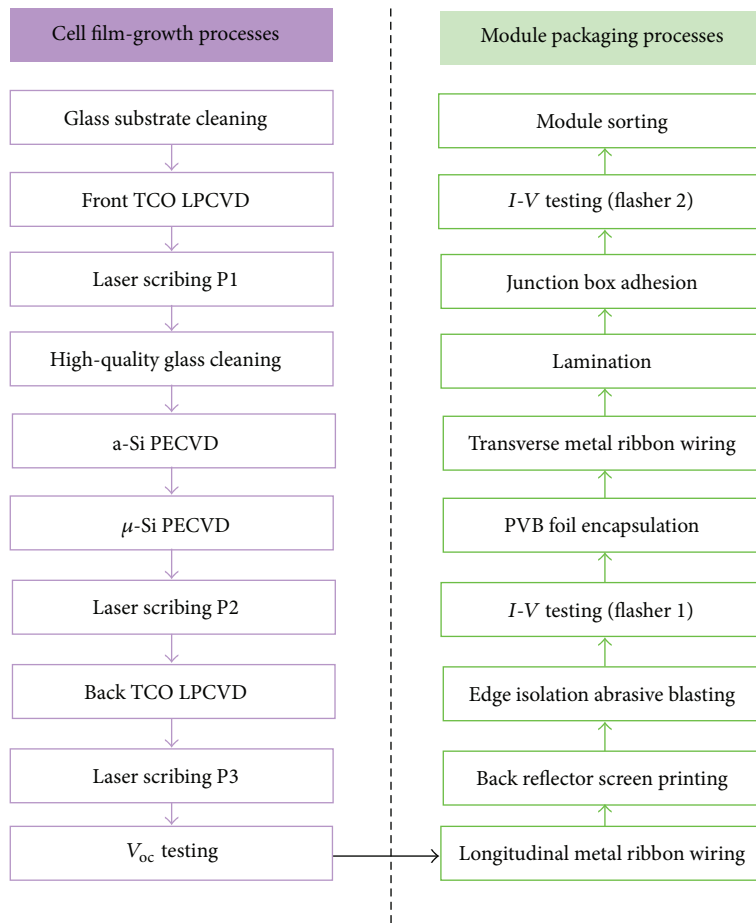


FIGURE 2: Schematic diagram of the flow of manufacture processes of tandem amorphous/microcrystalline silicon thin-film solar modules.

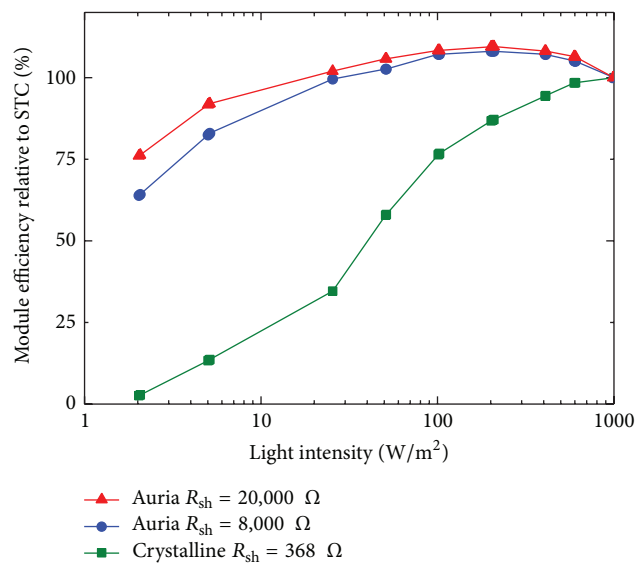


FIGURE 3: The module efficiency relative to standard testing condition (STC) as a function of the irradiance light intensity for two Auria thin-film and crystalline silicon modules with different shunt resistances ( $R_{sh}$ ).

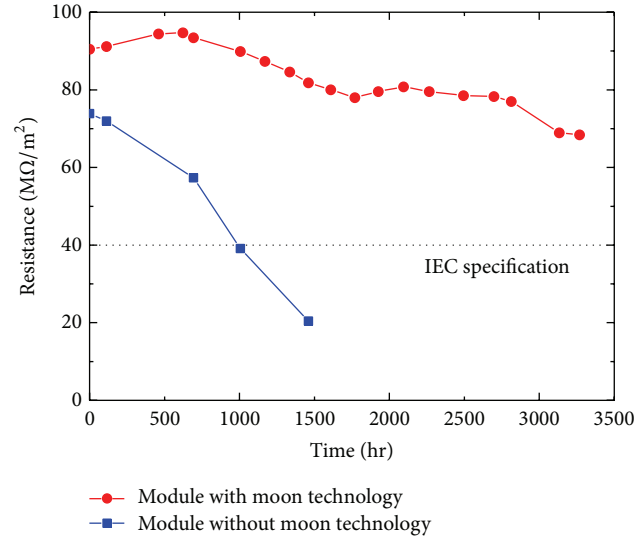


FIGURE 4: The resistance by module area as a function of the damp-heat testing time for modules with and without the moon technology passivation. Note that the dash line represents the minimum requirements of International Electrotechnical Commission (IEC) for the electric insulation in which the resistance should be larger than 40 MΩ per module area under the damp-heat testing condition.

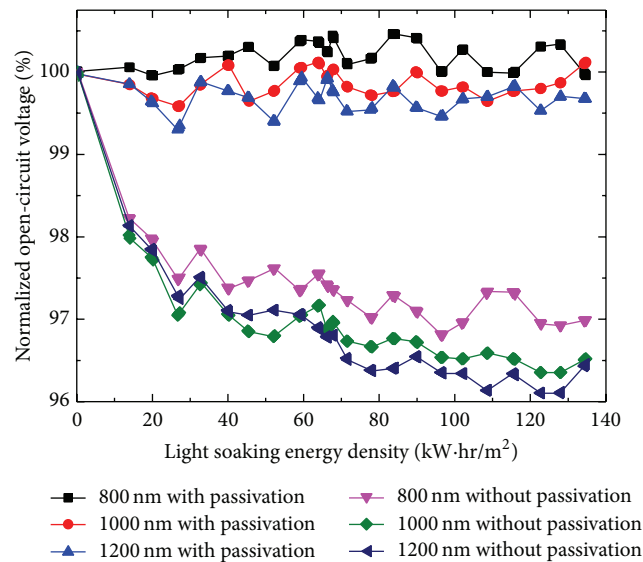


FIGURE 5: The open-circuit voltage ( $V_{oc}$ ) as a function of the light soaking energy density for solar modules with different  $i$ -layer thickness of 800, 1000 and 1200 nm, and also with and without the moon technology passivation, respectively.

from our thin-film silicon modules as shown in the results of Figure 3. The enhancement on the low-light performance will increase the energy yield of modules by an amount of 10~15%, according to our simulation. Furthermore, the material defects, such as microcracks, resulted from laser scribing not only provide channels for current leakage but also create permeative paths for water vapor to result in damp-heat degradation; therefore, technologies that can suppress the leakage current due to laser scribing will generally give modules a better performance under the damp-heat condition. The in-house damp-heat test (1000 hour 85°C

and 85% relative humidity) of our modules can even reach recorded over 3000 hours which is equivalent to 60 years damp-heat reliability, as shown in the results of Figure 4.

The passivation from moon technology not only minimizes the detrimental effects introduced by the laser scribing, but also surprisingly gives a beneficial effect of alleviating the light-induced degradation (LID) on silicon thin films. It has been observed that porous structures, such as cracks, exist in intrinsic  $\mu\text{c-Si}$  layers, which could lead to oxygen penetration and grain boundaries contamination and consequently cause the LID effects on fill factor and open-circuit

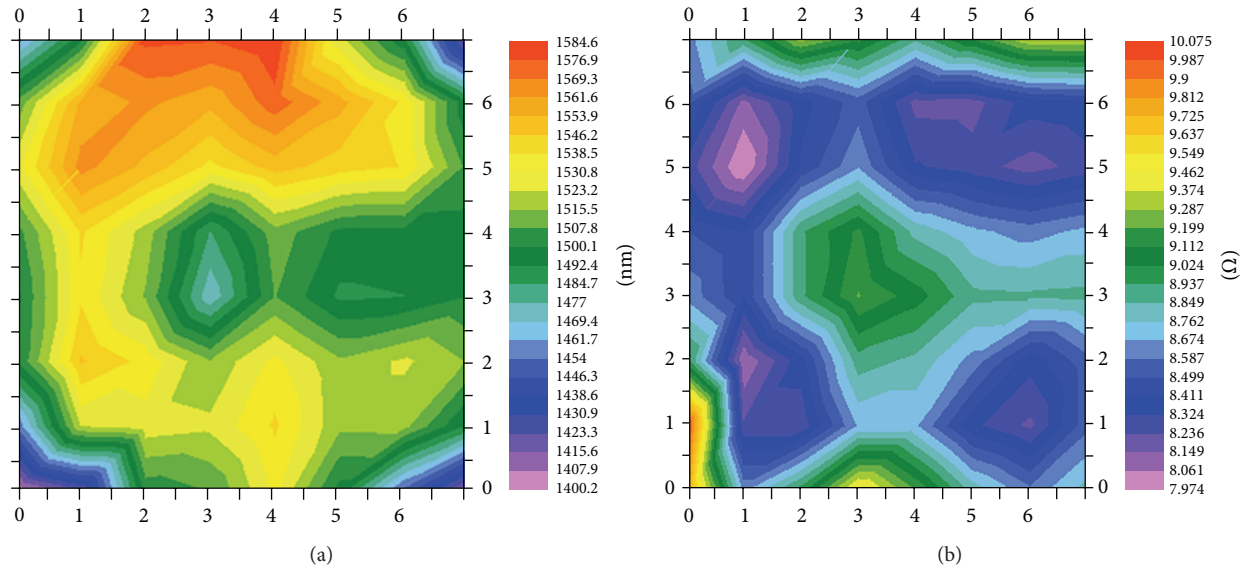


FIGURE 6: The (a) thickness and (b) resistance distributions of a TCO film represented by contour plot. The thickness and resistance uniformity is 2.8% and 11.64%, respectively. Note that the unit on the scale of the color chart is nm in (a) and  $\Omega$  in (b).

voltage of solar cells [10]. This fact has been verified by the light soaking experiments on the modules without the moon technology passivation, as shown in the results of Figure 5. On the contrary, for those modules with the moon technology passivation, the LID effects on the open-circuit voltage have been almost complete diminished. Therefore, it could be concluded that the moon technology passivation has successfully passivated the porous structures, such as cracks, in the intrinsic  $\mu\text{c-Si}$  layers and thus alleviated their LID effects.

**2.2. TCO Films.** In a low-voltage module, the panel is laser scribed into cells and then into segments. The cells within a segment are series connected, while the segments are parallel connected. Because of such a connection arrangement, the module performance inevitably will suffer from the mismatching effects results from the different physical characteristics of individual cells and segments. For example, due to the mismatching effect, the output current will be determined by and suffered from the cell with the lowest short-circuit current. Similarly, the output voltage will be determined by and suffered from the segment with the lowest open-circuit voltage. The mismatching effects caused by the different physical characteristics of cells and segments are mostly resulted from the nonuniformity of thin films due to the spatial variation of manufacture processes. Since the size of the solar panel in this work is  $1.3\text{ m} \times 1.1\text{ m}$ , the mismatching effects resulted from the nonuniformity of thin films will become a critical problem, especially for the LPCVD boron doped ZnO TCO films.

In order to increase the uniformity of TCO films, the manufacture process are carefully redesigned from its original turn-key solution and the manufacture condition needs to be precisely controlled. Especially, the spatial distributions of growth temperature, gas flow, and pressure need to be

constantly monitored and carefully controlled in order to ensure a better uniformity of the thickness and resistance of TCO films. Figure 6 shows the thickness and resistance spatial distributions of a TCO film. The thickness uniformity of TCO films in our production line can be as low as 2.8%, which was dramatically improved from the original 20% specification. At the same time, the resistance uniformity of TCO films can be as low as 11.64%, which is also significantly improved from the original 40% specification.

The surface morphology of TCO films needs to be carefully designed in order to optimize their light trapping function and minimize the interface defects between the TCO and Si films. For a TCO film of high haze, as shown in Figures 7(a) and 7(c), it has a larger and sharper grain morphology and thus a better light-trapping function, but it also creates more interface defects between the TCO and Si films. On the other hand, for a TCO film of low haze, as shown in Figures 7(b) and 7(d), it has a smaller and blunter grain morphology and thus a worse light-trapping function; nevertheless, it generates less interface defects between the TCO and Si films. The low-voltage solar modules in this work are designed with the optimal haze and thus have their maximum light-trapping function and minimum interface defects between the TCO and Si films.

**2.3. Laser Scribing.** In a low-voltage module, additional laser scribing lines are needed to form several segments in a panel. Usually, these segment-forming lines are much wider than the cell-forming lines in order to introduce good edge isolation between two segments; as a result, they will reduce the effective illuminated area of panels. In order to increase the effective illuminated area, the dead zone of laser scribing in our low-voltage module has been minimized to be as low as  $150\ \mu\text{m}$  (as shown in Figure 8), which is significantly improved from the original  $400\ \mu\text{m}$  specification. This result

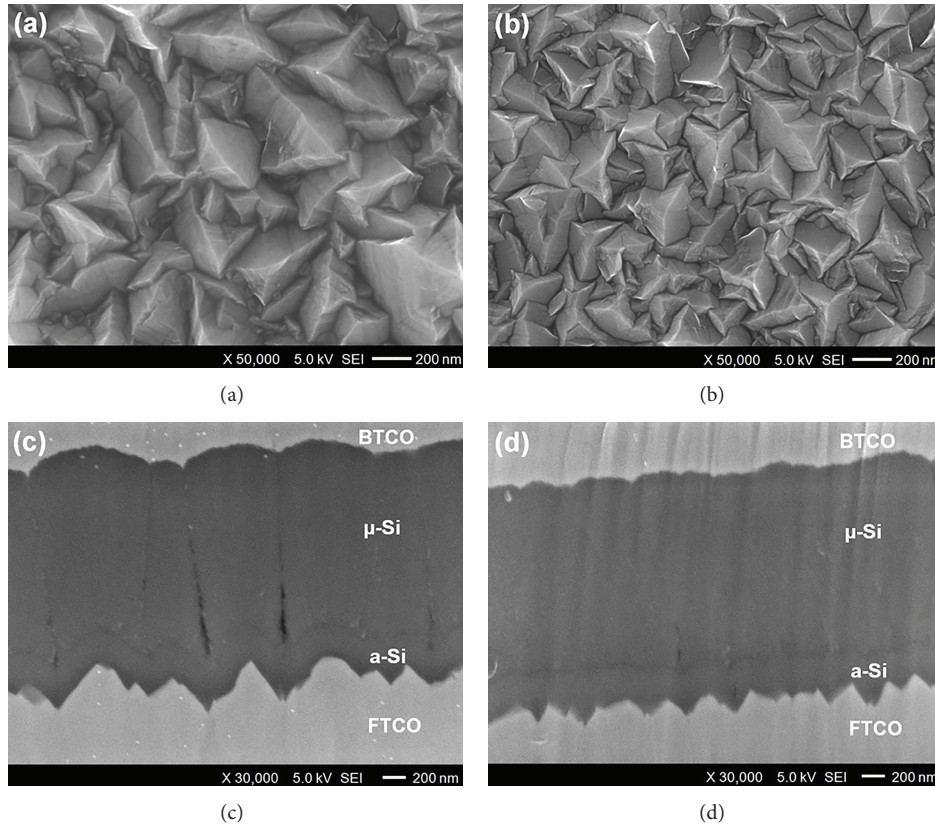


FIGURE 7: SEM top views of the front TCO in (a) a cell with high-haze TCO and (b) a cell with low-haze TCO. Their correspondent cross section views is given in (c) and (d), respectively.

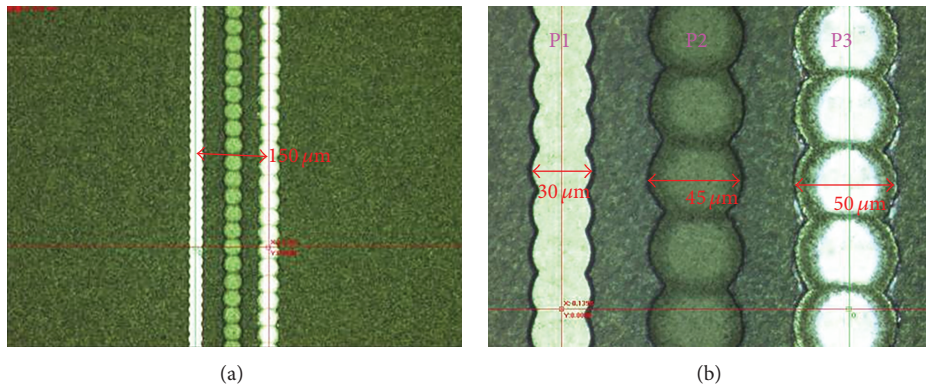


FIGURE 8: Three laser scribing lines, P1, P2, and P3, in a solar module. The dead zone is 150  $\mu\text{m}$ .

was achieved by several major tunings in the peak power, focus, and pulse duration of laser sources from its original turn-key specifications.

Although the nonuniformities of TCO films have been reduced to be as minimum as possible, their effects on the physical characteristics of solar modules, such as short-circuit current, could still be demonstrated in the results of Figure 9, in which a  $1.3 \times 1.1 \text{ m}^2$  solar module is divided into 33 regions and the normalized short-circuit current decreases from 100% at the edge to around 95% at the center. In other words, the TCO film nonuniformity causes a 5% mismatching

effect on the short-circuit current. Taking this fact into consideration, two types of low-voltage solar modules were designed and developed: one is laser scribed into 128 cells and 2 segments while the other 138 cells and 4 segments (as schematically shown in Figure 10). It should be noted that the original high-voltage solar module are laser scribed into 99 cells and without any segment. The increase in the number of cells in the low-voltage solar module is designed to optimize their performance and minimize the mismatching effects. The output voltage of the formal one is designed to be around 30 V (named as LV30 modules) which is roughly

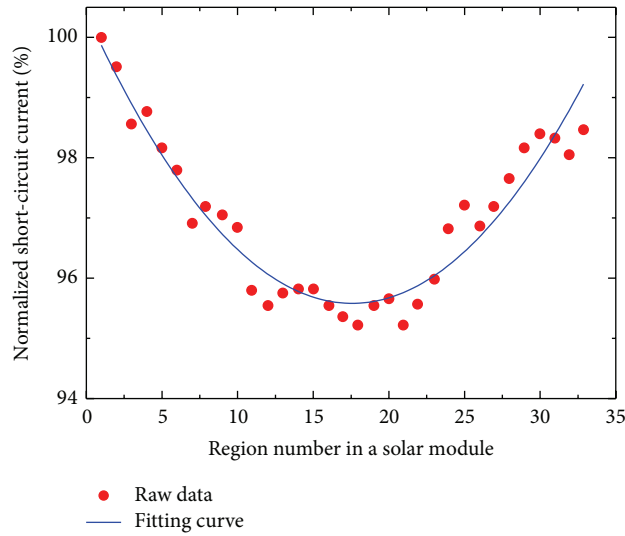


FIGURE 9: Normalized short-circuit current distribution in a  $1.3 \text{ m} \times 1.1 \text{ m}^2$  silicon thin-film solar modules divided into 33 regions.

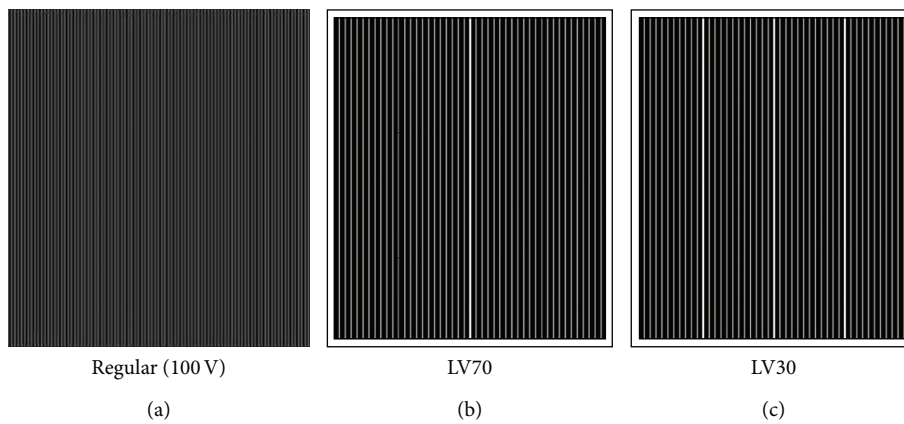


FIGURE 10: Schematic diagram of laser-scribed lines on (a) a regular module with 99 cells, (b) a 70 V low-voltage module (LV70) with 128 cells and 2 segments, and (c) a 30 V low-voltage module (LV30) with 138 cells and 4 segments.

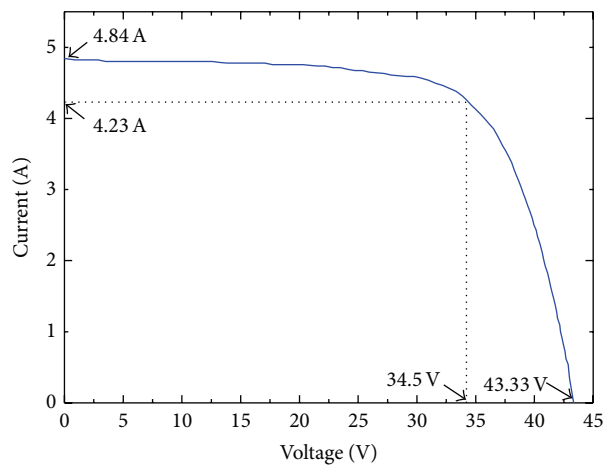


FIGURE 11: *I-V* curve of a 30 V low-voltage solar module (LV30) with open-circuit voltage 43.33 V, short-circuit current 4.843 A, maximum power voltage 34.5 V, and maximum power current 4.23 A. It should be noted that the *I-V* curve gives the initial maximum output power 145.94 W, while the stabilized maximum output power is 130.4 W after the light-induced degradation.

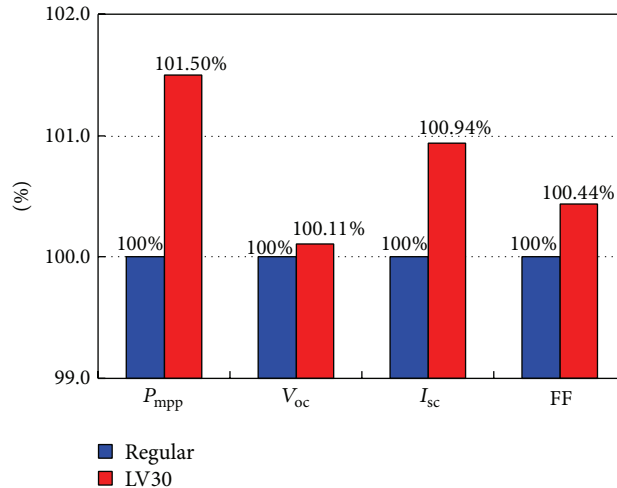


FIGURE 12: Comparison of maximum output power, open-circuit voltage, short-circuit current, and filled factor between a 30 V low-voltage silicon thin-film solar module (LV30) and a crystalline silicon wafer-based solar module.

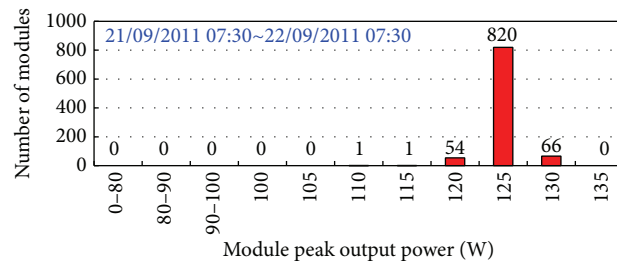


FIGURE 13: The distribution of power rating from a daily production record of LV30 modules in Auria Solar, where the produced modules are sorted according to their stabilized maximum output power.

correspondent to its counterpart of a typical crystalline silicon wafer-based solar module. On the other hand, the output voltage of the latter one is designed to be around 70 V (named as LV70 modules) which is approximately correspondent to its counterpart of a typical CdTe thin-film solar module. The performance of these low-voltage solar modules will be discussed in the following.

**2.4. Lamination.** In a low-voltage panel, metal ribbons are applied onto each individual segment. Different segments are then parallel connected by additional metal ribbons into the junction box. The ribbons on the individual segments will certainly result in uneven surface on the back side of the panel. This uneven surface will pose a serious problem for the lamination process. Therefore, the pressure, heat, and air flow need to be carefully designed and precisely controlled during the whole lamination processes to comply with the uneven surface from the additional metal ribbons of low-voltage modules. At the same time, the yield loss from lamination is still kept to be less than 1% even under the complicated layout topography of low-voltage modules. Most importantly, the throughput of lamination is required to be never compromised in the 60 MW production line.

### 3. Results and Discussion

With the above technologies, two kinds of low-voltage tandem amorphous/microcrystalline silicon thin-film solar modules, 30 V and 70 V, were successfully designed and mass produced in Auria's 60 MW production line. Figure 11 shows the  $I$ - $V$  characteristics of a 30 V low-voltage module (LV30) with open-circuit voltage  $V_{oc} = 43.33$  V, short-circuit current  $I_{sc} = 4.843$  A, maximum power voltage  $V_{mpp} = 34.5$  V, and maximum power current  $I_{mpp} = 4.23$  A. Its initial maximum output power is 145.94 W, while its stabilized maximum output power is 130.4 W after the effect of light-induced degradation. Compared with the correspondent crystalline silicon wafer-based solar module, the low-voltage module has better performance in all the aspects of its performance, such as maximum peak power, open-circuit voltage, short-circuit current, and filled factor, as shown in Figure 12.

The characteristic of the LV30 module is approximately correspondent to its counterpart of a typical crystalline silicon wafer-based solar module. A 70 V low-voltage solar module (LV70) is demonstrated with open-circuit voltage  $V_{oc} = 92.6$  V, short-circuit current  $I_{sc} = 2.25$  A, maximum power voltage  $V_{mpp} = 71.3$  V, and maximum power current  $I_{mpp} = 1.83$  A. The characteristic of the LV70 module is closely correspondent to that a typical CdTe thin-film



FIGURE 14: The 900 kW PV system with Auria’s high-performance low-voltage solar modules installed in an agriculture product distribution center near Verona of Italy.

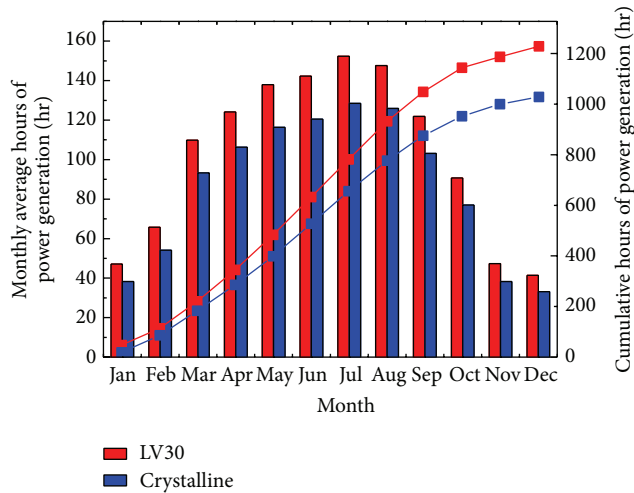


FIGURE 15: Simulation of the average hours power generation per month with the 900 kW LV30 PV system installed near Verona of Italy and its counterpart of a crystalline silicon solar module.

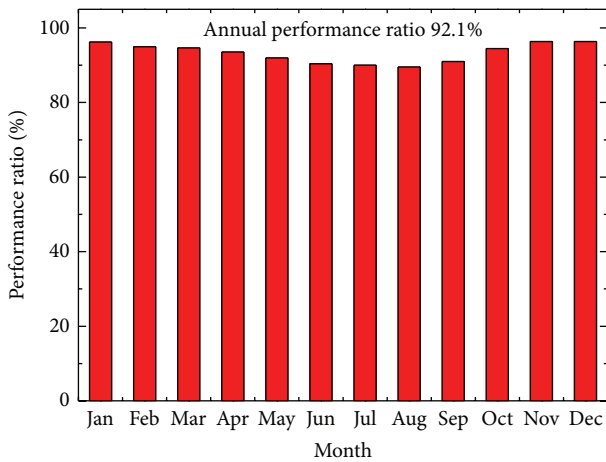


FIGURE 16: Simulation of the performance ratio of the 900 kW LV30 PV system installed near Verona of Italy.

module. It should be noted that our low-voltage modules have been regularly mass produced and their very narrow power distribution (as shown in Figure 13) clearly demonstrates our superb technologies and excellent quality control.

A 900 kW PV system with these high-performance low-voltage modules was installed in an agriculture product

distribution center near Verona of Italy, as shown in Figure 14. The PV panels and inverters are Auria C125 (LV30 type) and SMA Sunny Mini Central 700 HV and the total number of PV modules and inverters are 7200 and 120 units, respectively. According to simulation software PVsyst 5.21 for PV systems, 20% more energy yield per year can be obtained from our 30 V low-voltage solar modules in comparison to that of the crystalline silicon counterparts, as shown in Figure 15. Its performance ratio (PR) has been projected to be 92.1% (as shown in Figure 16) which is better than our regular modules (87.2% PR) and also much better than the crystalline silicon and CdTe counterparts (both around 83~85% PR). In other words, our low-voltage silicon thin-film modules would have energy yield much higher than crystalline Si, CdTe, and CIGS thin-film modules.

#### 4. Conclusion

In short, low-voltage tandem amorphous/microcrystalline silicon thin-film solar modules with high energy yield, low light-induced degradation, and high damp-heat reliability have been successfully designed and mass produced. Several key technologies in passivation, transparent-conducting-oxide films, and cell and segment laser scribing were researched, developed, and introduced into the production

line to enhance the performance these low-voltage modules and narrow their distribution of power rating in mass production. It was demonstrated that low-voltage silicon thin-film modules would generate energy yield much higher than crystalline Si, CdTe, and CIGS thin-film modules. In addition, with their shorter energy payback time due to their low-temperature manufacture processes, low-voltage silicon thin-film modules have higher investment return ratio (IRR).

### Conflict of Interests

The authors declare that there is no conflict of interests regarding the publication of this paper.

### Acknowledgments

The authors would like to thank the help from all the colleagues in Auria Solar. This work is partially funded by the Bureau of Energy of Ministry of Economic Affairs and the National Science Council of Taiwan.

### References

- [1] H. Keppner, J. Meier, P. Torres, D. Fischer, and A. Shah, "Microcrystalline silicon and micromorph tandem solar cells," *Applied Physics A: Materials Science and Processing*, vol. 69, no. 2, pp. 169–177, 1999.
- [2] A. Shah, J. Meier, E. Vallat-Sauvain et al., "Microcrystalline silicon and "micromorph" tandem solar cells," *Thin Solid Films*, vol. 403–404, pp. 179–187, 2002.
- [3] J. Meier, S. Dubail, S. Golay et al., "Microcrystalline silicon and the impact on micromorph tandem solar cells," *Solar Energy Materials and Solar Cells*, vol. 74, no. 1–4, pp. 457–467, 2002.
- [4] A. V. Shah, H. Schade, M. Vanecek et al., "Thin-film silicon solar cell technology," *Progress in Photovoltaics: Research and Applications*, vol. 12, no. 2–3, pp. 113–142, 2004.
- [5] K. Yamamoto, M. Yoshimi, Y. Tawada, Y. Okamoto, and A. Nakajima, "Thin film Si solar cell fabricated at low temperature," *Journal of Non-Crystalline Solids*, vol. 266–269, pp. 1082–1087, 2000.
- [6] K. Yamamoto, M. Yoshimi, Y. Tawada et al., "Large area thin film Si module," *Solar Energy Materials and Solar Cells*, vol. 74, no. 1–4, pp. 449–455, 2002.
- [7] K. Yamamoto, A. Nakajima, M. Yoshimi et al., "A high efficiency thin film silicon solar cell and module," *Solar Energy*, vol. 77, no. 6, pp. 939–949, 2004.
- [8] A. Nakajima, M. Gotoh, T. Sawada et al., "Development of thin-film Si HYBRID solar module," *Solar Energy Materials and Solar Cells*, vol. 93, no. 6–7, pp. 1163–1166, 2009.
- [9] G. E. Bunea, K. E. Wilson, Y. Meydbray, M. P. Campbell, and D. M. de Ceuster, "Low light performance of monocrystalline silicon solar cells," in *Proceedings of the IEEE 4th World Conference on Photovoltaic Energy Conversion*, vol. 2, pp. 1312–1314, Waikoloa, Hawaii, USA, May 2006.
- [10] M. Python, D. Dominé, T. Söderström, F. Meillaud, and C. Ballif, "Microcrystalline silicon solar cells: effect of substrate temperature on cracks and their role in post-oxidation," *Progress in Photovoltaics: Research and Applications*, vol. 18, no. 7, pp. 491–499, 2010.

## Research Article

# High Stability White Organic Light-Emitting Diode (WOLED) Using Nano-Double-Ultra Thin Carrier Trapping Materials

**Kan-Lin Chen**

*Department of Electronic Engineering, Fortune Institute of Technology, Kaohsiung, Taiwan*

Correspondence should be addressed to Kan-Lin Chen; [klchen@fotech.edu.tw](mailto:klchen@fotech.edu.tw)

Received 25 January 2014; Accepted 28 January 2014; Published 6 March 2014

Academic Editor: Chien-Jung Huang

Copyright © 2014 Kan-Lin Chen. This is an open access article distributed under the Creative Commons Attribution License, which permits unrestricted use, distribution, and reproduction in any medium, provided the original work is properly cited.

The structure of indium tin oxide (ITO) (100 nm)/molybdenum trioxide ( $\text{MoO}_3$ ) (15 nm)/N,N'-bis-(1-naphthyl)-N,N'-biphenyl-1,10-biphenyl-4,40-diamine (NPB) (40 nm)/4,4'-Bis(2,2-diphenylvinyl)-1,1'-biphenyl (DPVBi) (10 nm)/5,6,11,12-tetraphenylanthracene (Rubrene) (0.2 nm)/DPVBi (24 nm)/Rubrene (0.2 nm)/DPVBi (6 nm)/4,7-diphenyl-1,10-phenanthroline (BPhen): cesium carbonate ( $\text{Cs}_2\text{CO}_3$ ) (10 nm)/Al (120 nm) with high color purity and stability white organic light-emitting diode (WOLED) was fabricated. The function of the multiple-ultra-thin material (MUTM), such as Rubrene, is as the yellow light-emitting layer and trapping layer. The results show that the MUTM has an excellent carrier capture effect, resulting in high color stability of the device at different applied voltages. The Commissions Internationales De L'Eclairage (CIE) coordinate of this device at 3~7 V is few displacement and shows a very slight variation of ( $\pm 0.01$ ,  $\pm 0.01$ ). The maximum brightness of 9986  $\text{cd/m}^2$  and CIE coordinates of (0.346, 0.339) are obtained at 7 V. The enhanced performance of the device may result from the direct charge trapping in MUTM and it can be found in the electroluminescence (EL) process.

## 1. Introduction

Recently, organic light-emitting diodes (OLED) have attracted a great deal of attention as the new full-color displays and solid-state lighting technology. OLED's superior characteristics such as high brightness, fast response time, wide viewing angle, and low operating voltage allow it to have great potential for commercialization [1–3]. Furthermore, the white organic light-emitting diode (WOLED) lighting technology has been extensively studied. And then, there are several methods to obtain WOLEDs; for example, using a multilayer stack of three primary colors (red, green, and blue), two complementary colors (blue and yellow), and two or three colors of the dye doped into a single host material [4–7]. In the doping codeposition process, to accurately control the evaporation rate and the concentration of two or more materials is very difficult, resulting in its deposition process and reproducibility being poor. However, nondoping technique can accurately control to avoid these problems in the fabrication process. Currently, Tsuji et al. and Xie et al. have reported non-doped-type WOLEDs with the single-ultra-thin layer (SUTL) structure, which is a simple

device structure with good reproducibility, making them very suitable for low-cost lighting applications and conducive to commercialization [8, 9].

In this work, we employ the nondoped method to fabricate WOLEDs with a multiple-ultra-thin material (MUTM) structure. The material of 5-, 6-, 11-, 12-tetraphenylanthracene (Rubrene) was used as yellow light sources in the MUTM structure. Rubrene is the most common nanomaterial, which has good light-emitting efficiency, high color saturation, good stability, and good capture efficiency of charge carriers. In addition, the photoluminescence (PL) quantum efficiency of the Rubrene can be close to 100% [10–13]. And then the material of 4,40-bis(2,20-diphenyl vinyl)-1,10-biphenyl (DPVBi) is a well-known blue fluorescent material. It is usually deemed a host-emitting layer (EML) due to the higher efficiency of blue light. Moreover, DPVBi not only emits but also transfers the incomplete energy from DPVBi to the Rubrene. So far the study of fluorescence WOLED based on the nondoped MUTM is rarely reported. Therefore, we introduced a simple process for the nondoped WOLEDs with an MUTM structure. Meanwhile, the influential factors for the improvement of WOLEDs performance were investigated

in detail. However, the mechanism of the influences of an MUTM structure on the electroluminescence (EL) and the optimal color stability of WOLEDs is also presented.

## 2. Experimental Details

Indium tin oxide (ITO) coated glass with a sheet resistance of approximately  $12\Omega/\text{sq}$  was consecutively cleaned in an ultrasonic bath containing detergent water, acetone, ethanol, and deionized (DI) water for 20 min each, then dried with a nitrogen ( $\text{N}_2$ ) flow. All organic nanomaterials were deposited by high-vacuum ( $10^{-6}$  Torr) thermal evaporation. Thermal deposition rates for organic nanomaterials, inorganic materials, and Al were about  $0.1\text{ \AA}/\text{sec}$ ,  $1\text{ \AA}/\text{sec}$ , and  $10\text{ \AA}/\text{sec}$ , respectively. The evaporation rate and thickness of the thin films were monitored using a quartz crystal oscillator system (Sigma, SID-142). The structures of devices are as follows:

- (A) ITO/molybdenum trioxide ( $\text{MoO}_3$ ; 15 nm)/N,N,N'-bis-(1-naphthyl)-N,N'-biphenyl-1,10-biphenyl-4,4'-diamine (NPB; 40 nm)/DPVBi (10 nm)/Rubrene (0.2 nm)/DPVBi (30 nm)/4,7-diphenyl-1,10-phenanthroline: cesium carbonate (BPhen:  $\text{Cs}_2\text{Co}_3 = 4:1$ ; 10 nm)/aluminum (Al; 120 nm),
- (B) ITO/ $\text{MoO}_3$  (15 nm)/NPB (40 nm)/DPVBi (34 nm)/Rubrene (0.2 nm)/DPVBi (6 nm)/BPhen:  $\text{Cs}_2\text{Co}_3 = 4:1$  (10 nm)/Al (120 nm),
- (C) ITO/ $\text{MoO}_3$  (15 nm)/NPB (40 nm)/DPVBi (10 nm)/Rubrene (0.2 nm)/DPVBi (24 nm)/Rubrene (0.2 nm)/DPVBi (6 nm)/BPhen:  $\text{Cs}_2\text{Co}_3 = 4:1$  (10 nm)/Al (120 nm).

In these devices,  $\text{MoO}_3$  and NPB are used as a hole-injecting layer and hole-transport layer. The DPVBi acts as a blue-emitting layer. The ultrathin Rubrene (UTR) was selected as a yellow light-emitting layer. The BPhen:  $\text{Cs}_2\text{Co}_3$  is used as an electron transporting layer and hole blocking layer. The chemical structures of the organic nanomaterials and the structures of the device are shown in Figure 1. The active area of the device was  $0.4\text{ cm}^2$ . With measuring the properties of the device, a voltage was applied by using a Keithley 2400 programmable voltage-current source (Keithley SourceMeter 2400; USA). EL spectra and CIE coordination of the devices were measured by PR655 spectra scan spectrometer (Kollmorgen Instrument PR655; USA). All measurements were carried out at room temperature in air without encapsulating the devices.

## 3. Results and Discussion

In this study, the WOLED which consists of the blue emission layer and the yellow emission layer was fabricated. The UTR layer was inserted in the light-emitting layer of DPVBi to form the structure of DPVBi (10 nm EML1)/Rubrene (0.2 nm)/DPVBi (30 nm EML2) for device A. The yellow emission of device A was caused by the UTR layer. Figure 2(a) shows the EL spectra of device A at the applied voltage of 3~7 V. The peak wavelengths of the DPVBi layer and

the Rubrene layer were 436 nm and 556 nm, respectively [14, 15]. The intensity of blue emission was higher than that of the yellow emission, and the location of EL spectra for the blue and the yellow emission did not shift as the voltage increased.

In addition, the CIE coordinates of device A at the applied voltage of 3~7 V were shown in Figure 2(b). It was found that the CIE coordinates for device A changed from (0.269, 0.299) at 3 V to (0.249, 0.259) at 7 V. By comparing the CIE coordinates (0.330, 0.330) of standard white light, the error value of the CIE coordinates was about  $(-0.081, -0.071)$  at the 7 V; that is, the shift of the CIE coordinates is about  $(-7.4\%, -13.4\%)$  during the applied voltage of 3~7 V. That is to say, the CIE coordinates of device A were unstable. As for the EL phenomenon in the applied voltage of 3~5 V, some of the holes which were injected from the anode via Rubrene layer into the EML2 can be directly trapped by the UTR layer, which might be due to the effective hole trapping of Rubrene molecules. However, the UTR layer has excellent charge carriers trapping properties, but it is unable to trap lots of the injected holes. On the other hand, the electron mobility in BPhen:  $\text{Cs}_2\text{Co}_3$  of  $3.9 \times 10^{-4}\text{ cm}^2/\text{Vs}$  was less than the hole mobility of  $5.5 \times 10^{-4}\text{ cm}^2/\text{Vs}$  in NPB, so lots of the electrons from an electrode inject just into EML2; that is, the electrons recombine with holes in the EML2 close cathode. Therefore, the electrons were difficult to be directly trapped by the UTR layer at 3~5 V. As a result, the majority of electrons and holes would meet in EML2. Similarly, for the voltage of 6~7 V, more charge carriers were injected into Rubrene layer and EML2, so the amount of recombination for electrons and holes was also relatively increased in Rubrene layer and EML2, resulting in an enhancement in the intensity of peaks, as shown in Figure 2(a). However, the UTR layer in device A cannot trap enough electrons and holes to generate exciton. Therefore, optimum complementary color of the blue and the yellow emission intensity was not achieved.

According to the results obtained above, the best recombination zone was in the EML2 of device A. For device B, the UTR layer inserted in and closed to the cathode to form the structure of DPVBi (34 nm EML1)/Rubrene (0.2 nm)/DPVBi (6 nm EML2) was fabricated. However, by comparing Figures 2(a) and 3(a), it is found that the yellow emission intensity of device B was stronger than that of device A because of its position in the UTR layer being changed. Although the UTR layer was inserted into the best recombination zone and has an excellent charge carrier trapping effect, the blue emission and the yellow emission did not reach the best complementary color.

As mentioned above, the optimal location is in EML2 of device A. Thus, the UTR layer was inserted into a better recombination zone near the EML2/BPhen:  $\text{Cs}_2\text{Co}_3$  interface of device B. The difference between lowest unoccupied molecular orbital (LUMO) energy of Rubrene ( $-3.2\text{ eV}$ ) and that of DPVBi ( $-2.8\text{ eV}$ ) is  $0.4\text{ eV}$ . Similarly, the difference between highest occupied molecular orbital (HOMO) value of Rubrene ( $-5.4\text{ eV}$ ) and that of DPVBi ( $-5.9\text{ eV}$ ) is  $0.5\text{ eV}$  [16, 17]. It is expected that the electrons and holes can be trapped in the UTR layer as well as accumulated in the Rubrene/EML2 interface, leading to an enhancement in

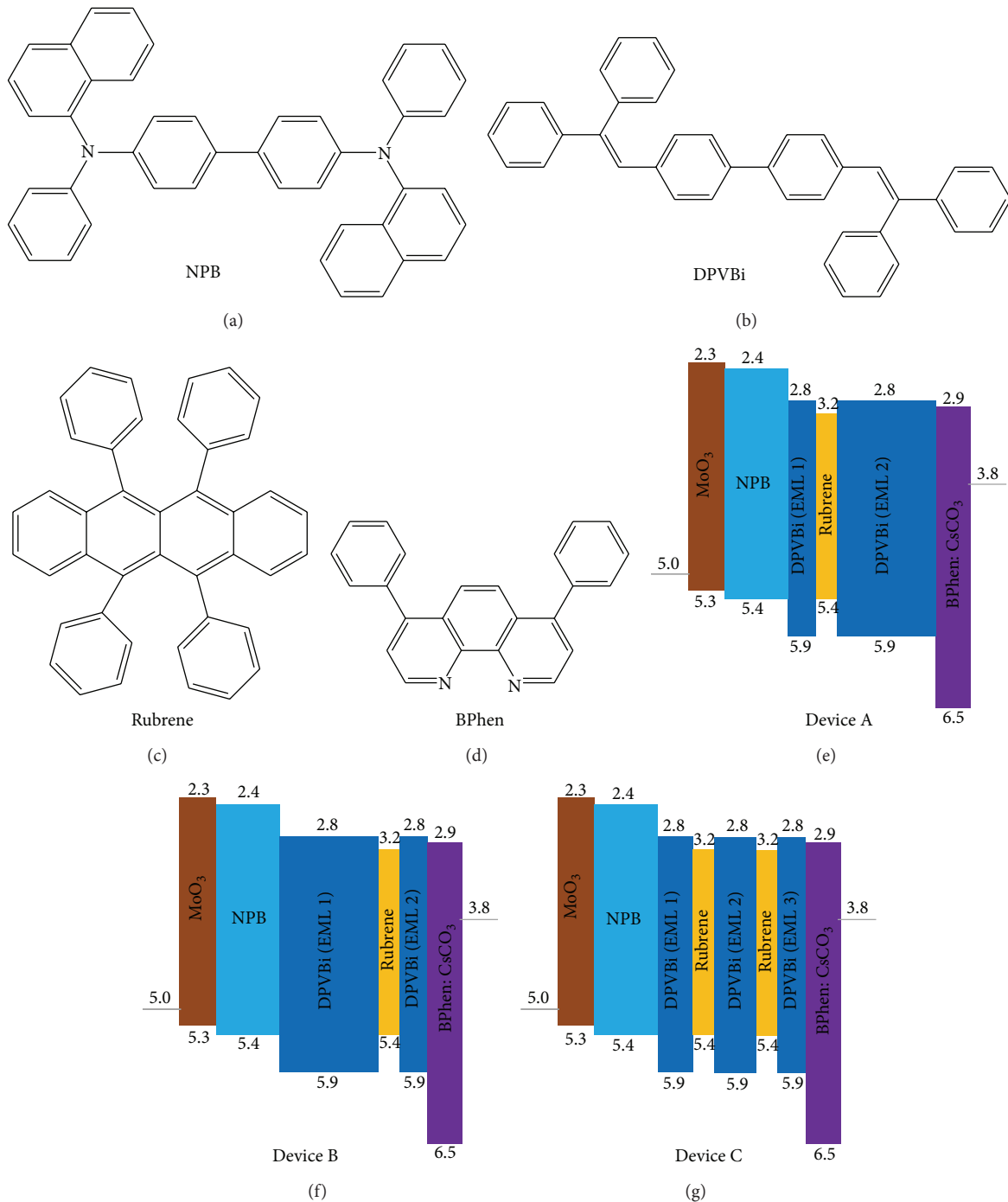


FIGURE 1: The chemical structures of (a) NPB, (b) DPVBi, (c) Rubrene, and (d) BPhen and the schematic energy band diagrams of (e) device A, (f) device B, and (g) device C.

the intensity of yellow emission. Figure 3 shows the EL spectra and CIE coordinates of device B. With the applied voltage increasing, most of the electrons and holes can be directly trapped and recombined to form exciton in the UTR layer. Moreover, the relative intensity of yellow is higher than that of the blue emission; that is, the exciton number of UTR layer is more than that of the DPVBi layer. In Figure 3(a), the intensity of both yellow emission and blue

emission became large, but the ratio of the enhancement in yellow emission is larger than that of blue emission. Thus, the CIE coordinate gradually shifts toward an orientation of white color. For example, when the applied voltage is 3V and 4V, the location of CIE coordinates shows at (0.462, 0.481) and (0.425, 0.437), respectively. By comparing the CIE coordinates of standard white light, the error value of the CIE coordinates was gradually reduced. It is confirmed that the

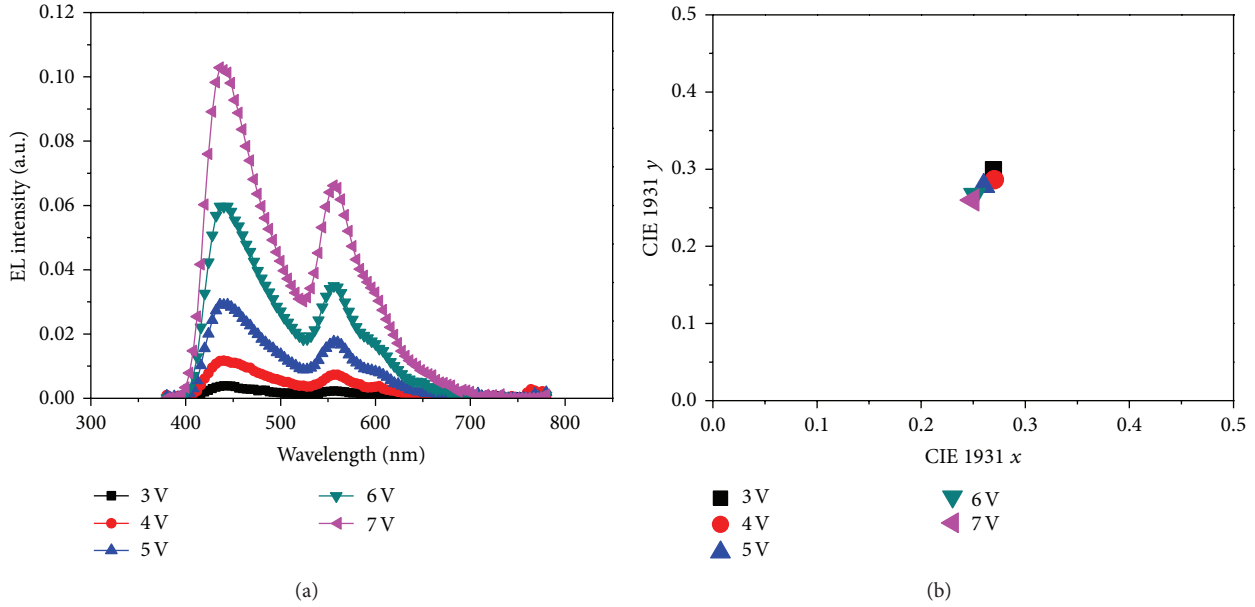


FIGURE 2: (a) The EL spectra of device A at 3~7 V applied voltage. (b) The CIE coordinates of device A at 3~7 V applied voltage.

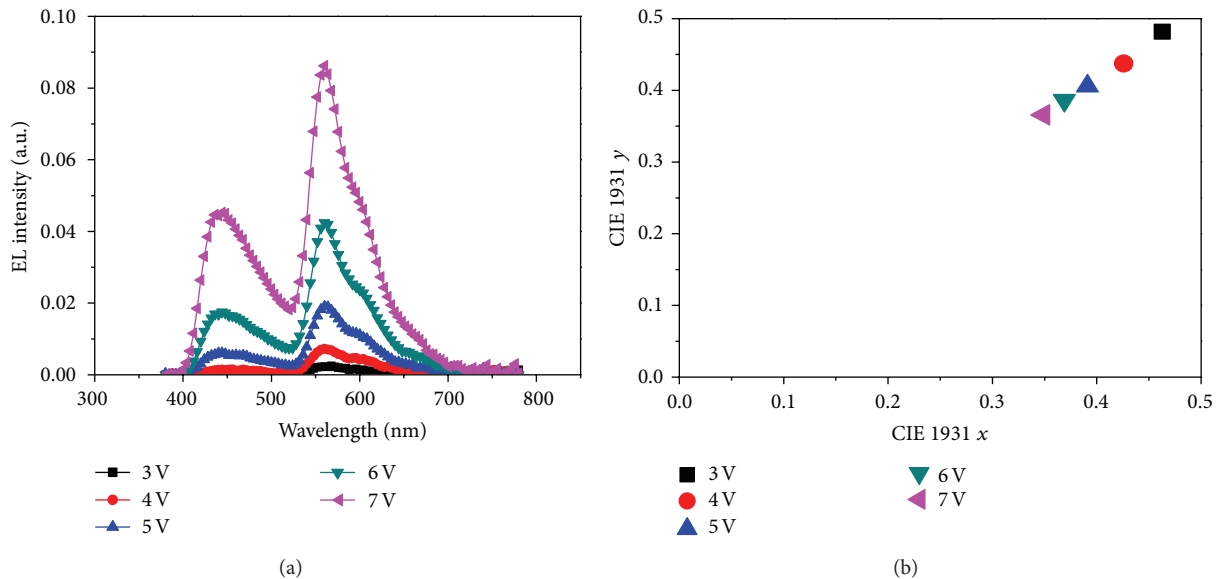


FIGURE 3: (a) The EL spectra of device B at 3~7 V applied voltage. (b) The CIE coordinates of device B at 3~7 V applied voltage.

better recombination zone of device B is in the UTR/EML2 interface.

With the applied voltage increasing to 5 V, the recombination zone of electrons and holes gradually shifts toward the UTR/EML2 interface; the corresponding CIE coordinates are (0.391, 0.405). We thus conjecture that few excitons are generated in the EML2, resulting in an enhancement in the blue emission. On the other hand, more electrons and holes were trapped in the UTR; that is, more excitons are generated in the UTR, leading to an enhanced yellow emission. At the voltage of 6~7 V, CIE coordinates shift again from (0.368, 0.385) to (0.348, 0.365) and gradually shifts

toward the CIE coordinates of standard white light. When a high voltage is applied, the concentration of electrons and holes increases which significantly influences the zone of the exciton generation. The movement of the electrons and holes is similar towards the opposite electrode. Thus, the zone of the exciton generation in device B becomes broad as the EML1/UTR and UTR/EML2 interfaces. This implies that the location of UTR not only improves the color shift of CIE coordinates but also enhances carrier recombination rate. By comparing the CIE coordinates of standard white light, the error value of the CIE coordinates was about (0.018, 0.035) at the 7 V; that is, the shift of the CIE coordinates is about

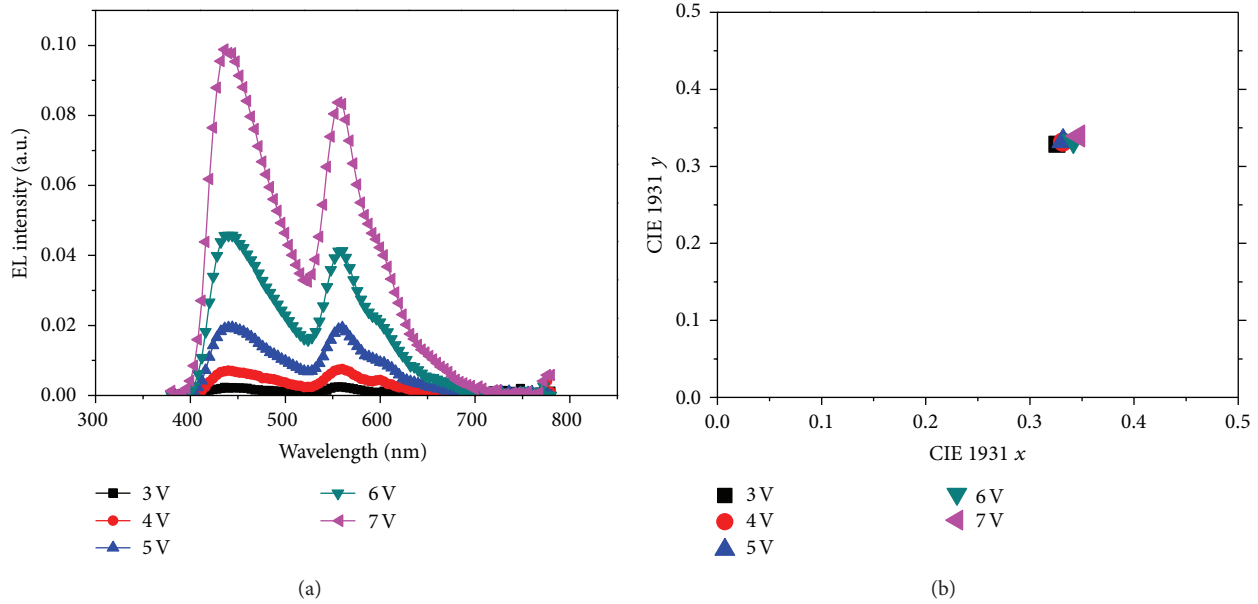


FIGURE 4: (a) The EL spectra of device C at 3~7 V applied voltage. (b) The CIE coordinates of device C at 3~7 V applied voltage.

(−24.7%, −24.1%) during the applied voltage of 3~7 V. With the results obtained above, the CIE coordinates of device B are close to the CIE coordinates of standard white light by the ultrathin Rubrene layer inserted into EML2, but the CIE coordinates of device B are still unstable during the applied voltage of 3~7 V.

Figure 4 shows the EL spectra and CIE coordinates of device C, ITO/MoO<sub>3</sub>/NPB/DPVBi/Rubrene/DPVBi/Rubrene/DPVBi/BPhen: Cs<sub>2</sub>Co<sub>3</sub>/Al, during the applied voltage of 3~7 V. It is found that there is a balance or complementary color in blue emission and yellow emission, as shown in Figure 4(a). Besides, at the applied voltage of 5 V, a pure white emission with CIE coordinates of (0.332, 0.332) is observed. When the voltage continued to increase to 6 and 7 V, the CIE coordinates were, respectively, (0.342, 0.332) and (0.345, 0.338), and showed little change. This is due to the fact that the ratio of blue and yellow emission intensity from EL spectra of Figure 4(a) is almost the same and about unit. Furthermore, this improvement in chromaticity can be attributed to the MUTM structure in the emission layer, resulting in a balance in the relative intensity of blue and yellow emission. Thus, by introducing an MUTM structure in the emission layer, the WOLED has more stable spectra characteristics than that of devices A and B with the increase of bias voltage. This is due to the reason that the injection of holes and electrons was enhanced by the MUTM structure and that the MUTM structure can enhance charge carrier trapping in the EML1/Rubrene, EML2/Rubrene, and Rubrene/EML3 interfaces. And then the enhanced carrier injection was because electric fields were induced by the accumulated carrier at the MUTM. This result is similar to the result discussed in other literatures [18–21]. In other words, the excitons formed from electrons and holes can widely distribute in the entire emission layer. As is expected, the excitons of Rubrene and DPVBi layers will increase and

reach balance, indicating that the MUTM can enhance color stability of CIE coordinates and chromaticity of pure white emission. However, the difference of the CIE coordinates during the applied voltage of 3~7 V is almost null which is advantageous for lighting application.

The current density-voltage-luminance characteristics of devices A~C are shown in Figure 5. The maximum current density of devices A, B, and C is 204 mA/cm<sup>2</sup>, 298 mA/cm<sup>2</sup>, and 356 mA/cm<sup>2</sup> at 7 V, respectively. It can be seen that device C shows larger current density than the other two devices at the same voltage. This is the reason why it has larger luminance. The maximum luminance of devices A–C is 6013 cd/m<sup>2</sup>, 7769 cd/m<sup>2</sup>, and 9986 cd/m<sup>2</sup>, respectively. It can be explained that the holes were accumulated at the Rubrene/EML3 interface and that the electrons were accumulated at the BPhen: Cs<sub>2</sub>Co<sub>3</sub> layer, indicating that the electric field can be formed in EML3. The electric field is favorable for electron injection into the emission layer. However, it is expected that the holes were trapped and confined in the Rubrene/EML3 interface and electron injection thus enhanced, resulting in that an improved carrier balance was achieved. Moreover, when the MUTM structure was inserted into the emission layer, the current density rising in device C exceeds those in the other devices. The phenomenon can be attributed to the effect of Coulomb attractive force (CAF) that is due to the presence of the trapped and accumulated holes in the emission layer [22]. That is to say, more accumulated holes in the HOMO level of DPVBi/Rubrene/DPVBi potential well will generate the stronger CAF for electron, resulting in a better injection of electron from ETL to EML layer. Thus, the current density rising depends on the position and the number of the ultrathin layer, that is, the formation of MUTM.

Figure 6 shows the current efficiency and power efficiency of the device with and without MUTM. In Figure 6(a), the

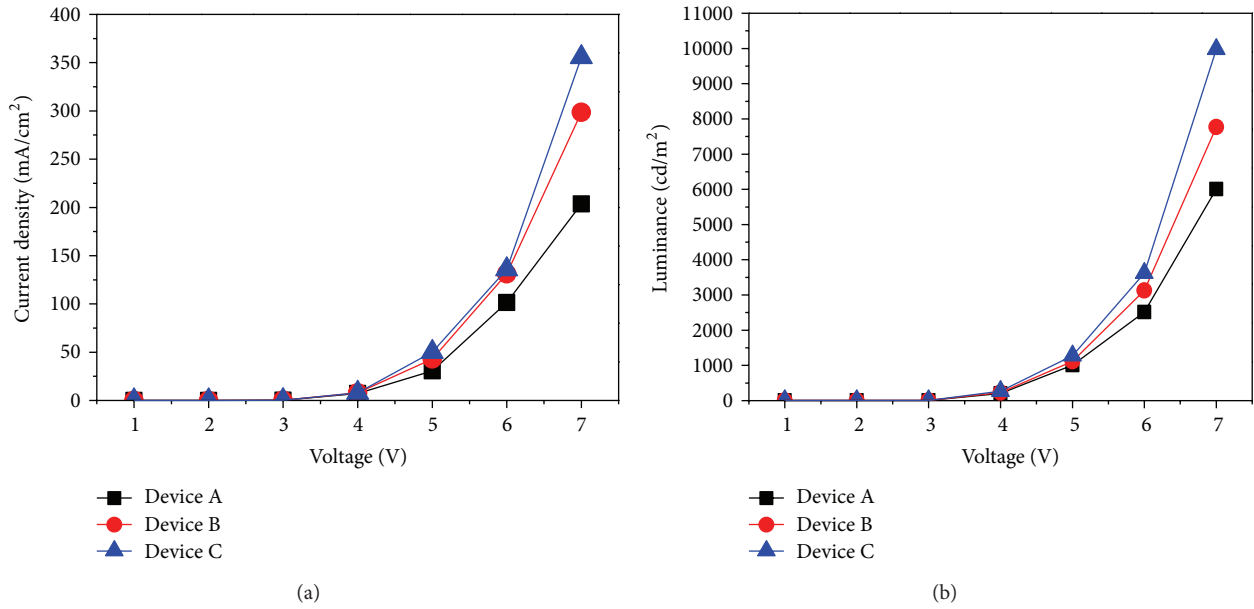


FIGURE 5: (a) The current density versus bias voltage (J-V) characteristics of devices A~C. (b) The luminance versus bias voltage (L-V) characteristics of devices A~C.

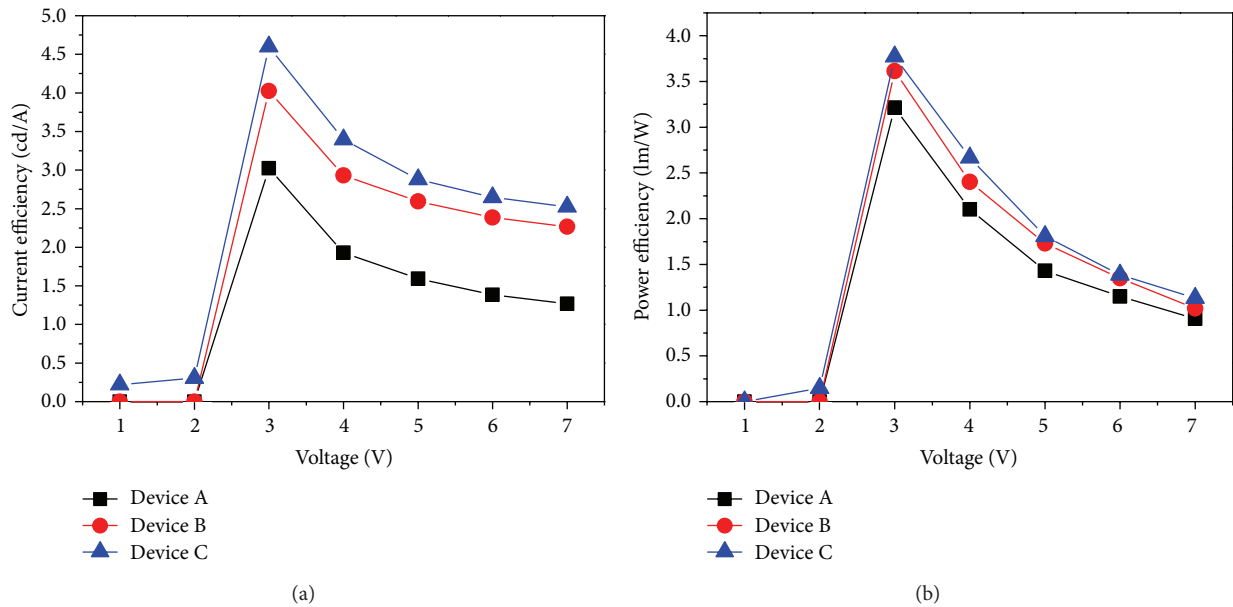


FIGURE 6: (a) The current efficiency versus bias voltage characteristics of devices A~C. (b) The power efficiency versus bias voltage characteristics of devices A~C.

current efficiency of device C with MUTM is of good and exceeds that without MUTM. At the applied voltage of 3 V, devices A, B, and C show the maximum current efficiency of 3.02, 4.02, and 4.6 cd/A, respectively. These values indicate that the recombination rate of electron-hole pairs in device C exceed those in the other devices. In Figure 6(b), the maximum power efficiency of devices A~C is 3.2, 3.6, and 3.7 lm/W, respectively. It can be seen that device C with the MUTM structure has a high power efficiency than the other two devices. As is known, the power efficiency depends on

carrier injection, while current efficiency not only depends on the carrier injection, but also on the carrier balance. On the contrary, an unbalanced injection of electron-hole pairs in the EML with excess carrier injection reduces the efficiency due to the effect of carrier quench. Thus, the high current efficiency and power efficiency of the device can be achieved at an efficient carrier balance. However, the MUTM structure with high carrier trapped efficiency leads to the formation of stronger CAF, which enhances the efficiency of the device.

## 4. Conclusions

In summary, white light emission was achieved by inserting the MUTM structure in the emission layer. The carrier trapping mechanism of the MUTM structure can more effectively confine electrons and holes in the emission layer. Consequently, the excitons of Rubrene and DPVBi layers will increase and reach balance; that is, there is a balance or complementary color in blue emission and yellow emission, resulting in good color stability characteristics of WOLED at different applied voltages. Pure white emission CIE coordinates of (0.332, 0.332) can be obtained and show little change at the applied voltage of 3~7 V. It is demonstrated that EL emission is less dependent on the applied voltage. Furthermore, a device with a MUTM structure increased carrier trapping probability to improve carrier recombination, current density, and luminance intensity.

## Conflict of Interests

The authors declare that there is no conflict of interests regarding the publication of this paper.

## Acknowledgments

The author thanks the Research Center for Electro-Optical and Semiconductor, Southern Taiwan University of Technology, Taiwan, for fabrication and measurements of WOLED. The author would also like to thank Dr. Chien-Jung Huang and Mr. Fong-Yi for their discussion and support.

## References

- [1] C. J. Huang, T. H. Meen, S. L. Wu, and C. C. Kang, "Improvement of color purity and electrical characteristics by co-doping method for flexible red-light organic light emitting devices," *Displays*, vol. 30, no. 4-5, pp. 164-169, 2009.
- [2] D. W. Chou, K. L. Chen, C. J. Huang, W. R. Chen, and T. H. Meen, "Effect of post-annealing treatment on silicon dioxide films for passivating flexible organic light-emitting diode," *Solid-State Electronics*, vol. 79, pp. 130-132, 2013.
- [3] C. J. Huang, C. C. Kang, T. C. Lee, W. R. Chen, and T. H. Meen, "Improving the color purity and efficiency of blue organic light-emitting diodes (BOLED) by adding hole-blocking layer," *Journal of Luminescence*, vol. 129, no. 11, pp. 1292-1297, 2009.
- [4] J. Kido, H. Shionoya, and K. Nagai, "Single-layer white light-emitting organic electroluminescent devices based on dye-dispersed poly(*N*-vinylcarbazole)," *Applied Physics Letters*, vol. 67, no. 16, pp. 2281-2283, 1995.
- [5] K. Okumoto, H. Kanno, Y. Hamada, H. Takahashi, and K. Shibata, "High efficiency red organic light-emitting devices using tetraphenyldibenzoperiflanthene-doped rubrene as an emitting layer," *Applied Physics Letters*, vol. 89, no. 1, Article ID 013502, 3 pages, 2006.
- [6] G. Li and J. Shinar, "Combinatorial fabrication and studies of bright white organic light-emitting devices based on emission from rubrene-doped 4,4'-bis(2,2'-diphenylvinyl)-1,1'-biphenyl," *Applied Physics Letters*, vol. 83, no. 26, pp. 5359-5361, 2003.
- [7] K. T. Kamtekar, A. P. Monkman, and M. R. Bryce, "Recent advances in white organic light-emitting materials and devices (WOLEDs)," *Advanced Materials*, vol. 22, no. 5, pp. 572-582, 2010.
- [8] T. Tsuji, S. Naka, H. Okada, and H. Onnagawa, "Nondoped-type white organic electroluminescent devices utilizing complementary color and exciton diffusion," *Applied Physics Letters*, vol. 81, no. 18, pp. 3329-3331, 2002.
- [9] W. F. Xie, Z. J. Wu, S. Y. Liu, and S. T. Lee, "Non-doped-type white organic light-emitting devices based on yellow-emitting ultrathin 5,6,11,12-tetraphenylnaphthacene and blue-emitting 4,4'-bis(2,2'-diphenylvinyl)-1,1'-biphenyl," *Journal of Physics D*, vol. 36, no. 19, pp. 2331-2334, 2003.
- [10] H. Mattoussi, H. Murata, C. D. Merritt, Y. Iizumi, J. Kido, and Z. H. Kafafi, "Photoluminescence quantum yield of pure and molecularly doped organic solid films," *Journal of Applied Physics*, vol. 86, no. 5, pp. 2642-2650, 1999.
- [11] Y. M. Wang, F. Teng, Z. Xu, Y. B. Hou, S. Y. Yang, and X. R. Xu, "Trap effect of an ultrathin DCJTb layer in organic light-emitting diodes," *Materials Chemistry and Physics*, vol. 92, no. 2-3, pp. 291-294, 2005.
- [12] M. Matsumura and T. Furukawa, "Efficient electroluminescence from a rubrene sub-monolayer inserted between electron- and hole-transport layers," *Japanese Journal of Applied Physics*, vol. 40, no. 5, pp. 3211-3214, 2001.
- [13] T. Li, X. Li, W. Li et al., "Tunable red emission by incorporation of a rubrene derivative in *p*-type and *n*-type hosts in organic light emitting devices," *Thin Solid Films*, vol. 517, no. 16, pp. 4629-4632, 2009.
- [14] C.-J. Huang, T.-H. Meen, K.-C. Liao, and Y.-K. Su, "The mechanism of efficiency enhancement with proper thickness of DPVBi layer for blue organic light-emitting devices (BOLED)," *Journal of Physics and Chemistry of Solids*, vol. 70, no. 3-4, pp. 765-768, 2009.
- [15] Q. Xue, S. Zhang, G. Xie et al., "Efficient fluorescent white organic light-emitting devices based on a ultrathin 5,6,11,12-tetraphenylnaphthacene layer," *Solid-State Electronics*, vol. 57, no. 1, pp. 35-38, 2011.
- [16] D. Xu, X. Li, H. Ju, Y. Zhu, and Z. Deng, "A novel red organic light-emitting diode with ultrathin DCJTb and Rubrene layers," *Displays*, vol. 32, no. 2, pp. 92-95, 2011.
- [17] X. Y. Zheng, W. Q. Zhu, Y. Z. Wu et al., "A white OLED based on DPVBi blue light emitting host and DCJTb red dopant," *Displays*, vol. 24, no. 3, pp. 121-124, 2003.
- [18] L. Li, J. Yu, X. Tang, T. Wang, W. Li, and Y. Jiang, "Efficient bright white organic light-emitting diode based on non-doped ultrathin 5,6,11,12-tetraphenylnaphthacene layer," *Journal of Luminescence*, vol. 128, no. 11, pp. 1783-1786, 2008.
- [19] X. Tang, J. Yu, L. Li, L. Zhang, and Y. Jiang, "White organic light-emitting diodes with improved performance using phosphorescent sensitizer and ultrathin fluorescent emitter," *Displays*, vol. 30, no. 3, pp. 123-127, 2009.
- [20] S. H. Yang, B. C. Hong, and S. F. Huang, "Luminescence enhancement and emission color adjustment of white organic light-emitting diodes with quantum-well-like structures," *Journal of Applied Physics*, vol. 105, no. 11, Article ID 113105, 7 pages, 2009.
- [21] Z. Ma, J. Yu, L. Li, and Y. Jiang, "Non-doped white organic light-emitting diodes consisting of three primary colors based on a bipolar emitter," *Displays*, vol. 33, no. 1, pp. 42-45, 2012.
- [22] Q. Xu, J. Ouyang, Y. Yang, T. Ito, and J. Kido, "Ultra-high efficiency green polymer light-emitting diodes by nanoscale interface modification," *Applied Physics Letters*, vol. 83, no. 23, pp. 4695-4697, 2003.

## Research Article

# Theoretical Study of the Effects of Carrier Transport, Capture, and Escape Processes on Solar Cells with Embedded Nanostructures

**Chin-Yi Tsai**

*Department of Applied Physics, National University of Kaohsiung, Kaohsiung 811, Taiwan*

Correspondence should be addressed to Chin-Yi Tsai; [chinyitsai@hotmail.com](mailto:chinyitsai@hotmail.com)

Received 12 January 2014; Accepted 18 January 2014; Published 24 February 2014

Academic Editor: Chien-Jung Huang

Copyright © 2014 Chin-Yi Tsai. This is an open access article distributed under the Creative Commons Attribution License, which permits unrestricted use, distribution, and reproduction in any medium, provided the original work is properly cited.

A theoretical model is proposed to study the effects of carrier transport, escape, and capture processes on solar cells with embedded nanostructures. The theoretical results clearly indicate that the carrier transport, escape, and capture times are important physical quantities affecting the performance of solar cells with embedded nanostructures and they should be fully considered in device design, such as the selection of the optimal band-gap energy of the nanostructures. The beneficial results from the embedded nanostructures cannot be warranted. Slow escape processes and long transport time will make the nanostructures act as gigantic recombination sites and cause a detrimental effect on the bulk solar cell. The results show that solar cells embedded with nanostructures of very small band-gap energy materials will suffer from extremely slow escape processes due to a very large potential difference between the nanostructures and the bulk host material; therefore, their output photocurrent could be inferior to their bulk counterparts without the nanostructures. The beneficial results from the embedded nanostructures to the solar cells can only be realized by their long carrier lifetime and fast escape time.

## 1. Introduction

There exist ongoing efforts to improve the efficiency of solar cells. Solar cells embedded with nanostructures of smaller band-gap energy to form various quantum structures, such as quantum wells, wires, or dots, undoubtedly provide an interesting subject worth of more investigations [1, 2]. The fact that the device performance demonstrated by quantum-well lasers is far more superior to their bulk counterparts [3, 4] somehow suggests that solar cells embedded with nanostructures might have better performances than their bulk counterpart. This is not a pure conjecture because the major advantage of embedding nanostructures of smaller band-gap energy into solar cells is that the nanostructures can absorb the additional photons below the band-gap energy of the bulk host material. In fact, using different materials to absorb different spectral portions of sunlight is a well-known practice for improving the efficiency of solar-cells. It can be achieved by using various methods and configurations,

such as beam-splitting, mechanically stacking, heterojunction, and tandem structures. Embedding nanostructures of smaller band-gap energy directly into existing bulk solar cells certainly could achieve broader absorption of solar spectrum, as shown schematically in Figure 1. The nanostructures of smaller band-gap energy embedded in the bulk host material with larger band-gap energy, depending on their configurations and formations, will consequently constitute various quantum structures, such as quantum wells, wires, or dots. In fact, the quantum-well and quantum-dot solar cells have been experimentally realized and their performance is rather promising [1].

In spite of the promising features of solar cells embedded with nanostructures, there are some outstanding questions and problems in the device design remaining to be answered or solved, for example, the optimal band-gap energy of the nanostructures. As we know, deeper nanostructures can absorb a wider spectrum of the incident sunlight; however, they inevitably suffer from slower carrier escape processes.

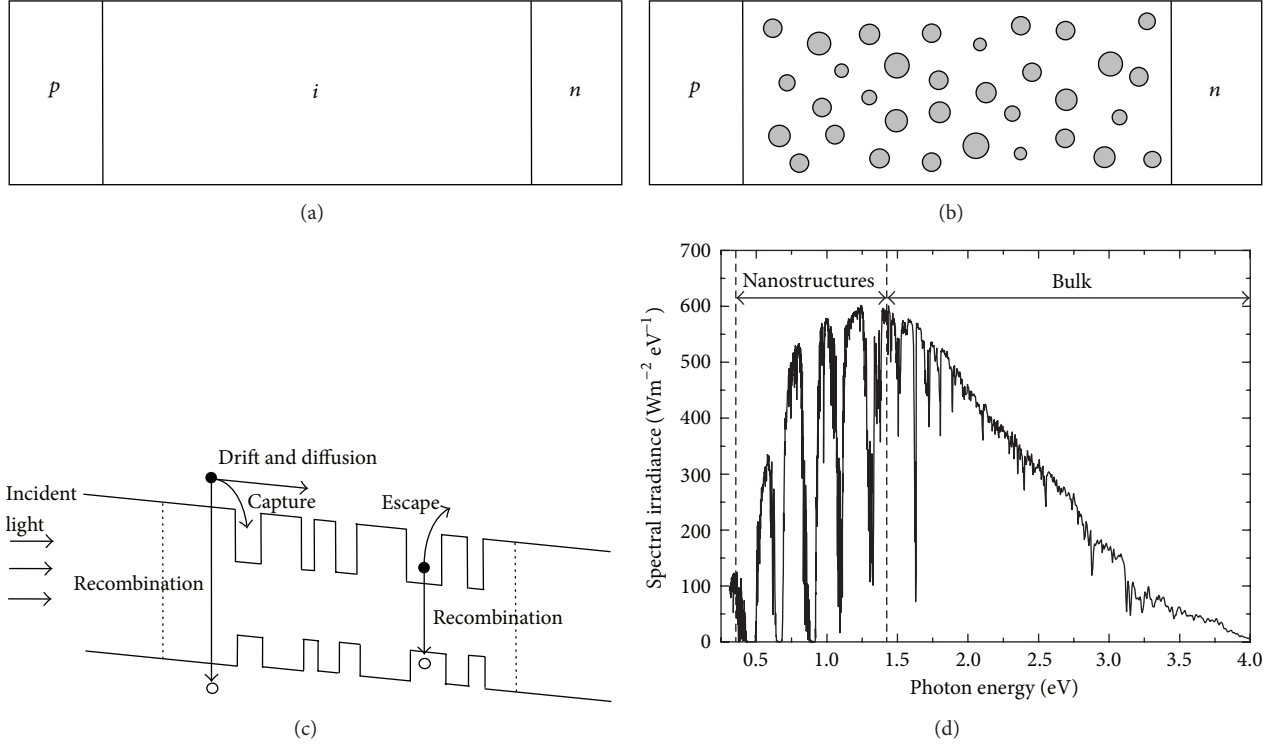


FIGURE 1: (a) A schematic diagram of a  $p$ - $i$ - $n$  bulk solar cell. (b) A schematic diagram of a  $p$ - $i$ - $n$  solar cell embedded with nanostructures in which the gray dots indicate the nanostructures. (c) A schematic energy band diagram of a  $p$ - $i$ - $n$  solar cell embedded with nanostructures. (d) The ranges of light absorption from the bulk material (GaAs) and the nanostructures (InAs). The solar spectrum is AM1.5 normalized to the  $1000 \text{ W/m}^2$  standard test condition.

In other words, carriers generated in the nanostructures with deep potential wells cannot efficiently escape from the nanostructures into the bulk materials and then transport out of the device to contribute as useful output photocurrents. In fact, carrier transport, capture, and escape processes are one of the key issues that determine the performance of quantum-well and quantum-dot lasers and their effects on the devices have been intensively investigated and discussed [3]. However, the effects of carrier transport, capture, and escape processes on solar cells embedded with nanostructures are not well studied yet [5–7].

## 2. Theoretical Model

In this work, a simple but rather illustrative theoretical model will be proposed to investigate the effects of carrier transport, capture, and escape processes on the photocurrent of solar cells embedded with nanostructures. A bulk  $p$ - $i$ - $n$  solar cell is adopted and nanostructures (e.g., quantum dots) are formed in the bulk  $i$ -region, as shown schematically in Figure 1. To focus our discussion on the effects of carrier transport, capture, and escape processes on this solar cell, a simple 2- $N$  model is used, in which the device is controlled by the carrier population of the unconfined states of the bulk material in the  $i$ -region,  $N_b$ , and that of the confined states of the nanostructures,  $N_w$ . Photocurrents contributed from the bulk  $p$ - and  $n$ -regions are assumed to be omitted for

simplicity. The assumptions and validity of this model have been discussed in our previous work for quantum-well lasers and will not be reiterated here [8]. Of course, more complicated models such as many- $N$  or distributed models with separated roles of electrons and holes can be implemented, but it is likely to make theoretical models less transparent and might obscure the essential results presented in this work. The rate equations of carrier populations  $N_b$  and  $N_w$  of this model are given as

$$\frac{dN_b}{dt} = \frac{I_b}{q} + \frac{N_w}{\tau_{\text{esc}}} - \frac{N_b}{\tau_{\text{cap}}} - \frac{N_b}{\tau_b} - \frac{N_b}{\tau_d}, \quad (1)$$

$$\frac{dN_w}{dt} = \frac{I_w}{q} - \frac{N_w}{\tau_{\text{esc}}} + \frac{N_b}{\tau_{\text{cap}}} - \frac{N_w}{\tau_w}. \quad (2)$$

Here  $q$  is the elementary charge.  $I_b$  and  $I_w$  are the photocurrents generated by the light absorption of the bulk material and the nanostructures; respectively.  $\tau_b$  and  $\tau_w$  are carrier lifetimes of the bulk material and the nanostructures, respectively. They are resulted from various recombination processes, such as, Shockley-Read-Hall (SRH), emission of photon, Auger, and interface recombination processes:

$$I_R = I_{\text{SRH}} + I_{\text{photon}} + I_{\text{Auger}} + I_{\text{interface}} + \dots, \quad (3)$$

where  $I_{Rb}/q = N_b/\tau_b$  and  $I_{Rw}/q = N_w/\tau_w$  represent the recombination currents in the bulk material and the nanostructures, respectively. The contributions of these recombination processes could be rather different for different materials and structures. For example, the SRH recombination is usually the dominant one in the indirect band-gap semiconductors, while the recombination via the emission of photon could be the most significant one in the direct band-gap semiconductors. On the other hand, for ill-form nanostructures, the interface recombination could be possibly the most dominant one.  $\tau_{esc}$  and  $\tau_{cap}$  are the carrier escape and capture times, respectively.  $\tau_d$  is the carrier transport (i.e., drift and diffusion) time across the bulk  $i$ -region.

As shown schematically in Figure 1, (1) describes that carriers in the bulk material would recombine in the bulk material, captured into the nanostructures, or transport across the bulk region to contribute as the output photocurrent. Similarly, (2) describes that carriers in the nanostructures would either recombine inside the nanostructures or escape into the bulk materials. It should be noted that the carrier transport, capture, and escape models presented in (1) and (2) are rather universal and could be used for the cases of quantum wells, wires, dots, and other similar nanostructures by adopting their correspondent carrier lifetimes and carrier transport, capture, and escape times for specific cases which will be discussed in the following.

It has been theoretically shown that the carrier capture and escape times are in fact defined from the carrier net capture current  $I_{net}$  as [8]

$$\frac{I_{net}}{q} = \frac{N_w}{\tau_{esc}} - \frac{N_b}{\tau_{cap}}. \quad (4)$$

If the carrier capture/escape processes proceed via the emission/absorption of phonons, it has been shown that the net capture current  $I_{net}$  could be theoretically calculated from the first principle and thus the capture and escape times can be theoretically obtained for the case of quantum wells [8, 9]. In our previous work, the carrier escape and capture processes between the unconfined bulk states and the confined quantum states have been calculated from the first principle by evaluating the carrier-polar optical phonon interactions, and the details of their physical meaning have been discussed and will not be repeated here for simplicity.

For solar cells, the devices effectively operate at DC steady state; that is,  $dN_b/dt = dN_w/dt = 0$ ; as a result, (1) and (2) can be presented in a form of the so called ‘‘charge-control model’’ as

$$\begin{aligned} I_b - I_{net} - I_{Rb} &= I_\lambda, \\ I_w + I_{net} - I_{Rw} &= 0, \end{aligned} \quad (5)$$

where  $I_\lambda$  are the output photocurrent,  $I_{net}$  are net capture current,  $I_{Rb}$  and  $I_{Rw}$  are the recombination currents in the bulk and the nanostructures, respectively. Note that the output photocurrent is defined as  $I_\lambda/q = N_b/\tau_d$ . It describes that carriers in the bulk material must transport via drift and diffusion processes across the bulk  $i$ -region, before being recombined or captured into the nanostructures, and

contribute as the useful output photocurrent. In fact, the carrier net capture current  $I_{net}$ , the recombination currents in the bulk material  $I_{Rb}$ , and the recombination current in the nanostructures  $I_{Rw}$  in (5) can be calculated from the first principles, and thus the correspondent time constants can be evaluated by  $I_{net}/q = N_b/\tau_{cap} - N_w/\tau_{esc}$ ,  $I_{Rb}/q = N_b/\tau_b$ , and  $I_{Rw}/q = N_w/\tau_w$  for a given specific operating condition.

From the addition of (3) and (4), the output photocurrent  $I_\lambda$  is simply the superposition of the input photocurrent  $I_{photon} = I_b + I_w$  generated by the absorption of the incident sunlight and the dark current  $I_{dark} = I_{Rb} + I_{Rw}$  due to the recombination processes:

$$I_\lambda = I_{photon} - I_{dark} = (I_b + I_w) - (I_{Rb} + I_{Rw}), \quad (6)$$

as in the general case of a solar cell. The result of (6) clearly indicates that the superposition form of the photocurrent and the dark current for solar cells is still valid even with the inclusion of carrier transport, capture, and escape processes into the theoretical model. Similar forms of (6) have been used by several previous works without considering the effect of carrier escape and capture processes (i.e.,  $I_{net} = 0$ ) in quantum-well solar cells [10].

There are several possible routes for a carrier to escape from a nanostructure to become a free carrier, such as phonon-assisted, photo-assisted, intraband and interband (i.e., Auger) carrier-assisted, and direct tunneling. Usually, phonon-assisted and direct tunneling are the two major channels for carrier escape processes. For typical  $p$ - $i$ - $n$  solar cells with electric field in an  $i$ -region much less than 50 kV/cm, the phonon-assisted escape process is known to be the dominant escape process in a quantum well [11]. In our previous work, the carrier escape and capture processes between the unconfined bulk states and the confined quantum states have been calculated from the first principle by evaluating the carrier-polar optical phonon interactions, and the details of their physical meaning have been discussed and will not be repeated here [8, 9]. The results indicate that the quasi-Fermi energy of the confined states must be different from that of the unconfined states in order to have a net current flow between them. It should be noted that the escape and capture processes actually do not consume any photocurrent; they simply determine the proportion of the carrier populations (or more precisely, the quasi-Fermi energy levels) between the bulk material and the nanostructures. This quasi-Fermi energy separation between the bulk material and nanostructures will consequently modify the proportion of the dark recombination currents in the bulk and the nanostructures, and then the output current and voltage will be determined by the carriers in the bulk material transporting via drift and diffusion processes across the active region.

### 3. Results and Discussion

As it has been pointed out in our previous publication, the escape and capture times are not constants and they depend on the quasi-Fermi energy levels (and thus the carrier densities) in the bulk material and nanostructures. If this is the case, then the theoretical model of (1) and (2) should be

solved and calculated numerically. However, if the escape and capture times are treated as time constants for a device at a given specific operating condition, the output photocurrent can be expressed by

$$I_\lambda = \frac{I_b(\gamma + 1) + I_w\gamma}{1 + \alpha + \beta + \gamma + \gamma\beta}, \quad (7)$$

where the ratios between different time constants are defined as

$$\alpha \equiv \frac{\tau_d}{\tau_{\text{cap}}}, \quad \beta \equiv \frac{\tau_d}{\tau_b}, \quad \gamma \equiv \frac{\tau_w}{\tau_{\text{esc}}}. \quad (8)$$

These dimensionless parameters can be viewed as the indicators for the efficiencies of capture, transport, and escape processes, respectively. Note that if  $1/\tau_b = 1/\tau_w = 0$  is assumed, a hypothetical case of infinite carrier lifetimes due to negligible recombination processes, the output photocurrent will become  $I_\lambda = I_b + I_w$ , which represents the theoretical maximum photocurrent that can be produced from a solar cell. In another hypothetical case of infinite carrier escape time, that is,  $1/\tau_{\text{esc}} = 0$ , the photocurrent will become

$$I_\lambda = \frac{I_b}{1 + \alpha + \beta} = I_b \frac{1/\tau_d}{1/\tau_d + 1/\tau_b + 1/\tau_{\text{cap}}}. \quad (9)$$

It means that carriers cannot escape from the nanostructures and thus the nanostructures have no contribution for the output photocurrent at all, while the capture processes will make the nanostructures acting as recombination sites. Under such circumstances, solar cells embedded with nanostructures are even inferior to their bulk counterparts, and the inclusion of nanostructures will only degrade the efficiency of the device and totally lose its purpose. This just illustrates the importance of the carrier escape processes on the performance of solar cells embedded with nanostructures. Furthermore, if the carrier capture time is assumed to be infinite (i.e.,  $1/\tau_{\text{cap}} = 0$ ); in other words, the existence of the nanostructures will have no physical effects at all on the solar cell. In such cases, the output photocurrent can simply be calculated by

$$I_\lambda = \frac{I_b}{1 + \alpha} = I_b \frac{1/\tau_d}{1/\tau_d + 1/\tau_b}. \quad (10)$$

Similar form as (10) has been proposed to study the effect of carrier transport on a bulk  $p$ - $i$ - $n$  solar cell [12].

In our following discussion,  $\tau_d$  is the combination of carrier drift and diffusion times:

$$\frac{1}{\tau_d} = \frac{1}{\tau_{\text{drift}}} + \frac{1}{\tau_{\text{diff}}}. \quad (11)$$

The drift time can be calculated by  $\tau_{\text{drift}} = L_b/v_{\text{drift}}$ , where  $L_b$  is the width the active bulk  $i$ -region and  $v_{\text{drift}}$  is the carrier average drift velocity, which is the sum of the contribution from electrons and holes  $v_{\text{drift}} = v_n + v_p$  since the output photocurrent is contributed by electrons and holes separately. For a typical electric field  $E \sim 10$  kV/cm in a  $p$ - $i$ - $n$  solar cell, the ‘‘high-field’’ effect in carriers’ drift velocities might be

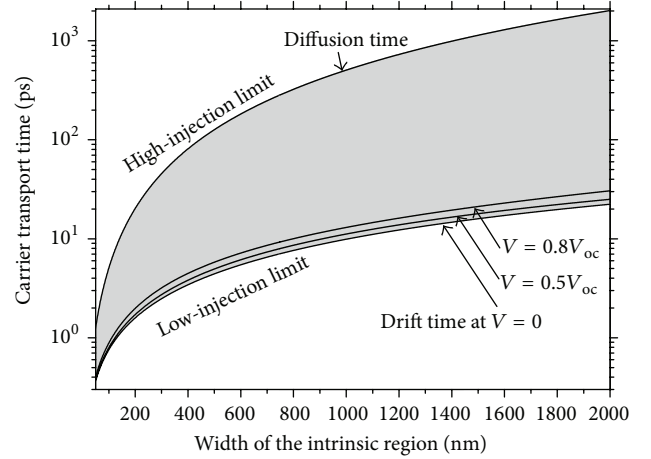


FIGURE 2: Carrier transport (diffusion and drift) times as a function of the width of the intrinsic region for different output voltages of a  $p$ - $i$ - $n$  GaAs bulk solar cell.  $V_{\text{oc}}$  stands for the open-circuit voltage. Note that the carrier transport is mainly limited by the drift process at low-injection conditions while it is limited by the diffusion process at high-injection conditions. The gray area indicates the possible range of carrier transport times.

considered. It has been suggested that carrier drift velocity can be calculated by

$$v_c = \frac{\mu_c E}{[1 + (\mu_c E/v_{\text{sat}})^C]^{1/C}}, \quad (12)$$

where  $C \approx 2$  for electrons and  $C \approx 1$  for holes [13],  $v_{\text{sat}}$  is the carrier saturation drift velocity,  $\mu_c$  is the carrier mobility, and  $E$  is the electric field in the active region. Although the actual electric field is a function of the position and is determined by the operating condition of the device, in the case of low injection, it could be roughly estimated by  $E \approx (V_{\text{bi}} - V)/L_b$ , where  $V_{\text{bi}}$  is the built-in voltage determined by the  $n$ - and  $p$ -doping concentrations of the  $n$ - and  $p$ -regions, respectively, and  $V$  is the output voltage. The diffusion time can be calculated by  $\tau_{\text{diff}} = L_b^2/2D$  where  $D$  is the ambipolar carrier diffusion coefficient. If the electron and hole densities are assumed to be equal, then  $2/D = 1/D_n + 1/D_p$ , which means that the ambipolar diffusion current is the sum of electrons and holes. Taking GaAs materials as an example, the calculated value of the drift time is 0.5~50 ps while the diffusion time is 10~1000 ps for the width of the  $i$ -region which varies from 0.1 to 2  $\mu\text{m}$ , as shown in Figure 2. The diffusion current is usually rather small compared to the drift part, and it only becomes important at a very high-injection condition (e.g., solar cells operated with concentrators) where electron and hole densities are almost equal and the electric field resulted from the space charge in the  $i$ -region is very small and can be neglected. Under such circumstances, the slow carrier transport processes will certainly impede the output photocurrent of the solar cells, according to the result of (10). Therefore, the carrier transport processes are a vital factor that determines the performance of a solar cell.

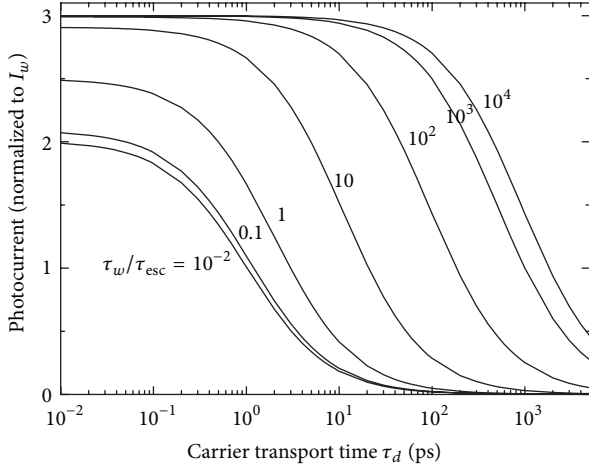


FIGURE 3: Total output photocurrent (normalized to the photocurrent contributed from nanostructures  $I_w$ ) as a function of the carrier transport time  $\tau_d$  at different ratios of carrier lifetime in nanostructures and the carrier escape time ( $\tau_w/\tau_{esc}$ ). Here, the carrier capture time is assumed to be 1 ps and the carrier lifetime of the bulk material is 1 ns.

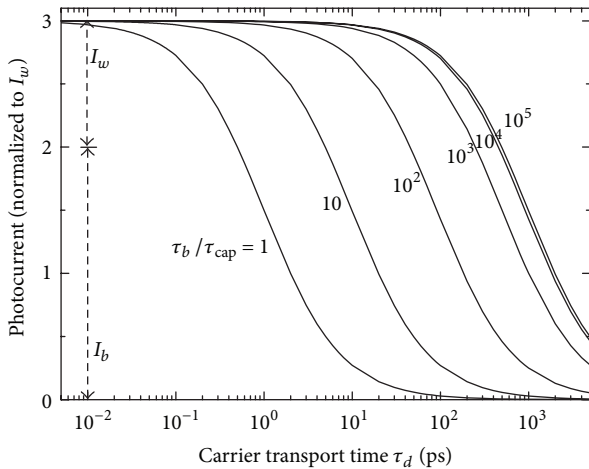


FIGURE 4: Total output photocurrent (normalized to the photocurrent contributed from nanostructures  $I_w$ ) as a function of the carrier transport time  $\tau_d$  at different ratios of carrier lifetime in the bulk material and the carrier capture time ( $\tau_b/\tau_{cap}$ ). Note that the dot line indicates the photocurrent contributed from the bulk host material  $I_b$  and the nanostructures  $I_w$  at very small carrier transport time. Here, the carrier escape time is assumed to be 1 ps and the carrier lifetime of nanostructures is 1 ns.

Based on the above theoretical model, the calculated results of carrier transport time on the output photocurrent of a solar cell embedded with nanostructure are shown in Figures 3 and 4. Usually the carrier lifetime for direct band-gap materials, such as GaAs, is in the range of nanoseconds if the spontaneous emission of photons is the dominant recombination process. The escape time for nanostructures with small potential difference from the bulk material via the absorption of a single phonon is typically in the range of picoseconds for carrier-polar optical phonon interactions.

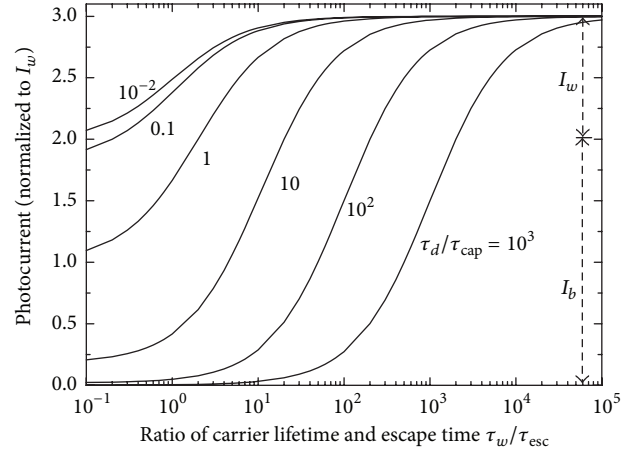


FIGURE 5: Total output photocurrent (normalized to the photocurrent contributed from nanostructures) as a function of the ratio of carrier lifetime in nanostructures and the carrier escape time ( $\tau_w/\tau_{esc}$ ) at different ratios of the carrier transport time and the carrier capture time ( $\tau_d/\tau_{cap}$ ). Note that the dot line indicates the maximal photocurrent contributed from the bulk material  $I_b$  and the nanostructures  $I_w$  with the minimal effects of carrier escape and capture processes. Note that the carrier lifetime of the bulk materials is assumed to be 1 ns.

As a result,  $\gamma \approx 10^3$  can be reasonably assumed for such a case and the carrier transport processes will have a negligible effect on the output photocurrent if the carrier transport time is smaller than 10 ps, as shown in the results of Figure 3. On the other hand, for nanostructures with very large potential difference from the bulk material, carriers can only escape from the nanostructures by absorbing several phonons and the escape time could be in the range of nanoseconds. If  $\gamma \approx 1$  is assumed for such a case, the nanostructures could possibly contribute the output photocurrent only if carrier transport time is smaller than 1 ps, as shown in the results of Figure 3.

The effect of the carrier escape processes is a vital factor determining the usefulness of the nanostructures in the solar cell. This can be fully appreciated from the calculated results in Figures 5 and 6. For carriers suffering from an extremely large escape time and thus a large ratio of carrier lifetime and escape time, if carriers have very slow transport process as well, the device can only generate a negligible amount of output photocurrent. Under such circumstances, the nanostructures in fact act as gigantic recombination sites and have no beneficial effect at all on the bare bulk solar cell.

In fact, the effects of carrier transport, capture, and escape processes are not separated incidents working independently from each other. On the contrary, they are closely intertwined with each other and affect the performance of solar cells simultaneously. The overall effect of carrier transport, capture, and escape processes on the output photocurrent can be illustrated from the calculated results of Figure 7. It clearly demonstrates that the beneficial results from the embedded nanostructures cannot be warranted. Slow escape processes and long transport time will turn the nanostructures into gigantic recombination sites and cause a detrimental effect on the bulk solar cell, rather than a beneficial one.

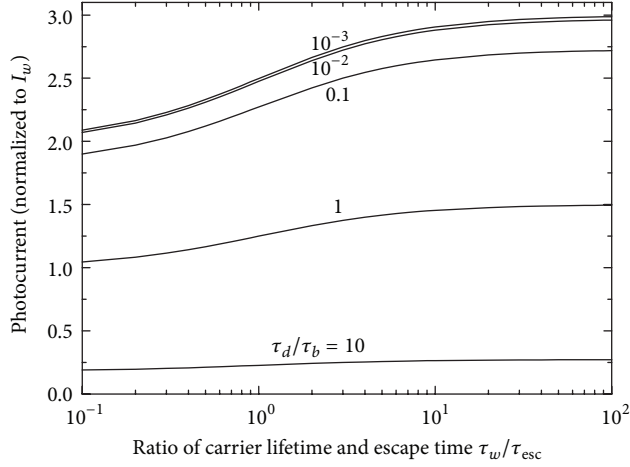


FIGURE 6: Total output photocurrent (normalized to the photocurrent contributed from nanostructures) as a function of the ratio carrier lifetime in nanostructures and the carrier escape time ( $\tau_w/\tau_{esc}$ ) at different ratios of the carrier transport time and the carrier lifetime of the bulk material ( $\tau_d/\tau_b$ ). Note that the carrier capture time is assumed to be 1 ps.

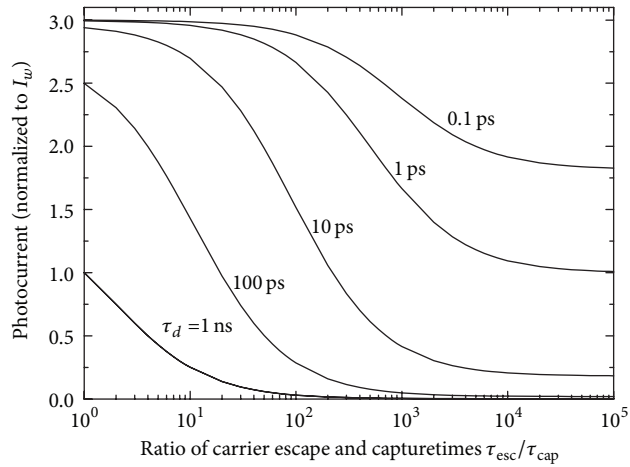


FIGURE 7: Total output photocurrent (normalized to the photocurrent contributed from nanostructures) as a function of the carrier capture/escape time ratio ( $\tau_{esc}/\tau_{cap}$ ) at different carrier transport times. Here the carrier lifetimes in the nanostructures and the bulk material are assumed to be 1 ns.

The device design issue regarding the choice the nanostructure material with the optimal band-gap energy can be calculated and discussed by using the theoretical model presented in this work. The carrier capture/escape processes mainly proceed via the emission/absorption of phonons with limited amount of energies and thus strongly depend on the band-edge energy difference between the nanostructures and the bulk material. It has been shown that the carrier capture/escape time ratio almost exponentially depends on the potential difference between the band edges of the quantum wells and the bulk barriers as

$$\frac{\tau_{cap}}{\tau_{esc}} \propto \exp\left(-\frac{\Delta E}{k_B T}\right), \quad (13)$$

where  $k_B$  is the Boltzmann constant,  $T$  is the carrier temperature, and  $\Delta E$  is the band-edge energy differences of the conduction bands for electrons or the valence bands for holes [8, 9]. However, carriers capture/escape processes in other nanostructures, such as quantum dots, might be rather different from the cases of quantum wells, but the general relation given by (13) could be still observed, as long as the carriers proceed their capture/escape processes via the emission/absorption of phonons.

The output photocurrents as a function of the band-gap energies of the nanostructure materials are calculated and the results are shown in Figure 8 with different carrier transport/capture time ratios. The calculated results clearly demonstrate that there exists an optimal band-gap energy of the nanostructures for achieving the maximal output photocurrent. Nevertheless, the exact value of the optimal band-gap energy critically depends on the carrier lifetime in the nanostructures.

In the cases of very fast carrier transport, the results shown in Figure 8(a) indicate that the nanostructures generally have beneficial effect on the output photocurrent. On the contrary, in the cases of very slow carrier transport, as shown in Figure 8(c), the photocurrent contributed from the nanostructures becomes less significant, while the photocurrent contributed from the bulk material is severely degraded by the carrier escape processes. Nanostructures with very deep potential depth could have detrimental effect on the bare bulk solar cell even in the cases of very long carrier lifetime (i.e., nearly perfect material conditions). It should be noted that, if a solar cell embedded with nanostructures designed to be operated under light concentration, the devices will then operate at a high-injection condition and thus with a longer transport time. As a result, the effects of carrier transport, capture, and escape processes will become more important and should therefore be considered in the design for such devices operated with solar concentrators.

#### 4. Conclusion

In conclusion, a theoretical model is proposed to study the effects of carrier transport, capture, and escape processes on solar cells with embedded nanostructures. The calculated results show that nanostructures with very small band-gap energies will suffer from extremely slow escape processes. Under such circumstances, carriers cannot efficiently escape from the nanostructures and thus the nanostructures have a negligible contribution for the output photocurrent, while the capture processes will make the nanostructures act as recombination sites. If this is the case, solar cells embedded with nanostructures are even inferior to their bare bulk counterparts, and the inclusion of nanostructures could degrade the performance of the device and totally loses its purpose.

The optimal band-gap energies of the nanostructure materials for achieving the maximum photocurrent are calculated and discussed by using the theoretical model given in this work. The results clearly demonstrate that the effects of carrier transport, capture, and escape processes on a solar cells embedded with nanostructures are very significant and

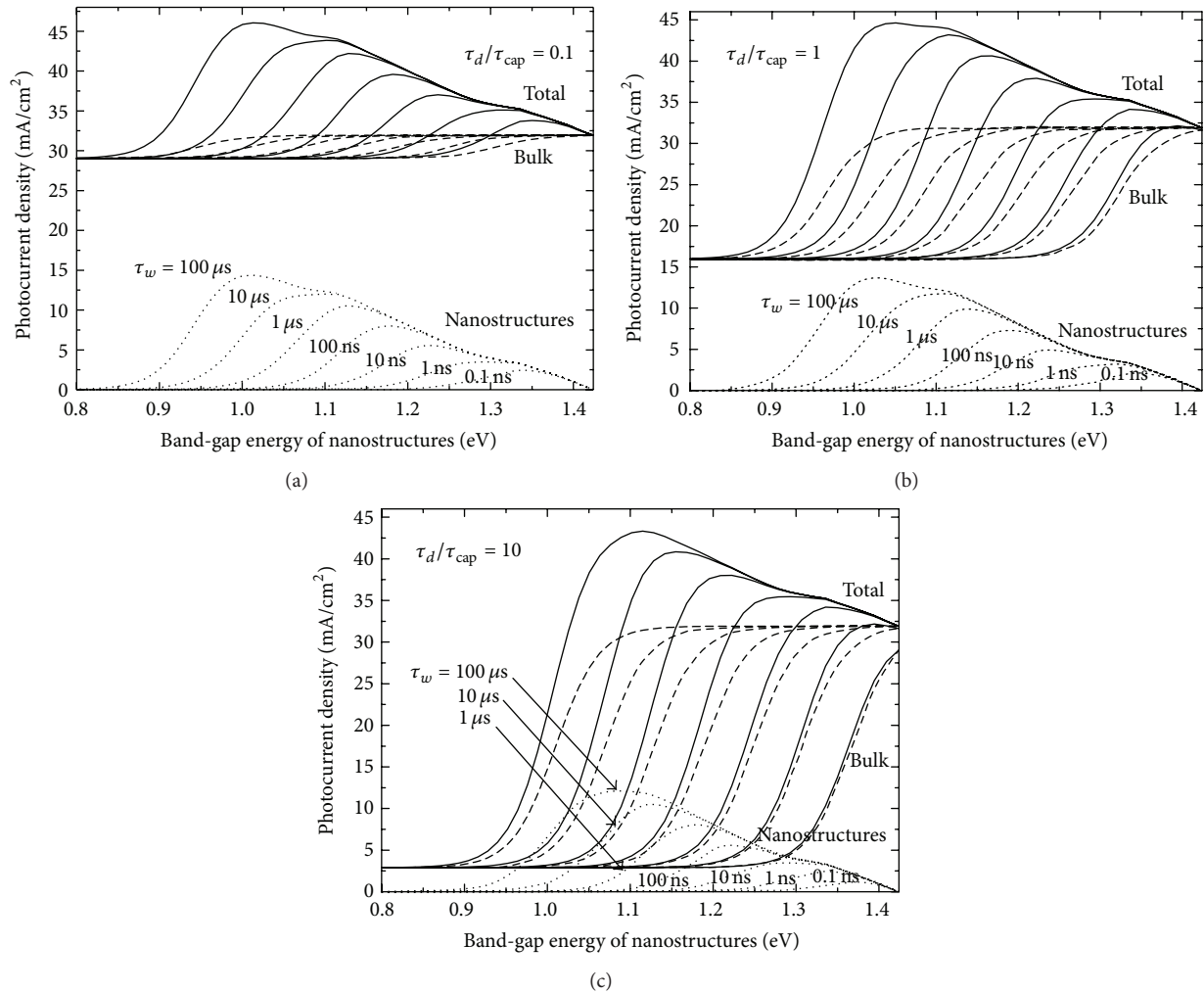


FIGURE 8: The output photocurrent density contributed from the nanostructures (dot line), the bulk material (dash line), and their sum (solid line) as a function of the band-gap energy of the nanostructures at different carrier lifetimes of the nanostructures  $\tau_w$ . (a) The ratio of the carrier transport time and the carrier capture time is assumed to be 0.1 to represent the ideal cases of very fast carrier transport processes in the bulk *i*-region. (b) The ratio of the carrier transport time and the carrier capture time is assumed to be 1. (c) The ratio of the carrier transport time and the carrier capture time is assumed to be 10 to represent the cases of very slow carrier transport processes in the bulk *i*-region.

should be considered in the device design, especially in designing devices operated with solar concentrators.

### Conflict of Interests

The author declares that there is no conflict of interests regarding the publication of this paper.

### Acknowledgment

This work is partially funded by the Bureau of Energy, Ministry of Economic Affairs, Taiwan.

### References

- [1] M. Mazzer, K. W. J. Barnham, I. M. Ballard et al., "Progress in quantum well solar cells," *Thin Solid Films*, vol. 511-512, pp. 76–83, 2006.
- [2] A. J. Nozik, "Quantum dot solar cells," *Physica E*, vol. 14, no. 1-2, pp. 115–120, 2002.
- [3] P. S. Zory Jr., *Quantum Well Lasers*, Academic Press, San Diego, Calif, USA, 1993.
- [4] V. M. Ustinov, *Quantum Dot Lasers*, Oxford University Press, Oxford, UK, 2003.
- [5] A. Zachariou, J. Bames, K. W. J. Barnham et al., "A carrier escape study from InP/InGaAs single quantum well solar cells," *Journal of Applied Physics*, vol. 83, no. 2, pp. 877–881, 1998.
- [6] S. M. Ramey and R. Khoie, "Modeling of multiple-quantum-well solar cells including capture, escape, and recombination of photoexcited carriers in quantum wells," *IEEE Transactions on Electron Devices*, vol. 50, no. 5, pp. 1179–1188, 2003.
- [7] A. Alemu, J. A. H. Coaquira, and A. Freundlich, "Dependence of device performance on carrier escape sequence in multi-quantum-well p-i-n solar cells," *Journal of Applied Physics*, vol. 99, no. 8, Article ID 084506, 5 pages, 2006.

- [8] C. Y. Tsai, C. Y. Tsai, Y. H. Lo, R. M. Spencer, and L. F. Eastman, "Nonlinear gain coefficients in semiconductor quantum-well lasers: effects of carrier diffusion, capture, and escape," *IEEE Journal on Selected Topics in Quantum Electronics*, vol. 1, no. 2, pp. 316–330, 1995.
- [9] C. Y. Tsai, L. F. Eastman, Y. H. Lo, and C. Tsai, "Breakdown of thermionic emission theory for quantum wells," *Applied Physics Letters*, vol. 65, no. 4, pp. 469–471, 1994.
- [10] N. G. Anderson, "Ideal theory of quantum well solar cells," *Journal of Applied Physics*, vol. 78, no. 3, pp. 1850–1861, 1995.
- [11] D. M. T. Kuo and Y. C. Chang, "Dynamic behavior of electron tunneling and dark current in quantum-well systems under an electric field," *Physical Review B*, vol. 60, no. 23, pp. 15957–15964, 1999.
- [12] J. Nelson, *The Physics of Solar Cells*, Imperial College Press, London, UK, 2003.
- [13] S. M. Sze and K. K. Ng, *Physics of Semiconductor Devices*, John Wiley & Sons, New York, NY, USA, 3rd edition, 2007.